Parameter estimation for subsoil modelling via seismic refraction

Bibiana Boada[a], Director: Olga Lucia Quintero[b], Co-director: Juan Guillermo Paniagua[b]

[a]*MSc. Student in Applied Mathematics, Universidad EAFIT, Medellín , Colombia*
[b]*Department of Mathematical Sciences, Universidad EAFIT, Medellín , Colombia. Medellín, Colombia.*

Abstract

For mining exploration in geologically complex zones, there are several techniques, including seismic refraction, which studies the propagation of artificially produced seismic waves, establishing its relationship with the geological configuration of the subsoil. One of these techniques is the Generalized Reciprocal Method (GRM), which has been proposed for the reconstruction of subsurface structures with lateral velocity variations. This method depends on several parameters, mainly on a single parameter called the optimal distance of XY. This optimal value of XY presents uncertainties when this is determined. A good estimate of this parameter determines a good characterization of the subsoil, determining other parameters such as velocity and depth of layers in the media. A good determination of GRM parameters also permits recognition and definition of near-surface irregularities. In this paper, we proposed a robust mathematical form to find the optimal value of XY looking for the functional average curve that looks for the curve that remains for more time in the center of the set of curves. Obtaining the curve of the median corresponding to one of the velocity functions with optimal XY values, we obtain the optimal robust XY value in order to reduce the uncertainties in such a way that a better delineation of the subsurface structures is achieved, with a good approximation, through obtaining the average velocity and depth of layers.

Keywords: Mining exploration, Generalized Reciprocal Method (GRM), Robust mathematical, Optimal XY value.

1. Introduction

In the National Development Plan "All of a new country" 2014-2018 is proposed in the area of Science, Technology, and Innovation the need of training researchers and innovators that will lead the transformation of the country. In this sense, the Government of the Department of Norte de Santander and the Administrative Department of Science, Technology and Innovation - COLCIENCIAS presented a call for the formation of high-level human capital for the Department of Norte de Santander, giving priority to the sectors of Energy, Mining, Agriculture, Agribusiness, Commerce, Tourism, Health, ICT, Fashion, Biotechnology and Education [1].

Emphasizing the previous call and taking into account that Norte de Santander is a department that due to its geographical location is rich in natural resources such as coal and oil and a little over four million barrels of crude have been extracted there from 2012 to date. The previous placed it in the 12th position of departments with the highest production of hydrocarbons, a place where a large part of the country's oil industry is concentrated. Besides, Norte de Santander has coal reserves distributed in Catatumbo and Tasajero and other carboniferous zones with less potential, Zulia -Chinacota, Pamplona, Don Juana, Salazar and Toledo [2].

Searching for minerals or materials found in the subsoil awake great scientific and economic interest in a country where one of the economy's pillars is the exploitation of natural resources, especially

*Corresponding author

Email addresses: bboadas@eafit.edu.co (Bibiana Boada), oquinte1@eafit.edu.co (Director: Olga Lucia Quintero), jpaniagu@eafit.edu.co (Co-director: Juan Guillermo Paniagua)

mining and hydrocarbons [3]. Due to this, it is essential to use new technologies and techniques to make the most of these resources, reducing costs and increasing production.
The mining expansion has been encouraged and accompanied by the central government since an increase in this activity of 70% is expected and evidenced by the rise in GDP (Gross Domestic Product), a projection suggested by the IMF (Monetary Fund International) more than five years ago [4].
The seismic refraction method has been used in Latin America to find specific materials, such as Brazil and Chile. In Brazil, it was used to study a deposit of bauxite in the Barro Alto - Goiás region, Brazil [5] where it was concluded possible to define the interface between the substantial portion and the mineralized portion in the study area.
In Chile through "Geophysical Services in Mining and Engineering (SEGMI)" which is a consulting company that provides services and advisory services for "Applied Geophysics", oriented to support in the exploration of natural resources, solving engineering problems geotechnical and civil works construction [6], concluded that the basal accumulation controls the seismic architecture and the growth of the crust of southern Chile. In the faculty of physical and mathematical sciences of the University of Chile, thesis papers have been presented where the seismic refraction method has been used for the estimation of cutting wave velocities [7]; likewise, the Catholic University of Chile has works on the application of geophysical methods for the characterization of soils, where with conventional seismic refraction equipment and combining it with different methods or data analysis techniques it demonstrated its capacity for the exploration of the first 30 meters deep [8].
In this way, the current research becomes relevant since there is little information on geological studies in the department of Norte de Santander for the exploration of mineral resources, besides there is no theoretical support showing mathematical and physical analyzes that determine the characteristics of the subsoil making use of computational algorithms.
For this reason it is proposed to investigate, implement and test computationally efficient algorithms for the interpretation of images of the subsoil obtained from data recorded by applying seismic refraction method in geologically complex zones for the increase of mining exploration and the characterization of the underground the Department.
Taking into account the seismic refraction method since it is a relatively inexpensive method (the equipment used to obtain data can be easily obtained), it covers large areas of study in a concise time, and the processing and interpretation of data is relatively simple [9].

2. Subsoil modeling problem

One of the main factors at time to search minerals is to make an excellent mining exploration, in which it should be determined if a particular area presents possibilities that exist a specific type of mineral field. The preceding is established in the function of the available information on the type of deposit and on the geology of the study region. For this, different techniques [10], including geological, geophysical, geochemical and sampling by drilling or excavations are distinguished used. Some of these only differ in the escalation and others in costs.
After obtaining a quantity of data, these must be analyzed optimally to make a functional characterization of the subsoil. The most common methods of interpretation are intercept times, apparent speeds, wavefronts, delay times and generalized reciprocity. The advent of increasingly sophisticated computational methods has allowed the development of refraction topographic processing algorithms. These algorithms enable solving variations or gradients of speeds in depth and lateral changes in highly variable media, as, for example, due to the presence of cavities, faults, among others. Topographical images generally show gradual changes variations speeds oppositely to what is obtained in the traditional methods which have identified strata constant speeds within each [11].
Some techniques for gathering and analyzing data that are currently used for mining exploration and that have improved over time due to the technological breakthrough are the following:

- *Geological Techniques.*
- *Geochemical Techniques.*
- *Geophysical Techniques.*

The geophysical techniques must be chosen among those that have the best possibilities to solve a specific problem, establishing, according to the geological-mining knowledge that they have. The advantages associated with geophysical methods are their relatively low cost, the possibility of covering large areas of land and that are not destructive techniques.
As for disadvantages, the possible indetermination of the results can be highlighted, or it can have a margin of possible error because they are indirect techniques that require a process of data inversion and the decrease of the resolution with the increase of the depth investigated [12, 13].
We will focus on the geophysical technique called the Seismic Method. The seismic method is based on the different conduction velocity that the different rocks have for the elastic waves. These are produced through an artificial tremor caused by an explosion [14]. Its objective is the study of the subsoil in general, which allows obtaining geological information of the materials that comprise it. Seismic prospecting is a powerful research tool since it can be inspected with a good resolution from the first meters of the ground to several kilometres deep [15].

2.1. Scheme of the Seismic Method

In the seismic method is generated by a pulse or a vibration at a shallow depth and the resulting movement of the ground at points near the surface is detected by *geophones*. The measurements of the pulse time travel to the different geophones located at certain distances give the velocity of propagation of the pulse in the ground. The soil is not generally homogenous in its elastic properties and this velocity varies in both depth and lateral distance [16].
When the soil structure is simple, the values of elastic wave velocity and the positions of the boundaries between the regions of different velocity can be calculated from the measured time intervals. Limits speeds generally match geological boundaries, and a cross-section in which the speed interfaces are drawn can at least resemble geological cross-section, although the two are not necessarily the same [16].
When a pulse is generated, waves are generated that propagate through the floor, both inside and on the surface. Seismic waves, consisting of small packages elastic deformation energy, away from any seismic source at speeds determined by the elastic moduli and densities of the media through which spread [17].
If the equilibrium equations of the body affected by the perturbation are analytically expressed, a system of equations is obtained from which four solutions have been deduced that give rise to longitudinal, transverse, Rayleigh and Love waves [18].

3. State of the art in the seismic method

To have a successful extraction of minerals, an excellent exploration must be done in which geophysics has become a widely used tool, since it is a science that studies the physical properties of the earth, or in other words, determines the structure of the earth from diverse physical properties characteristic of each material that form it [19].
In the applications of geophysics are helping to solve various problems that can be found in the first meters of a depth of the ground, for this reason, some fields of action are [19]:

- Reconnaissance of the land.
- Determination of cavities and fractures.

- Evaluation of the effectiveness of treatments in the improvement of the land.
- Find damage to existing structures.

Since the beginning of the geophysical exploration, three basic principles have been used such as: the measurement of small variations in the magnetic field, the measurement of small variations in the gravitational field and the measurement of the propagation time of the elastic waves through the land. These three basic principles are the basis of practically all the geophysical work done up to the present time [20].

The seismic method is one of the geophysical methods much more direct in its relation to geology than the potential methods. Reflection zones or horizons often correlate directly with the geological layers and give relatively accurate measurements of their depth and shape. However, in many cases, correlations with geology may be uncertain or misleading. In such cases, gravimetric and magnetic data may contribute to the establishment of limits on possible correlations and provide lithological information [20].

In the nineteenth century, the seismic theory reached a high degree of development. Studies of earthquake waves led to an excellent understanding of the internal structure of the Earth and a relatively detailed model of the Europa crust [21].

The seismic refraction method was quite successful in locating the salt coils, first along the Baltic coast of Germany and later along the coastal regions of the Gulf of Mexico in the United States. There, substantial dynamite charges were used to generate the seismic waves to measure quite long distances with suitable amplitudes to be recorded by the primitive instruments of the moment [21]. Although the refraction data can be analyzed and interpreted quickly, they have a fatal flaw: they can not give accurate results unless the seismic velocity in each layer of rock is higher than the previous one. An exception to this situation, a reversal of velocity, causes the layer velocities and the incorrect thicknesses to be calculated [21].

The methods of seismic refraction are entirely used for the study of the geological environment they are based on the analysis of body waves. The seismograms obtained usually contain very remarkable records of surface waves [22]. The seismic refraction technique provides a simplified characterization of relatively large and two-dimensional volumes (distance and depth) and has been used for transport facilities [23].

In Zaria, Nigeria used the technique of seismic refraction to obtain images of the subsoil under an earth dam, revealing five different layers within the area, being very good to delineate channels of infiltration of the subsurface of a ground dam [24].

In Ostler Fault, South Island, New Zealand, the seismic refraction technique combined with seismic reflection was used to understand the active fault structure associated with the convergence of the tectonic plates. Pacific and Australia consisting of a series of inverse faults that break on the surface [25].

The seismic refraction method is used for the classification of anomalies near the surface since it clearly distinguishes the models that belong to different groups [26]. At the Imam Khomeini International Airport (IKIA), Iran, vertical electric sounding methods and seismic refraction techniques were used, in an attempt to define the underground structure, the variation in the thickness, the resistance of the layers and determine the areas prone to the earthquake in the area [11]. During the 2008 to 2011 period in Finland, shallow seismic refraction studies were conducted to provide accurate images of the seismic structure [27].

The GEOMARGEM research group (Geology and Passive Margin Oceanography) developed an interface to optimize the use of the seismic data processing tools offered by free software Seismic Unix (SU) , in collaboration with the Laboratoire d'Ingenierie et Geosciences du Littoral of the University of Caen Basse-Normandie (UNICAEN), France, within the scope of a CAPES project - Marine Sciences entitled "Oceanographic and Geological Studies - Geophysicists integrated in the bay and

continental shelf environments throughout the State of Rio de Janeiro ". This work was presented within the framework of the VII Symposium of Geophysical 2016 [28]

Within the framework of the Seventh Brazilian Symposium on Geophysics, papers were presented in which seismic refraction was presented as a tool, combining it with other geophysical techniques. Such as the case of the paper " Integration of the seismic refraction tomography and the multichannel analysis of surface waves in surface research in the Termas de Ibira region, Sao Paulo state, Brazil" [22]. And the paper entitled "Application of MASW Seismic Methods and Refraction Tomography for the Determination of Mechanical Soil Properties: a case study in the municipality of Cacapava do Sul / RS" [29], which sought to maximize the results obtained with the seismic refraction and obtain new valuable information for each investigation.

Concerning Colombia, mining was initially carried out indiscriminately, causing environmental damage and economic instability. The most notorious and worrisome changes are those associated with climate change, the increase of extreme climatic phenomena, the increase in temperature, the decrease in average precipitation and the consequent droughts, the rise in sea level, the loss of biological diversity and the extinction of species that affects the loss of ecosystem services and species used for medicinal purposes or the collapse of fishing activities [30].

Despite the full range of mineral and energy products that exist or may exist in Colombia, there are a number of common consequences to their extraction: new conflicts over land tenure, dispute between illegal armed actors for capturing a portion of mining rent, growing demand for water, contamination of water sources and soils, damage to the landscape and soil, among others [30].

Regarding the issue of the administration of mining resources, it is essential to recognize that there has been an active transformation in the institutional structures of the sector, which has led to a lack of continuity in the development policies of the sector. Likewise, a series of programs and projects have been implemented in mining-environmental matters, but they have presented limitations due to the lack of coordination between the mining and environmental authorities [31].

In Colombia they have been developed at the head of some universities, research into the basement, which seeks to improve Pics, search for hydrocarbons detect faults among other things. The National University of Colombia created a manual for the acquisition and processing of terrestrial physics and its application in Colombia [32], in which a study of the processes of acquisition and processing was carried out. Besides, international procedures were studied, and finally, after making comparisons, recommendations were made in areas where there is the possibility of updating procedures and seismic knowledge.

The school of civil and geomatics engineering from Universidad del Valle, carried out a study on the seismic behavior of soil deposits in Cali, Colombia, in which they took into account the variations of effects. Those are based on the characteristics and properties of the various terrains to optimize land uses regarding their seismic response [33].

In the Francisco Jose de Caldas District University, in its cadastral engineering and geodesy Bogota program, they made the characterization of the subsoil using the geophysical refraction method, the Simon Bolivar circumvallation and central park where the behavior of surface waves was analyzed in the types of soil, and the thickness of the sediments in the study area is determined [34].

A geophysical characterization of the closed and operational areas was also carried out in "LA CORTADA" regional sanitary landfill facilities in the municipality of Pamplona Norte de Santander, using the geophysical method of seismic refraction guided by the University of Pamplona in the program of civil engineering, since it represents a high environmental complexity due to the ignorance of the impacts of its operation on the shallow layers of the soil on which the waste rests [35].

Concerning data analysis, the main algorithms commercially available today are *Rayfract, GeoCT-II, and SeisImager-2D*. The last studies are based on some of them for the analysis of the data that were obtained from the geophysical method of *seismic refraction*. Following are some characteristics of each program.

- *Rayfract* First, a database is created to store the data and the geometry of time travel. Once

the data is imported, the topographic geometry must be imported or specified from within the code. Once the data is imported and the geometry is specified, there are two processing options. The difference between the two options is in what the initial model is used.

The first option is to use the Delta-t-V method to generate an initial model.

The second option within Rayfract is to use the "soft inversion" algorithm. It automatically creates a one-dimensional initial model based on the results of Delta-t-V [36].

- *SeisImager* The data is only imported into the code. There are two ways to create the initial model: The first is to use a time and time investment algorithm contained in the code to generate a simple layered model.

  This layered model is converted to a grid model. It is a useful method for simple data where different slopes can be associated with particular refractors. The alternative is to create a pseudograde model specifying a speed range, dimensions, and the number of layers [36].

- *GeoCT-II* is derived from much more expensive codes developed for the oil industry. The first step is to import the times travel using the first arrival selection subroutine. Then the initial model can be generated using one of two methods.

  The first is to generate a model of your choice using the model generator subroutine. It works well if you want to use a simple gradient model, or if you have an estimate of the velocity structure.

  The other method is to use a subroutine that displays the time travel data and create a simple layered model from the selection of inflection points (i.e., changes in the slope) in the data, which are displayed in a graph of displacement time of the verses. As with Rayfract, the spacing of the grid can be set for the initial model and used for the tomography analysis step. There is also a smoothing parameter x/y that can be adjusted to improve the resolution and quality of the scan result. [36].

In the previous works the traditional techniques mentioned in the description of the problem have been used (section 2) and that stretch in the theoretical framwork included in the AppendixA.
It is also taken into account that none of the previous ones has reported the development of a robust method that allows reducing the uncertainty in the obtaining of the speeds taking into account the uncertainty of the measurements.

4. Research Hypothesis

The foregoing indicates that Norte de Santander has significant mineral exploitation, some of these operations are legal and others illegal, but it has sizeable unexplored territory since a large sector of the department is affected by violence or is geologically complex because of its geographic location. For mining exploration in geologically complex territories, there are several techniques, among them the seismic refraction, which studies the propagation of seismic waves produced artificially, establishing its relationship with the geological configuration of the subsoil. It is a handy method for the investigation of the geological structure, the properties of the land, problems of foundations, as well as the study of alluvial layers, landslides, gravel pits, and sand pits, among others [37].
On the other hand, the seismic refraction method is a non-destructive geophysical method, used for the interpretation of the properties of the soils, and the detection of the depth of the rock, by analyzing the variations in the seismic velocities [9].
In this order of ideas comes the question: How to determine if a particular area presents a probability that there is a specific type of mineral deposit using seismic refraction as the primary tool for obtaining data, minimizing environmental effects and costs?.

It is then proposed in a general way: To develop a mathematical solution that allows diminishing the uncertainty associated to the location of the sensors in the capture of the data that are used for the reconstruction of the subsoil through seismic refraction techniques.
The relevance of this development must be justified based on the following: In the report of the regional economic situation (ICER) of the year 2015, Norte de Santander had one of the highest increases compared to the year 2014 in the GDP (Gross Domestic Product). These increases occurred in coal extraction, lignite coal and peat (30.4%), extraction of uranium and demiral minerals (27.3%) and air transport (26.7%) [38].

5. Generalized Reciprocal Method (GRM)

Interpretation techniques for data obtained with seismic refraction are very varied. For the simple case where the refractor is flat, and velocities in layers are increased with depth, the corrected refraction times can be converted to depth using time-distance curves. In practice, geology is generally more complicated than this simple case implies, but a model of reasonable depth can often be obtained using this simplistic approach.
Time-distance curves obtained from a seismic refraction study contain information on the velocity and the structure of the refractor and, to some extent, on the upper layers. It is essential that the analysis of a specific refractor uses only the arrivals associated with that refractor; this may not be the case if the wrong displacement range is used because arrivals may include those of a deeper or shallower layer.
Some of these are more applicable to studies of surface refraction, others to broader objectives. The commonly used techniques are the ABC method (delay time), the Hagedoorn method or the plus-minus method, the generalized reciprocal method (GRM), the Gardner method, the Blondeau method, time-term inversion (decomposition), and tomographic approaches.
The general wavefront technique has historically been considered a graphical method, and as such gives the interpreter a good understanding of the refraction method and some of its limitations [39].
The **generalized reciprocal method** (GRM) is a technique for delineating undulating refractors, at any depth, from in-line seismic refraction data consisting of forward and reverse traveltimes [40] (See AppendixB). With these times of arrival on some occasions, approximations of the velocity of layers can be made, as it is the case of intercept time method. When approximations cannot be made, or the speeds of all the layers above the refractor are not known, an estimation of the refractor speed can be obtained.
The first phase in the procedure involves the calculation of the XY value.All the possible values between the disturbances A and B are taken into account, since the value of XY is the distance between two geophones, leaving in the center the geophone G which is to which the depth and velocity of the medium will be analyzed directly under. It is achieved using the velocity analysis function and the generalized time-depth values. In the ray diagram of Figure 1, the sources are in A and B and the receivers in X and Y. In the Figure 2 is the travel-time curves in the forward and reverse direction.
In AppendixB the Seismic refraction model 2D is detailed.

5.1. The velocity analysis function

The velocity analysis function (t_v) is given by:

$$t_v = \frac{1}{2}\left(t_{AY} - t_{BX} + t_{AB}\right) \tag{1}$$

where t_{AY} is the time travel from source A to receiver Y, t_{BX} is time travel from source B to receiver X and t_{AB} is time travel from source A to source B or the reciprocal time.
It is considered that the velocity analysis function is applied at the location G midway between X and Y. The values that are taken into account in the velocity function are values that are extracted

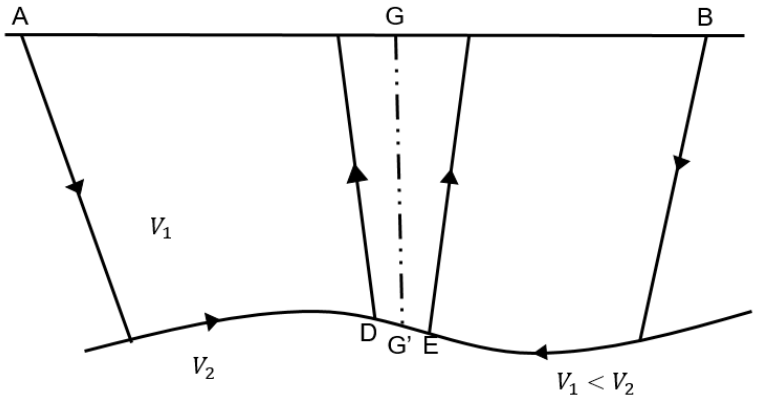

Figure 1: Geometry of the trajectory for the generalized reciprocal method.

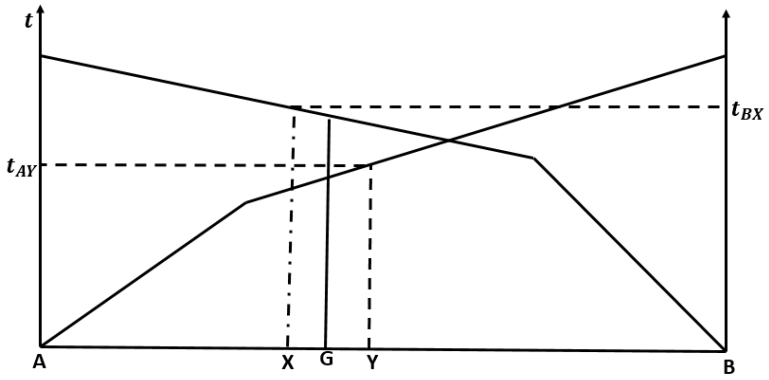

Figure 2: Travel-time curves in forward and reverse directions

from the travel-time curves (Figure 2), which are values of geophones around the geophone G. The optimal value for the distance between X and Y (XY) occurs when they are located on the surface where they measure the time of the two emergent rays of the same point in the refractor, that is, when D, G', E (Figure 1) coincide.

When analyzing refraction data near the surface, it is likely that the XY value has several components because it is based on the depth of the refractor, the velocity of the refractor and the velocity near the surface. For very shallow refractors, the effective XY value is zero, while a deeper refractor the XY value must be higher, and it can be a significant distance. Besides, a feature or anomaly near the surface, such as a local change in elevation, will have an XY value of zero or close to zero. Because the XY value is a composite of times in different directions, it is likely to change along the line if the depth of the refractor or the relative speeds changes or if there are changes near the surface.

In the presence of anomalies close to the surface, such as changes in elevation along the line, it is likely that any analysis of the XY value of refraction arrivals is dominated by surface anomalies, which have an XY value of zero.

In the conventional interpretation with the GRM, the values of the t_v velocity analysis function calculated using equation 1 are plotted against the distance for different values XY (Figure 3). The inverse of an apparent refractive velocity V_n' is defined as the slope of a line adjusted to the values of t_v for the optimal XY, that is,

$$\frac{d}{dx} t_v = \frac{1}{V_n'}. \tag{2}$$

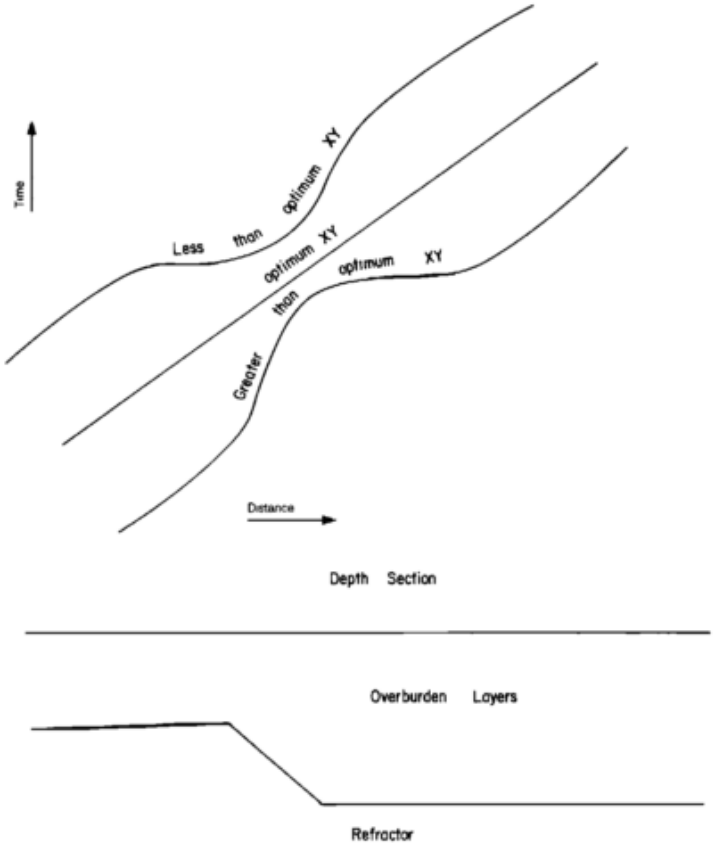

Figure 3: Schematic representation of velocity analysis functions for a refractor with a step in the depth [40].

5.2. The time-depth function

With the XY value and the apparent velocity of the refractor for the nth layer (V_n') can now be used to derive the generalized time-depth function (t_G), which is the one-way time travel to the refractor, defined by

$$t_G = \frac{1}{2}\left[t_{AY} + t_{BX} - \left(t_{AB} + \frac{XY}{V_n'}\right)\right] \tag{3}$$

For practical reasons, values of the generalized time-depth function are often calculated for a range of XY values at the same time as the velocity analysis functions, so that the final term in equation 3, which implies XY and V_n', it can be despised; it is introduced later once these parameters are known.

5.3. Distance between sensors - Value XY

Accurate determination of the XY value is often difficult, especially if the surface characteristics in the refractor are small. Under these conditions, the XY value can be calculated if enough information is available about the refractory layers. A general form of this equation for multiple layers is given by,

$$XY = 2\sum_{j=1}^{n-1} Z_{jG} \tan\left(\sin^{-1}\frac{V_j}{V_n}\right) \tag{4}$$

where .V_n is the velocity of the refractor, Z_jG is the thickness of the layer, V_j is the velocity of the layer, j is the index of the layer, and n is the number of layers

Taking $n = 2$, the value XY for two layers remains

$$XY = 2z \tan\left(\sin^{-1}\frac{V_1}{V_2}\right) \tag{5}$$

where XY is the x_{crit}, which is the minimum distance at which a receiver can be placed to receive the refracted wave.
If the XY value cannot be generated from the refraction arrival times, speed analysis functions or time depth, and if there is no information available about the layers on the refractor, it may often be used an XY value of zero as the default value.
The time-depth profile (t_G), updated with the estimated XY value and the refractor speed as defined in equation 3, is now converted to depth.
For flat layers, the generalized temporal depth was related to the thickness of the layer (Z_{jG}) and the depth conversion factor (V_{jn}) by

$$t_G = \sum_{j=1}^{n-1} \frac{Z_{jG}}{V_{jn}}. \tag{6}$$

A significant advantage of the GRM is that the depth conversion factor is relatively insensitive to drops of up to about 20 degrees because data is used both forward and backward. As a result, the approximation of the horizontal layer can be used for the depth conversion factor, it means,

$$V_{jn} \cong \frac{V_j' * V_n'}{(V_n'^2 - V_j'^2)^{1/2}}$$

where V_j' and V_n' are estimates of apparent velocity and can be calculated with equation 2.
For the case of two layers, having

$$t_G = \frac{Z}{V_{12}} \tag{7}$$

where

$$V_{12} \cong \frac{V_1 * V_2}{(V_2^2 - V_1^2)^{1/2}} \tag{8}$$

then the depth of the first layer (Z) can be expressed as

$$Z \cong t_G \frac{V_1 * V_2}{(V_2^2 - V_1^2)^{1/2}} \tag{9}$$

with speeds V_1 and V_2 of the layers. As it can use the approximation of the horizontal layer, it has $t_G \cong t_0/2$, where t_0 is the *intercept time* of the critically refracted ray, which has no real physical meaning because no refractions to the source arrive.

5.4. Average velocity

An alternative method to convert the generalized depth of time values to depth is the concept of the average velocity from the surface until the refractor. Palmer [41] showed that average velocity V_{prom} can be expressed as

$$V_{prom} = \left[\frac{V_n^2 * XY}{XY + 2t_G V_n}\right]^{1/2} \tag{10}$$

where the total depth Z_G of all the layers is given by

$$Z_G = \frac{t_G V_{prom}}{\cos\left(\sin^{-1}\frac{V_{prom}}{V_n}\right)}. \tag{11}$$

The use of the concept of average speed requires that the optimal value of XY must be calculated correctly.

The insensitivity of the depth conversion factor to immersion angles makes GRM an extremely convenient method for treating irregular refractors, including those covered by a layer within which velocity varies continuously with depth.

5.5. Optimal value for XY

The determination of optimal XY values is probably the most difficult and most important aspect of the GRM. At this stage, there are two different approaches to determining the optimal XY value [41]:

1. **Calculation of the direction of the XY values**. The first approach to determine the optimal XY values is the direct calculation from seismic velocities and thicknesses using the formula:

$$XY_{optimo} \simeq 2\sum_{j=1}^{n-1} Z_{jG}\tan i_{jn} \tag{12}$$

where

$$i_{jn} = \sin^{-1}\left(\frac{V_j}{V_n}\right) \tag{13}$$

Therefore, an optimal XY value can be calculated for any section of seismic velocity as a function of depth, such as that calculated from refraction time travel data using any method of interpretation.

2. **Observation of the XY values**. The second approach is the inspection of time travel data, the amplitudes of the seismic trails or the analysis of the refractor velocity and the time and depth functions.

6. Generalized particle reciprocal method (GPRM)

As explained in previous section, the generalized reciprocal method (GRM) is a technique to find depths and velocities of the subsoil in undulating layers at any depth from inline seismic refraction data.

For this, the travel times forward and backward of the propagated waves are taken into account.

Travel times in two geophones, separated by a variable distance XY, are used in the analysis of the refractor speed and in the calculation of time and depth. (See equation 1)

At the optimal XY spacing, rising ray segments that travel to each geophone emerge near the same point in the refractor. This makes the speed analysis of the refractor the simplest and the depths and times that it shows contain the greatest amount of detail.

On the other hand, the conventional reciprocal method that has XY equal to zero is especially prone to produce numerous fictitious changes of the refractor speed, as well as to produce a coarse smoothing of the topography of the irregular refractor.

The generalized reciprocal method uses the arrival times both forward and backward and is relatively insensitive to immersion angles up to about 20 degrees. As a result, depth calculations for a corrugated refractor are particularly convenient, even when superimposed layers have velocity gradients [40].

The GRM provides a means to recognize and accommodate undetected layers, provided that an optimal XY value can be recovered from the travel time data, the refractor speed analysis and/or the time depths. The presence of undetected layers can be inferred when the observed optimal XY value differs from the calculated XY value. Undetected layers can be accommodated using an average speed based on the optimal XY value. This average speed allows precise depth calculations with commonly found velocity contrasts [41].

With non-optimal XY values, the speed analysis functions can indicate refractor speed changes that vary with the XY separation, both in magnitude and in sign. These fictitious speed changes generally occur with an irregular refractor topography. The XY value, for which the speed analysis function is the simplest, corresponds to the optimal value. The non-optimal XY values also result in the smoothing of the time depths for the topography of the irregular refractor. The value XY for which the depths of time show the greatest amount of detail corresponds to the optimal value.

The existence of these two basic approaches to computation and observation of optimal XY values makes GRM a unique and extremely powerful interpretation method. *If the depth is consistent with the travel time data, the XY values calculated and observed should be similar*. If these values do not match, it is indicated that there are layers not detected.

For each value XY you can obtain a different Speed function and depend on the choice you will find a speed of the medium. A bad choice of XY makes the speed of the medium look highly modified. The velocity function (equation 1) is found for each geophone, therefore you will find as many points as there are geophones for each velocity function, and you will find as many velocity functions as possible separations XY exist.

To determine the optimal XY it is proposed to approximate the resulting points in each velocity function to a polynomial of degree one to then measure the error and thus determine which curve is more linear from the group of resulting curves for each possible XY.

With this you get the velocity of the medium using the equation 1 and the value XY optimal used to find the depth of the layer. The problem may then be the correct choice of a function to approximate the values of XY in a family.

Figure 5 presents possible values for XY, in a set of simulated data where the geophones are distributed every 5 meters to cover a plot of 325 meters. With each value XY the speed of the medium was found, with this it is evident that any change for XY affects considerably the calculation of the speed (Table 1).

Value XY	**Velocity of the medium**
0.	4419.101924
5.	4421.518055
10.	4417.36413
15.	4437.400951
20.	4568.527910
25.	4761.904762
30.	4960.317460

Table 1: Velocity calculated for values XY between 0 and 30 meters.

6.1. Uncertainty

As previously stated, the model that describes the phenomenon is completely deterministic, while the nature of the problem contains very high uncertainties that make it not completely well represented. In reality, the entire phenomenon is depending on the variations of the subsoil, the changes of speed, the different variations of density and speed of the middle of the layers, the uncertainty of the

measurement, the noises in the geophones the spatial location of the geophones. The complexity of the uncertainty makes its modelling a very difficult task.
Consequently, the propagation of mechanical waves in the environment can be represented with a static model of rays as used in GRM, but this model must contain a component that summarizes the sources of uncertainty.
In general, optimal filtering techniques are used to estimate the states of a dynamic system whose inputs and outputs are observed by measurements disturbed by noise. It is understood by " states of a system " to the minimum necessary information in a time zero that jointly to the value of the entrances defined in all time from $t \geq t_0$; allows you to determine the behavior of the system for any $t \geq t_0$.
The measurements are generally uncertain, so we speak of "measurement noise" even if we know the true states of the system, the measurements are not a deterministic function of these states but have a random component.
In this context, the evolution of the states is modeled by a dynamic system disturbed by a stochastic process (noise of the states) by means of a stochastic differential equation. The noise or disturbance of the states is incorporated into the model to represent the uncertainties of the system, which may be of a random nature, as well as signals or dynamics not considered in the model.
According to the Bayesian paradigm, the solution of the optimal filtering problem at the time t consists of obtaining the conditional probability distribution of the states, given the information available from the observations until that moment t [**?**].
Therefore, we proceed to incorporate noise to the positions of the geophones or to the recorded arrival times to find an optimal XY for each time the noise is applied to the described phenomenon.

6.1.1. Parameters

The direct, refracted and reflected waves described in AppendixB can be modeled with an uncertainty ζ.

$$t = f_i(\overline{X}, \theta_n) + \zeta \tag{14}$$

where $\overline{X} = (x_1, x_2, ..., x_j)$ it is the vector of distances; $\theta_n = (\overline{V}, \overline{z})$; $\overline{V} = (V_1, V_3, ..., V_n)$ it is the velocity vector; $\overline{z} = (z_1, z_2, ..., z_{n-1})$ it is the vector of depths.
For the case of the refracted wave for a layer we have the equation 15 and for the refracted wave for n layers the equation 16.

$$t_{refr_1} = \frac{2h(V_2^2 - V_1^2)^{1/2}}{V_1 * V_2} + \frac{\Delta x_i}{V_2} = f_3(X, \theta_2) + \zeta \tag{15}$$

$$t_{n-1} = \frac{\Delta x_i}{V_n} + \frac{2}{V_n} * \sum_{i=1}^{n-1} h_i \frac{(V_n^2 - V_i^2)^{1/2}}{V_i} = f_3(X, \theta_n) + \zeta \tag{16}$$

where ζ a random variable that can be of even, Gaussian or colored distribution, and thus generate a family of optimal curves which can be treated as stochastic processes with functional data techniques.

6.2. Optimum XY value

With this we obtain a set of optimal curves from which the functional median is searched using functional data tools such as those incorporated by Fraiman and Muniz [42] where their objective was to find the most central curve of a group of curves, resulting in a sturdy XY optimal.
Another possibility is to construct a probability density function from the curves obtained for each instant t. In this work, the first of the solutions will be addressed and the second will be considered future work to increase the extrapolation capacity of the method.

The value XY is very important in the GRM as already expressed before, in this case, the velocity function (equation 1) is calculated for all possible values of XY which varies from zero to half of the distance of disturbances A and B (Figure 4).

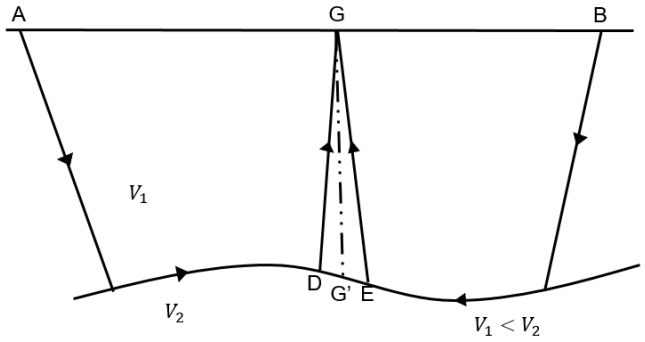

(a) $XY = 0$

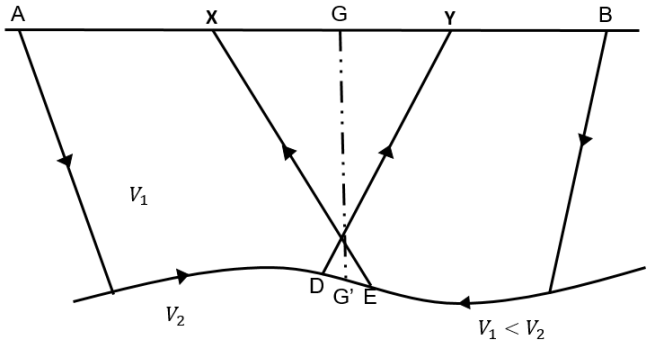

(b) XY is half the distance between A and B

Figure 4: Representation of the minimum and maximum XY distances in a particular geophone G

These values are discrete, since they also depend on the distances between the geophones. That is, for a distance between the disturbances A and B of 325 m with a distance between the geophones of 5 m, the values of XY are 0, 5, 10 , 15, ..., 80 meters.

Between which the optimal XY value should be for all the XY the velocity functions are obtained (Equation 1).

As an example we have the figure 5 where the graphs of the velocity functions for XY between 0 and 30 meters are shown.

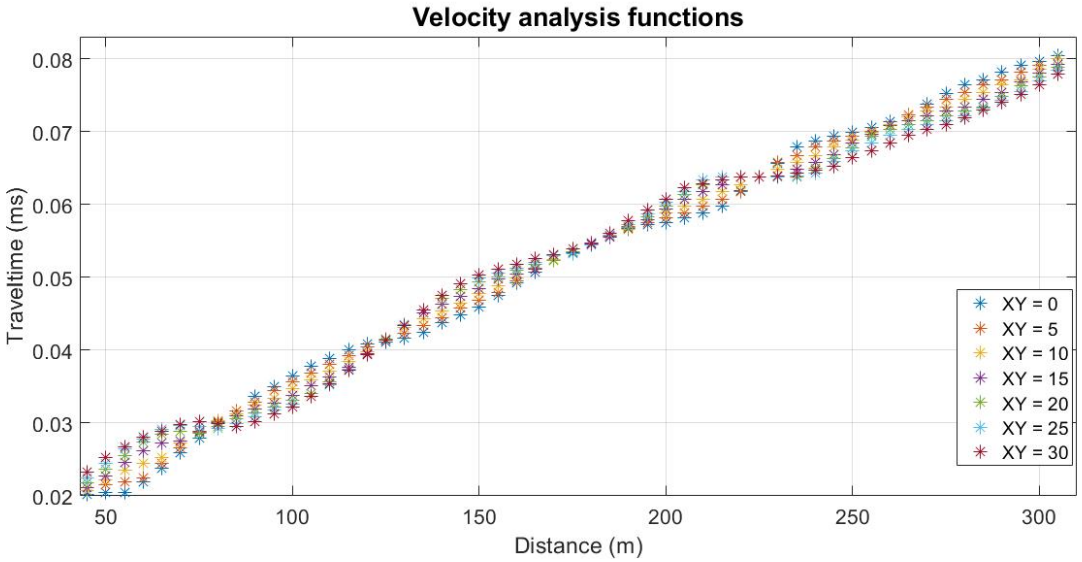

Figure 5: Example of velocity functions for XY between 0 and 30 meters.

After obtaining all the velocity functions for each of the possible values for XY, first-degree polynomial approximations are made to each function, to determine the softest curve. The coefficients for a polynomial $p(x)$ of degree 1 (in the sense of least squares) are found for the data of the velocity function.

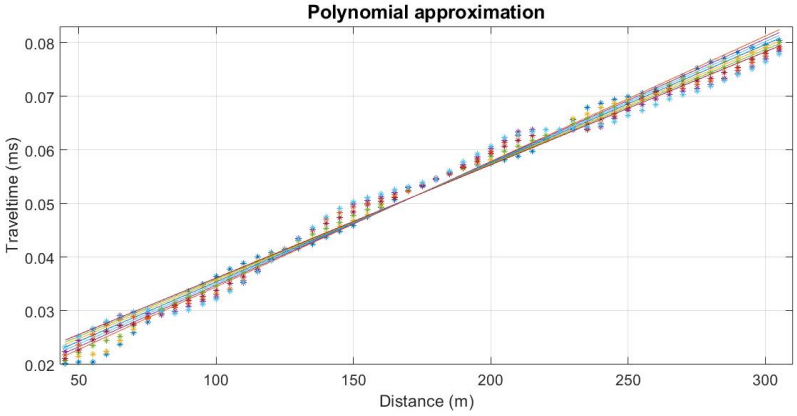

(a) Polynomial approximation

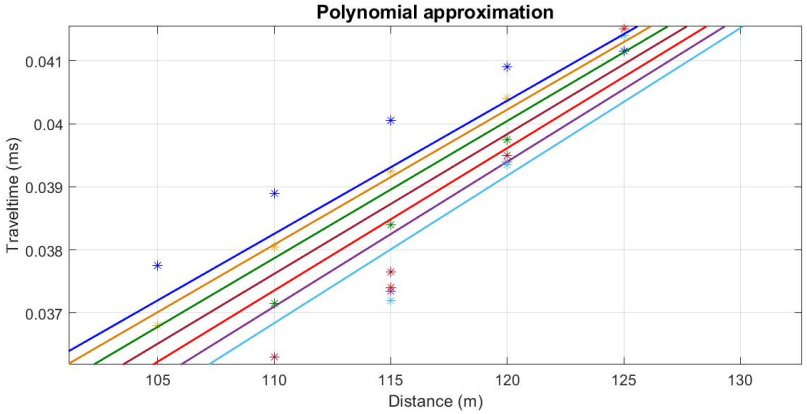

(b) Polynomial approximation zoom

Figure 6: Polynomial approximation for values of XY between 0 and 30 meters

Then we evaluate the data we have from the position of geophones in the polynomial found to then determine which of these speed functions have lower quadratic error with respect to the functions found and the data obtained from the velocity function, with this determines the optimal XY value.

6.3. Robust optimal XY value

The process of finding the optimal value described above is performed for each set of curves. That is obtained by introducing the noise in the original data, with this we have a set of optimal XY curves of which the most representative curve must be found. In this case the median curve described by Fraiman and Muniz is used [42].

6.3.1. Median curve

Using the theory of functional data that has grown in recent years whose objectives are essentially the same as those of any other branch of statistics, that is, represent the data in a way that helps further analysis; visualize the data in order to highlight various characteristics; study important sources of pattern and variation between the data; among others (Ramsay and Silverman 2005 [43]). The median or functional half curve will be searched.

What is sought with this process is to find the curve that remains for more time in the center of the set of curves, for this the definition of depth described by Fraiman and Muniz is used [42].

Obtaining the median curve corresponding to one of the velocity functions with optimal XY values, we obtain the optimal robust XY value, which is used to find the time-depth function (equation 3) with velocity of the medium using the equation 1 and the depth in each geophone with the equation 9 and in this way obtain how the subsoil is constituted.

7. Numerical experiments

In this section, results of numerical experiments are presented; performed using the equations described in the AppendixB.1 for horizontal layers (equation B.8) and in the AppendixB.2.1 for inclined layers (equations B.31 and B.32).

Some results obtained with the data recorded in the Palmer [41] book are presented, three data sets consisting, the first with data on a flat surface and a totally irregular refractor, the second set of data has data on an irregular surface and refractor and the third one has data on a surface and an irregular refractor.

Finally, a result is presented with real data, taken in Pamplona Norte de Santander, which were supplied by the University of Pamplona and used in the thesis `Comparison of refraction seismic data and MASW, obtained with the Superone seismic equipment and the Geode24` [44] .

Whenever we use sensors we can not escape the uncertainty since in real controlled media it is very difficult to obtain same results for the same experiment at two different times at 100%; In addition, many times the same experiment is expensive and often unnecessary. For this reason, we choose to model the noise in three different ways (uniform, normal and colored) to determine the best behavior of the noise and thus be able to obtain a robust optimum.

Three types of noise modeling are taken as mentioned above. The first, a noise with uniform distribution, since it is a manageable distribution, simple and easy to program. The second, a noise with standard normal distribution generated with the Box-Muller method, this type of model is chosen since it was wanted to prioritize in the data that is obtained originally with the data collection, causing that a larger number of observations are grouped for said value obtained and decrease the quantity on both sides of the observation. And the third, noise with a colored distribution as a series with irregular temporal variability, therefore has a smooth and continuous spectrum, indicating that all frequencies in a certain range or band of frequencies are excited by this process.

The determination of the sample size of the noise simulation experiment around the obtained data (N), that is, the number of times the process is observed, essentially influences the precision of the

estimation of the robust optimum XY for that reason they performed experiments with different values for N.

7.1. Horizontal layers

A first experiment is carried out with a horizontal layer to obtain the arrival times with the equation B.8 and to be able to graph the direct and inverse times taking into account the critical point which is calculated at through the equation B.10.

For this horizontal layer, the following information is available: velocity of medium one is 1400 m/s, velocity of medium two is 4500 m/s, the total of the land horizontally is 69 meters and a separation between the 3-meter geophones for a total of 24 geophones in the terrain.

Multiple realizations were made N introducing uniform noise (ζ) to the position of the geophones to obtain different time-distance curves, with $N = 100$, $N = 500$ and $N = 1000$.

We used three different noises, $\zeta_1 \sim U$, $\zeta_2 \sim N(0, 1)$ and a red noise. In the figures 7, 8, 9 the data with a uniform noise is shown, in the figures 10, 11, 12 show the data with normal noise and finally the figures 13, 14, 15 shows the data with red noise for each selected N number of realizations.

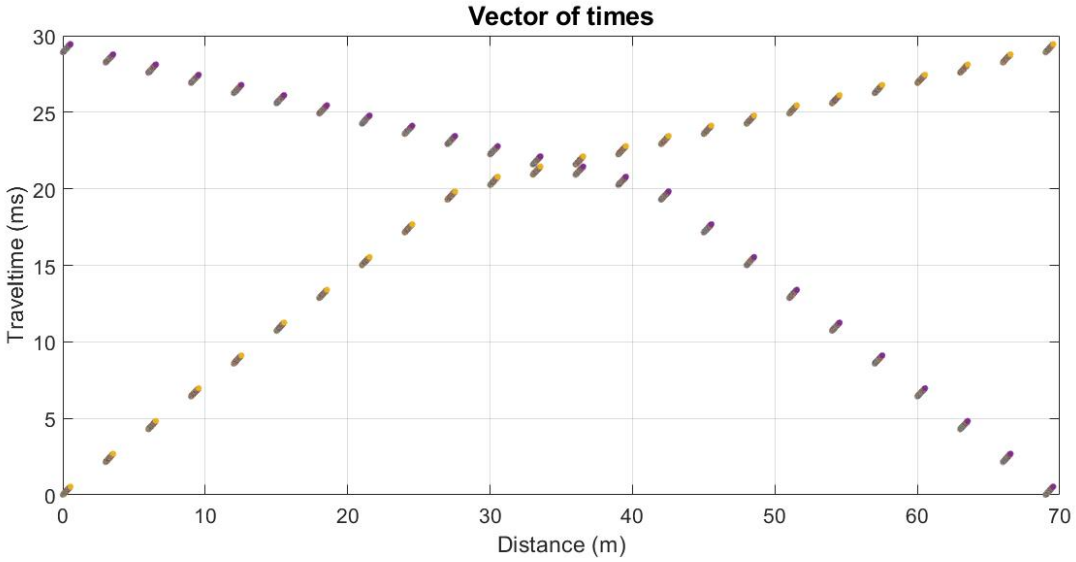

Figure 7: 100 Distance-Time curves with variation in arrival times with $\zeta_1 \sim U$

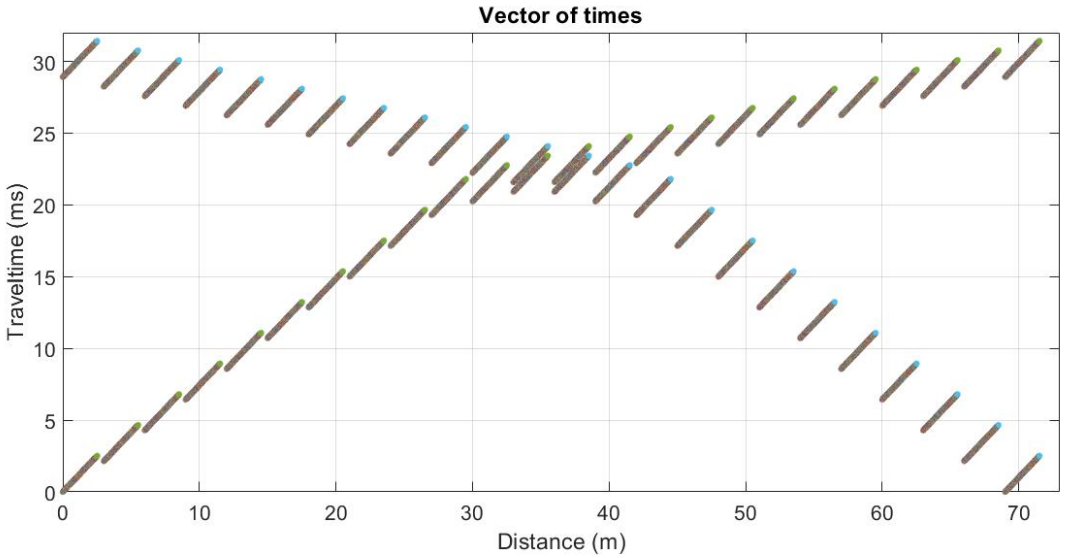

Figure 8: 500 Distance-Time curves with variation in arrival times with $\zeta_1 \sim U$

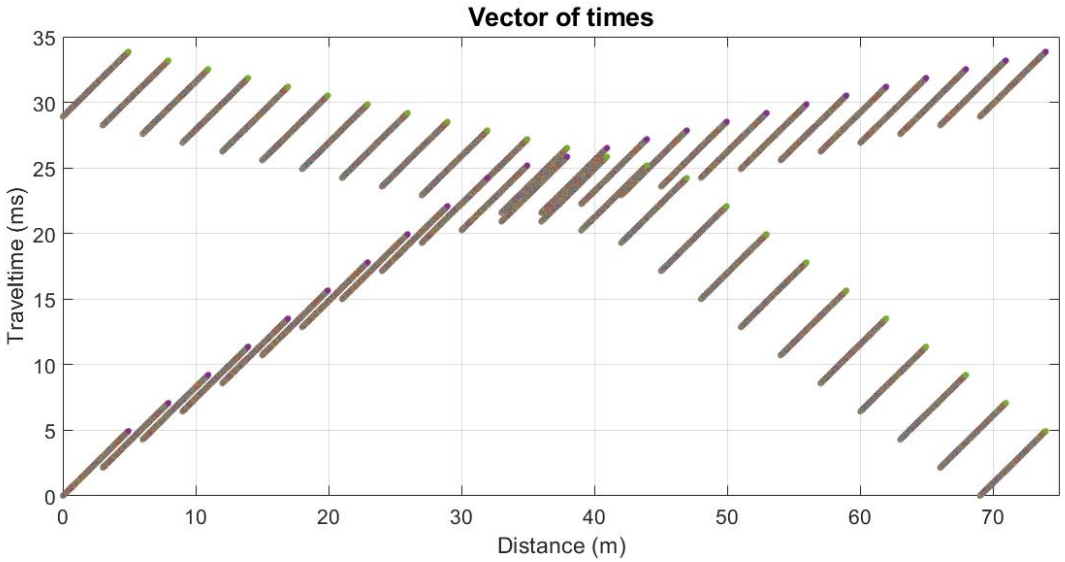

Figure 9: 1000 Distance-Time curves with variation in arrival times with $\zeta_1 \sim U$

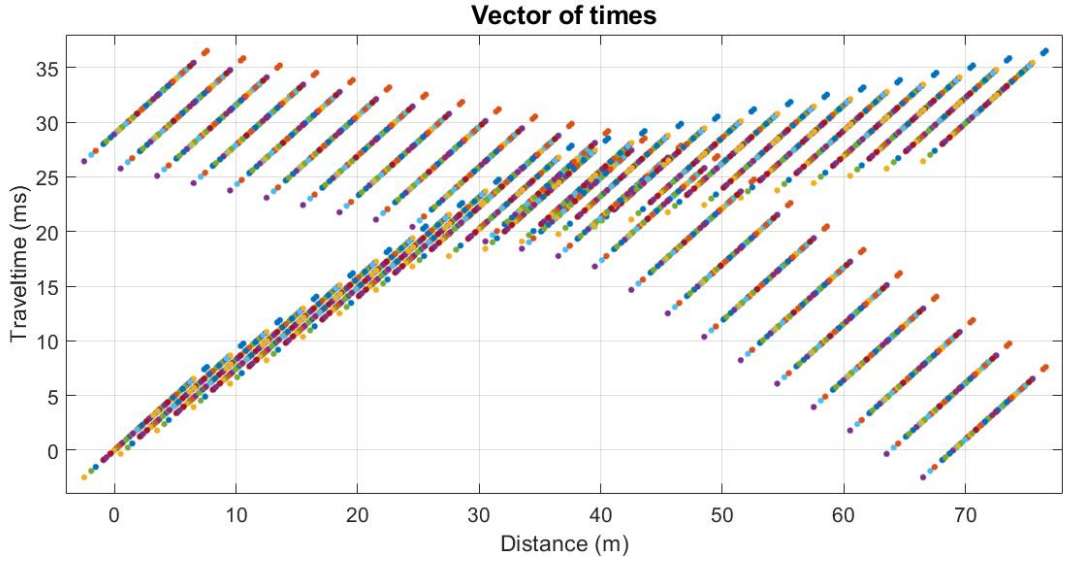

Figure 10: 100 Distance-Time curves with variation in arrival times with $\zeta_2 \sim N(0,1)$

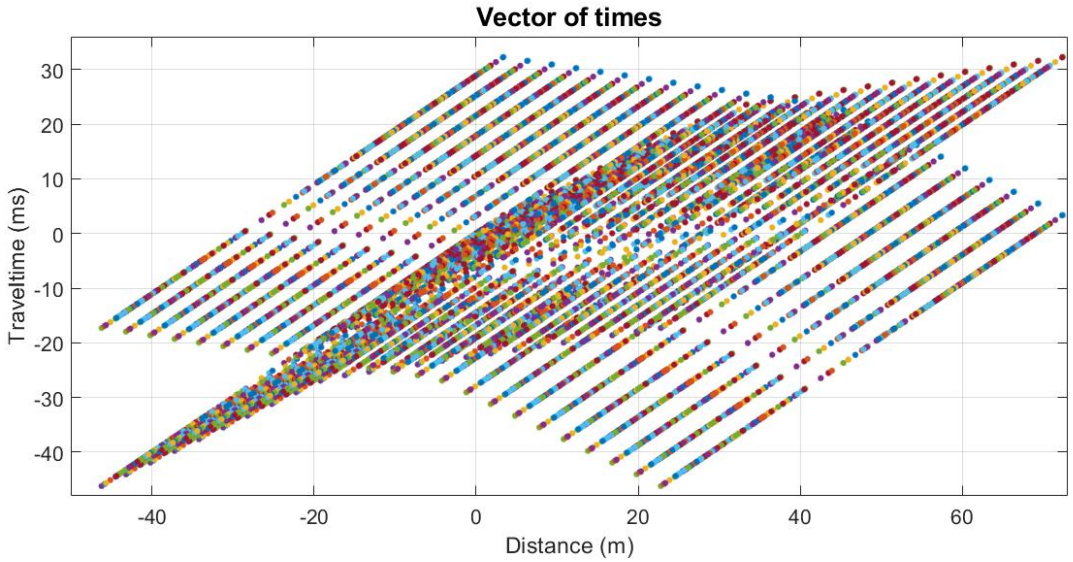

Figure 11: 500 Distance-Time curves with variation in arrival times with $\zeta_2 \sim N(0,1)$

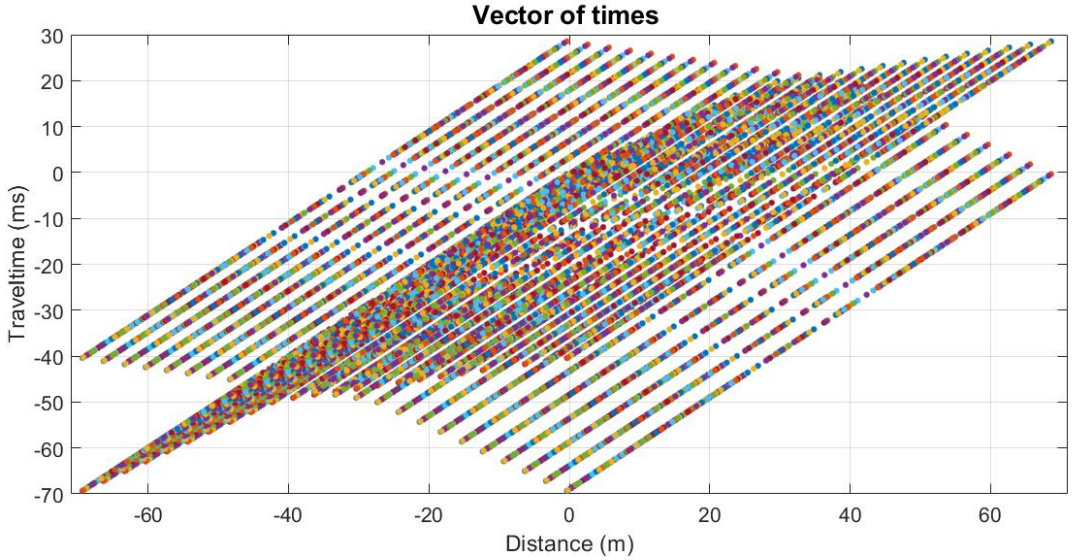

Figure 12: 1000 Distance-Time curves with variation in arrival times with $\zeta_2 \sim N(0,1)$

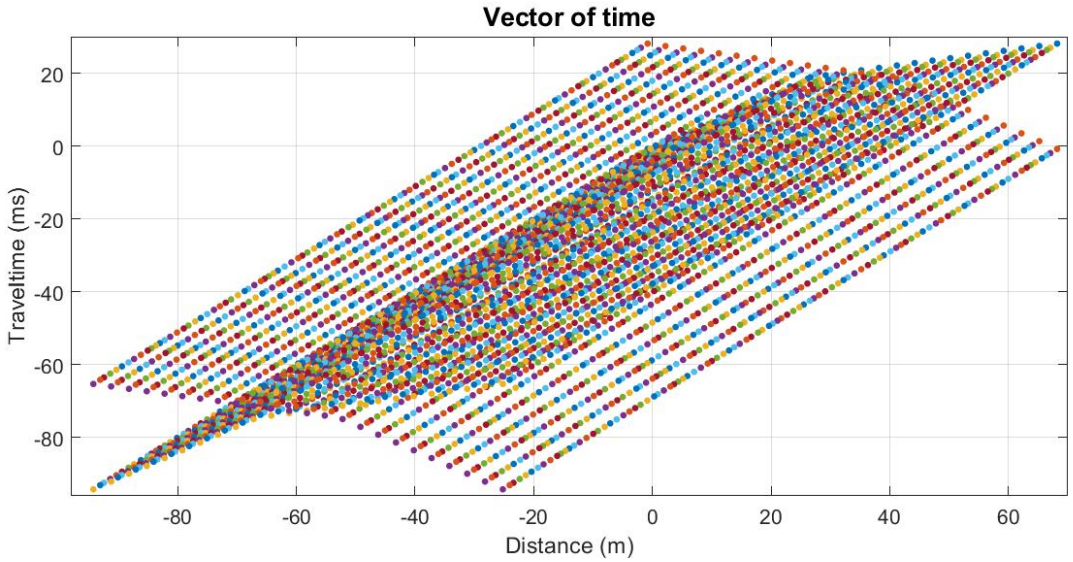

Figure 13: 100 Distance-Time curves with variation in their arrival times with red noise

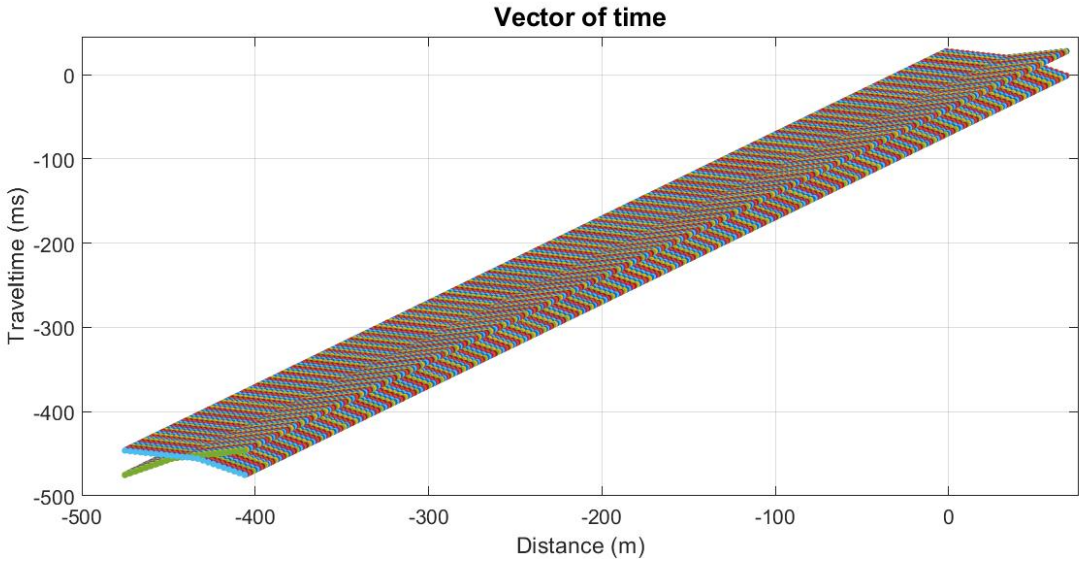

Figure 14: 500 Distance-Time curves with variation in their arrival times with red noise

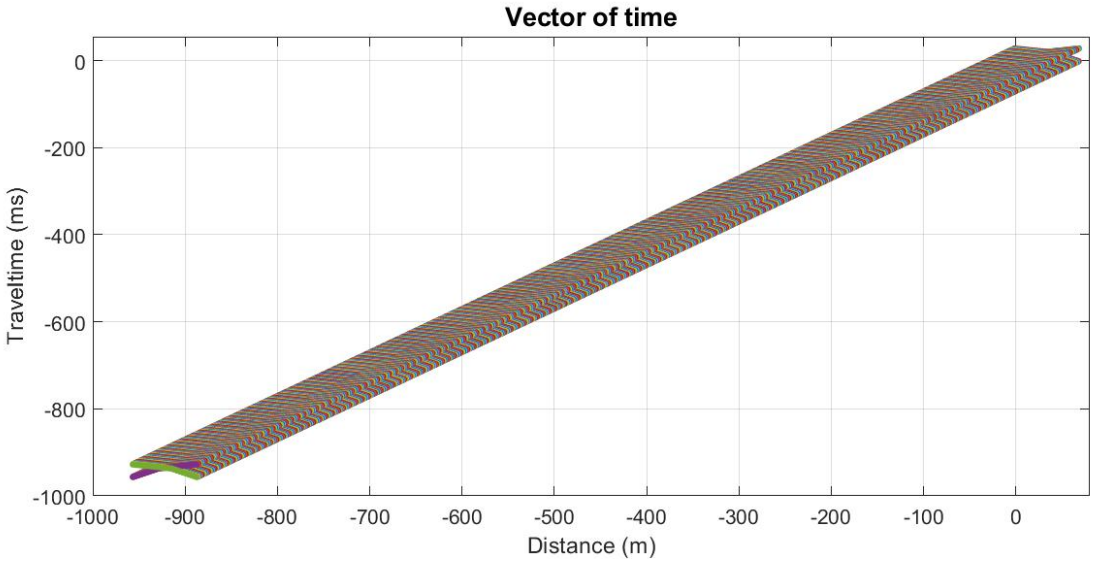

Figure 15: 1000 Distance-Time curves with variation in their arrival times with red noise

For each of the previous vector of times graphs, the velocity analysis function is calculated and each group has its respective optimal XY, thus generating an optimum velocity analysis function curve to then determine the median curve. Within each group (figures 16, 17, 18), regardless of the type of noise incorporated, the solution is the same.

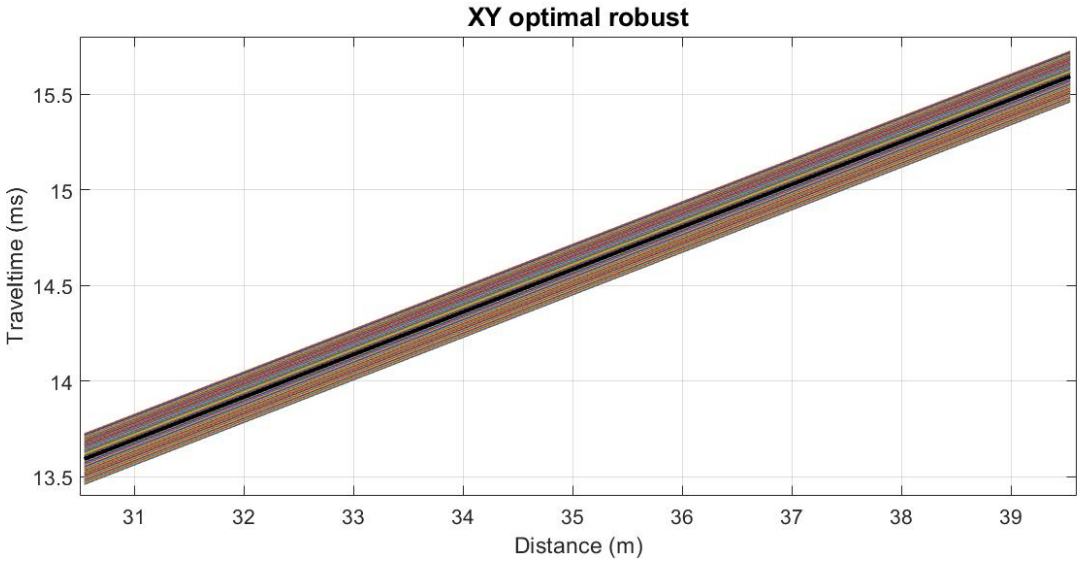

Figure 16: Median of 100 optimal XY curves

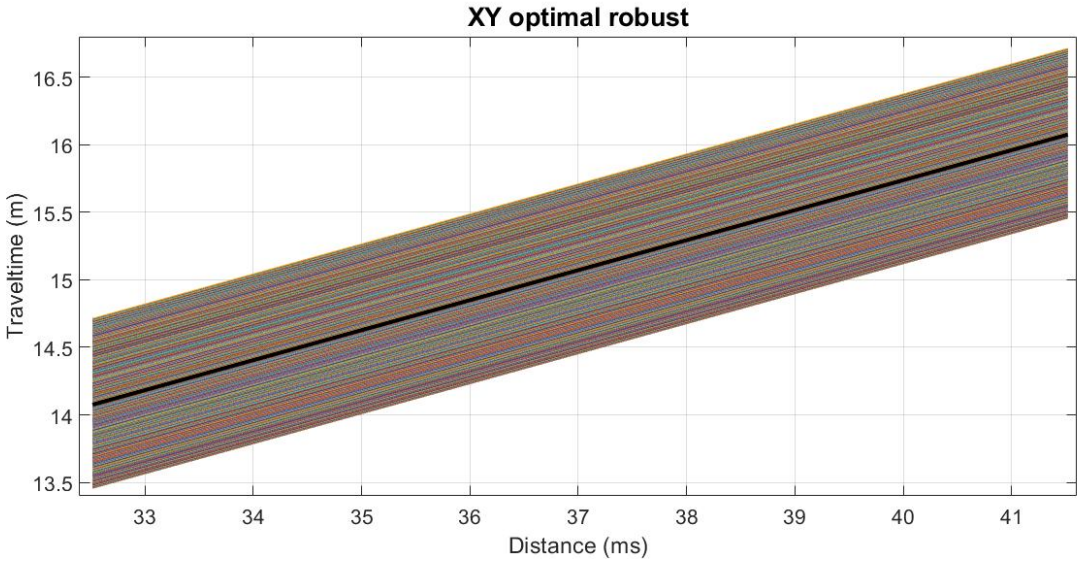

Figure 17: Median of 500 optimal XY curves

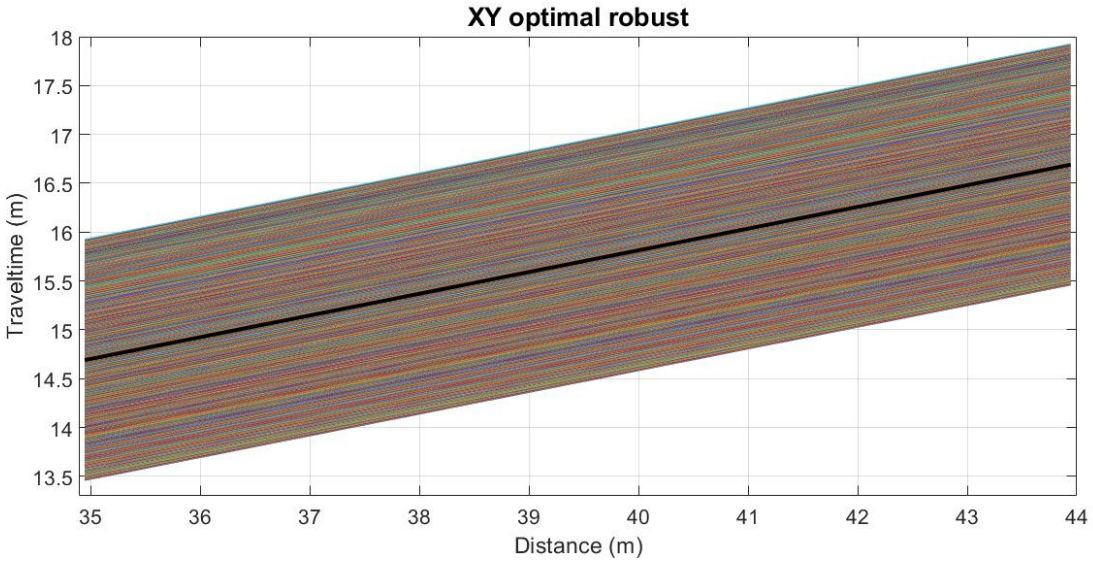

Figure 18: Median of 1000 optimal XY curves

For which the result of the XY optimum is 30 meters and the speed of medium two is $4500m/s$ as expected.

7.2. Inclined Layers

A second experiment was carried out with inclined layers, for which the soiling times were generated with the equations B.31 and B.32, with a distance between the geophones of 5 meters, covering a horizontal terrain of 120 meters.

The speed of the first layer is 400 m/s and the second layer of 1500 m/s, an angle of inclination of four degrees and a depth greater than 20 meters and less than 11.6 meters, for the two disturbances. In this case, the figures 19, 20 and 21 are obtained with $\zeta_1 \sim U$, the figures 22, 23 and 24 with $\zeta_1 \sim N(0,1)$ and the figures 25, 26 and 27 with white noise, for N $=$ 100, N $=$ 500 and N $=$ 1000 respectively where N is the number of Distance-vs-Time graphs after introducing noise to the position of the geophones to generate the different curves.

For this experiment, a robust XY optimal of 40 meters and a velocity of $1571.3339m/s$ was found.

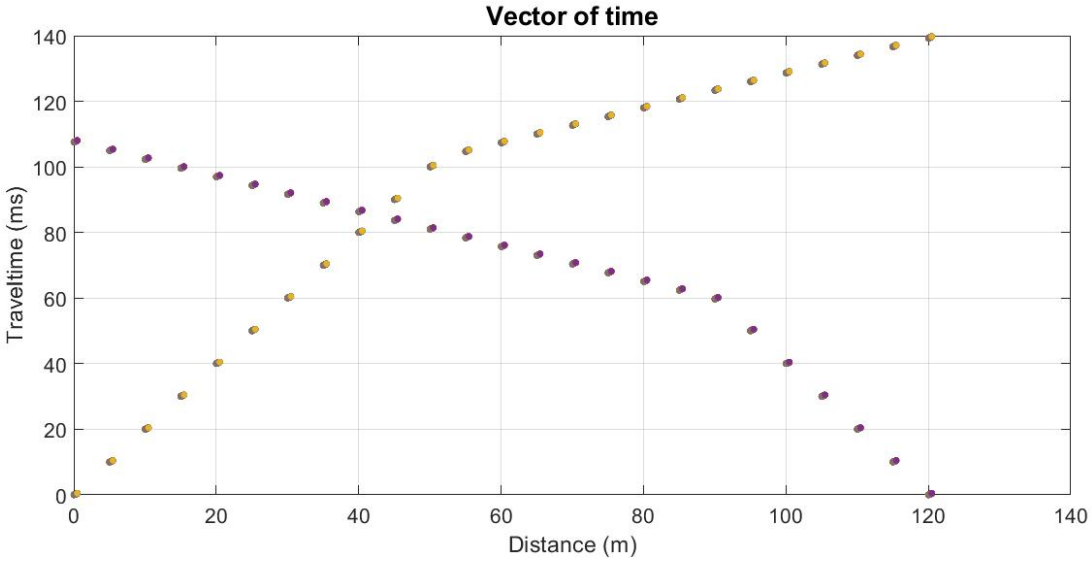

Figure 19: 100 Distance-Time curves with variation in their arrival times with $\zeta_1 \sim U$

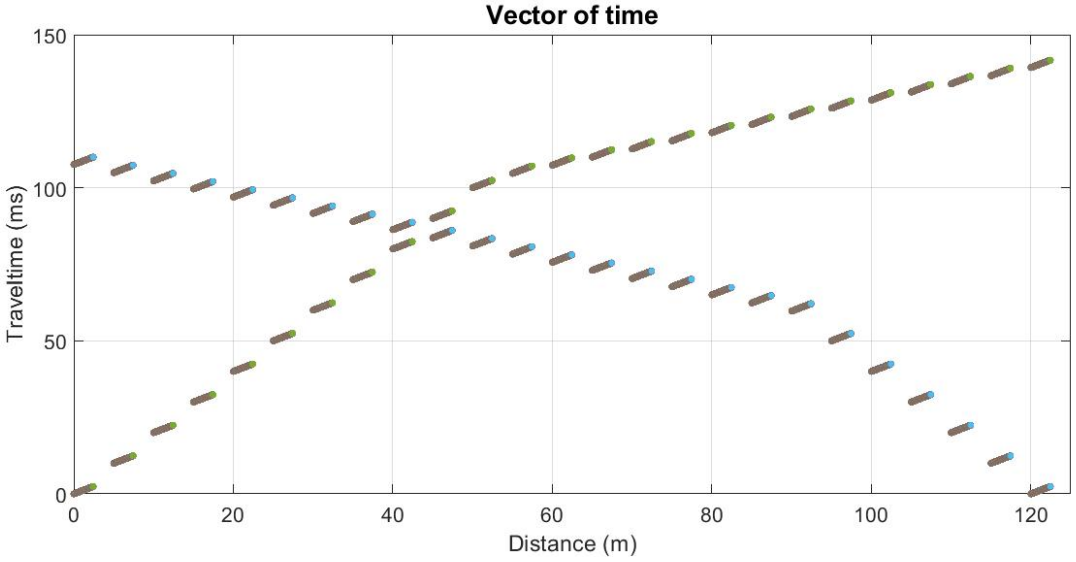

Figure 20: 500 Distance-Time curves with variation in their arrival times with $\zeta_1 \sim U$

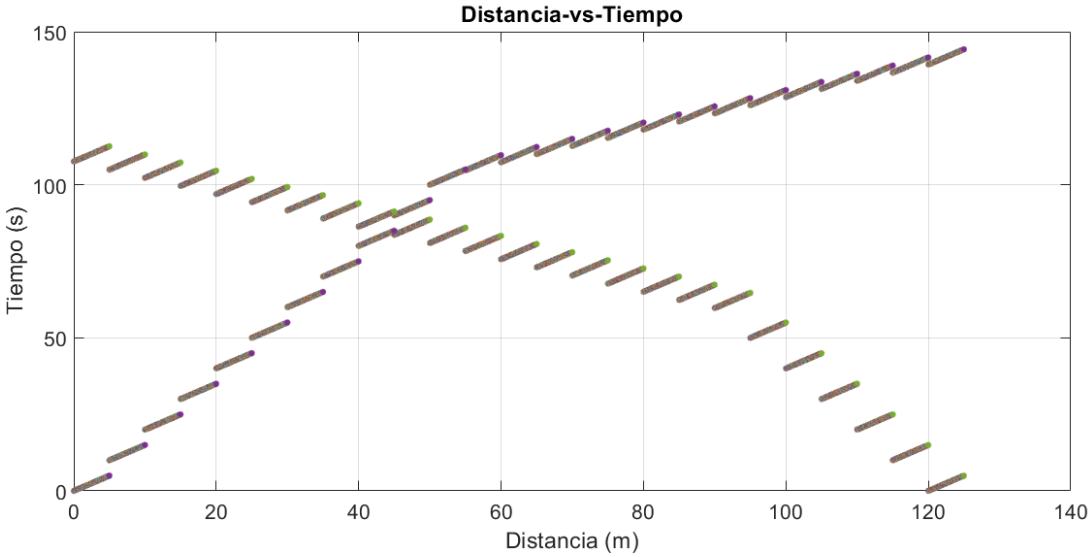

Figure 21: 1000 Distance-Time curves with variation in their arrival times with $\zeta_1 \sim U$

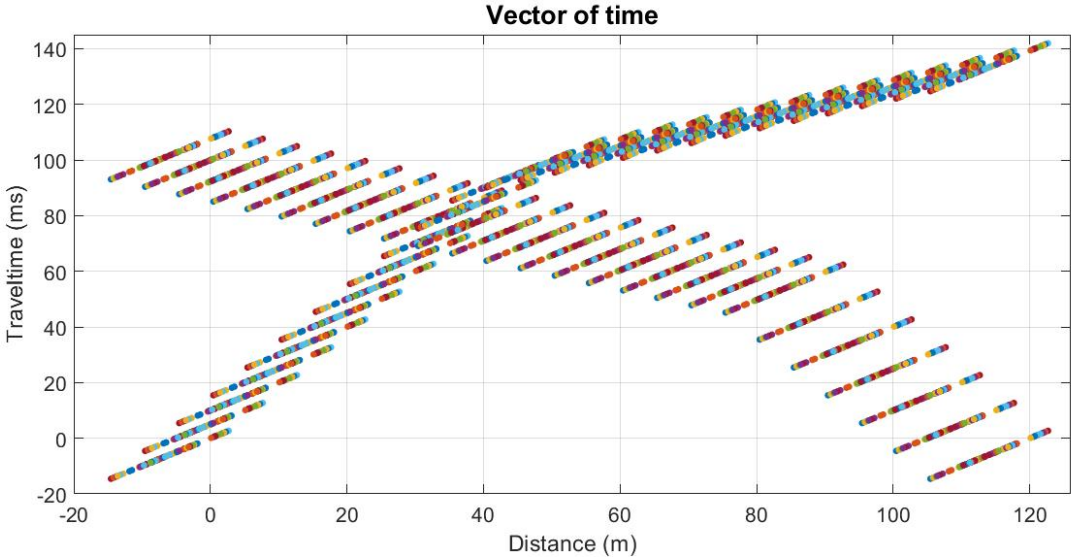

Figure 22: 100 Distance-Time curves with variation in their arrival times with $\zeta_2 \sim N(0,1)$

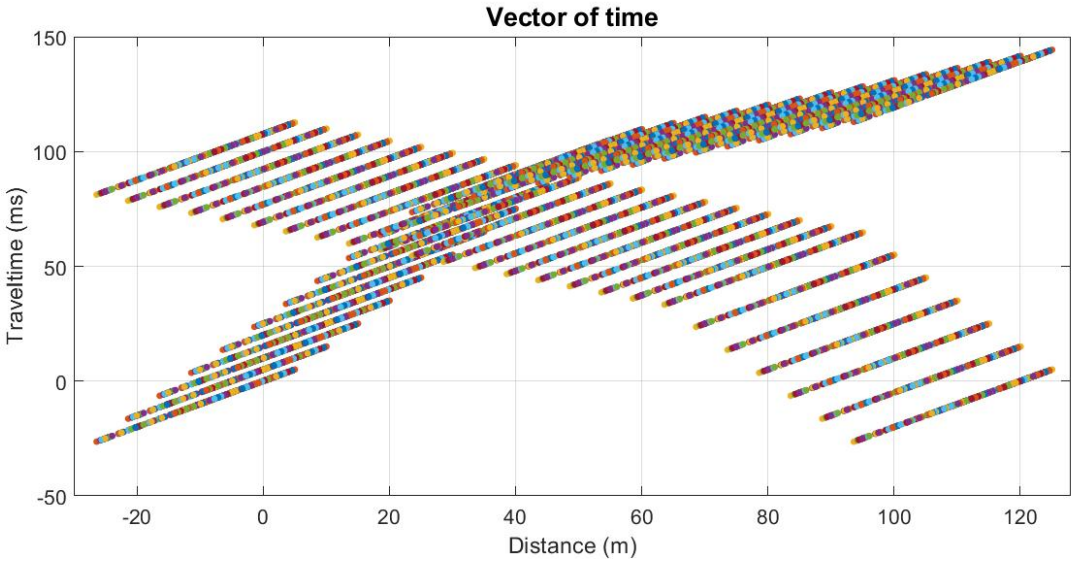

Figure 23: 500 Distance-Time curves with variation in their arrival times with $\zeta_2 \sim N(0,1)$

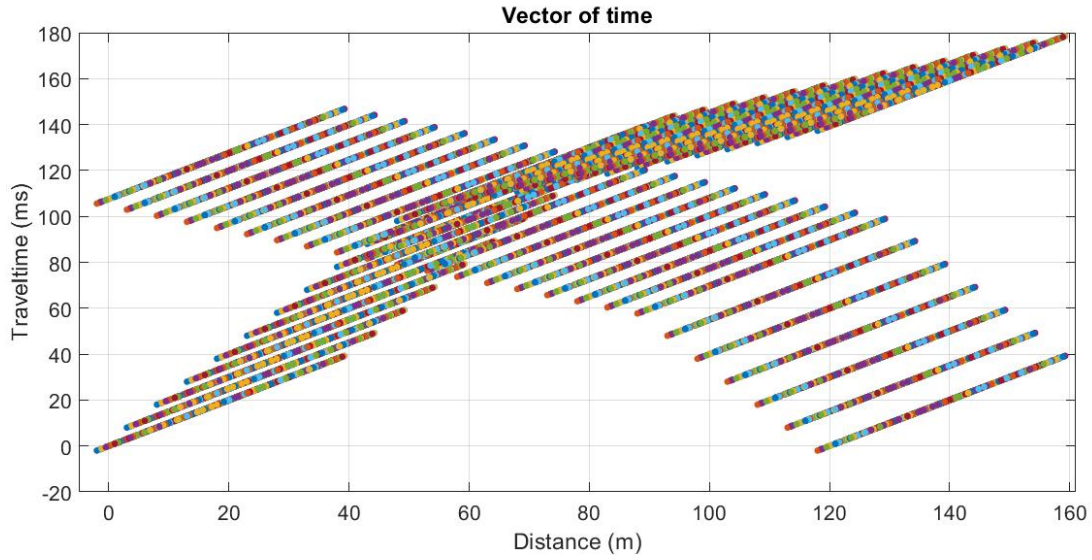

Figure 24: 1000 Distance-Time curves with variation in their arrival times with $\zeta_2 \sim N(0,1)$

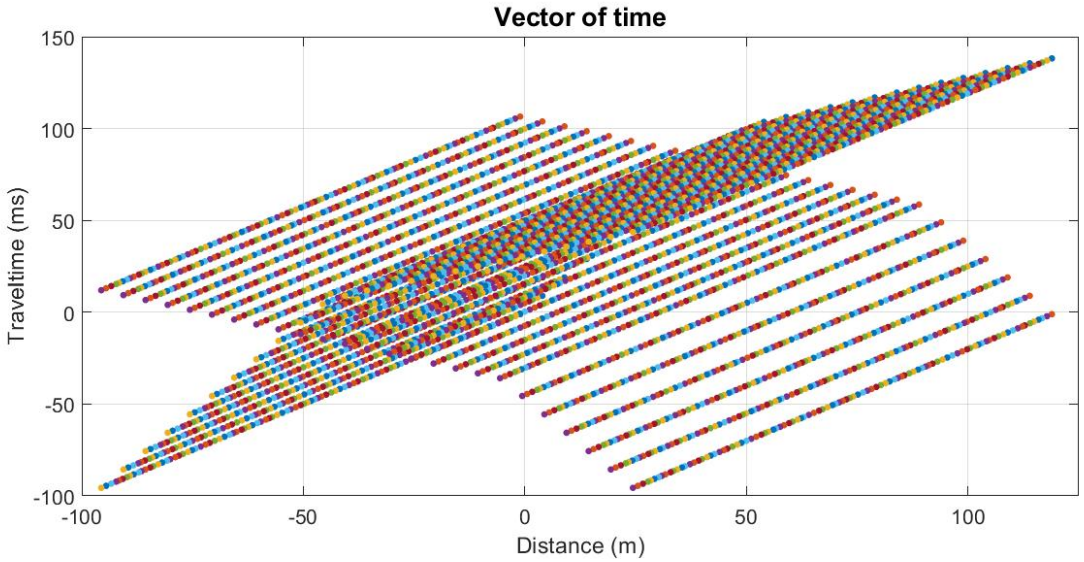

Figure 25: 100 Distance-Time curves with variation in their arrival times with red noise

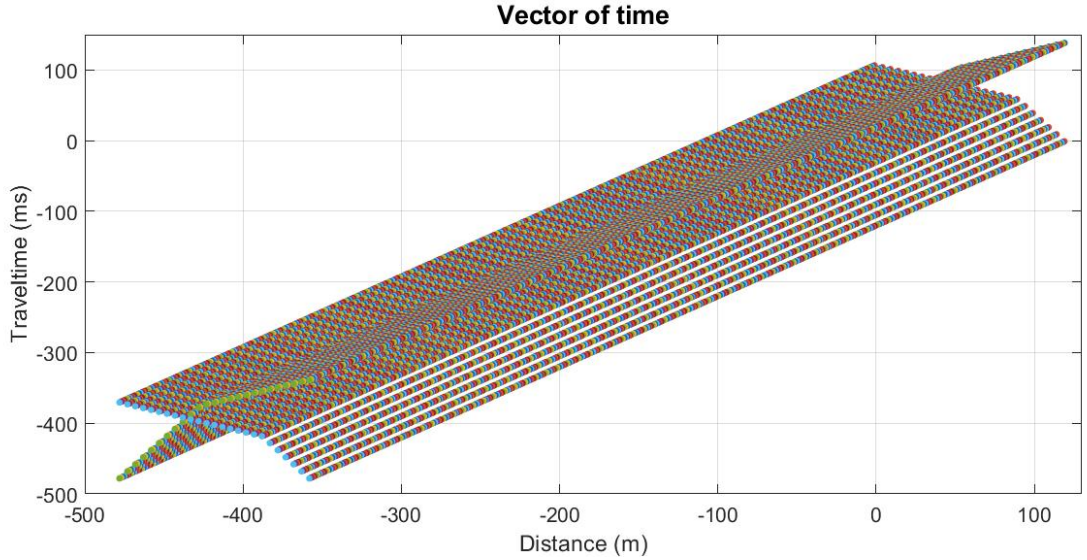

Figure 26: 500 Distance-Time curves with variation in their arrival times with red noise

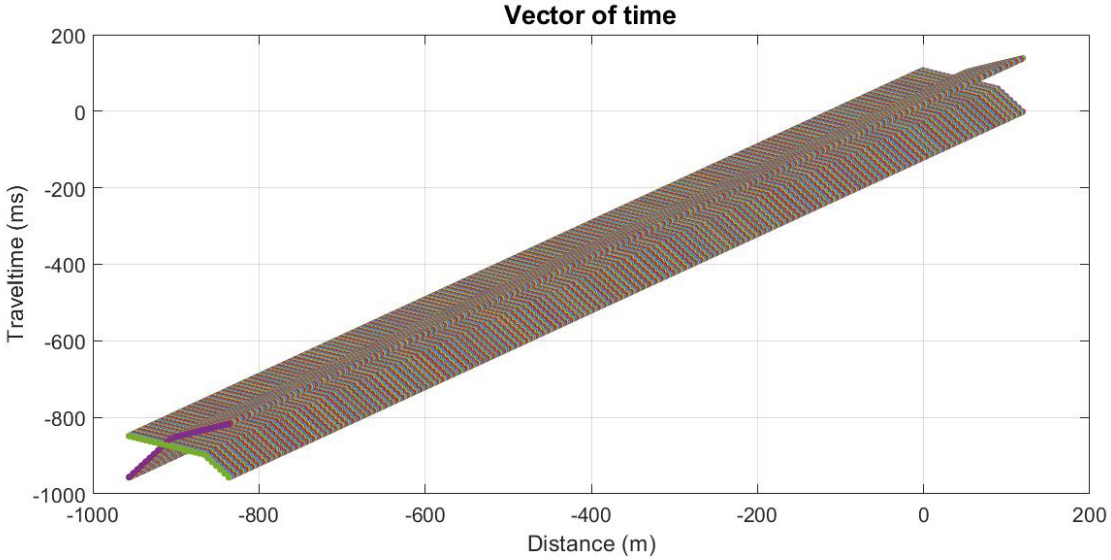

Figure 27: 1000 Distance-Time curves with variation in their arrival times with red noise

As in the first experiment, the optimum is drawn for each curve and then plotted to find the median of all the curves obtained and find the robust XY optimal (figures 28, 29 and 30), in this case regardless of the noise the solution is the same.

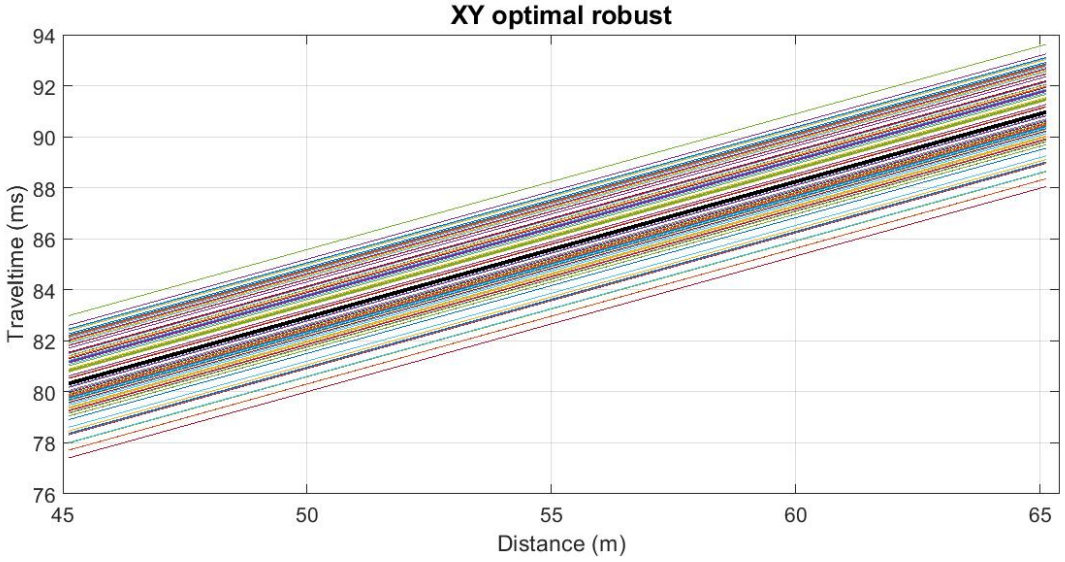

Figure 28: Median of 100 optimal XY curves

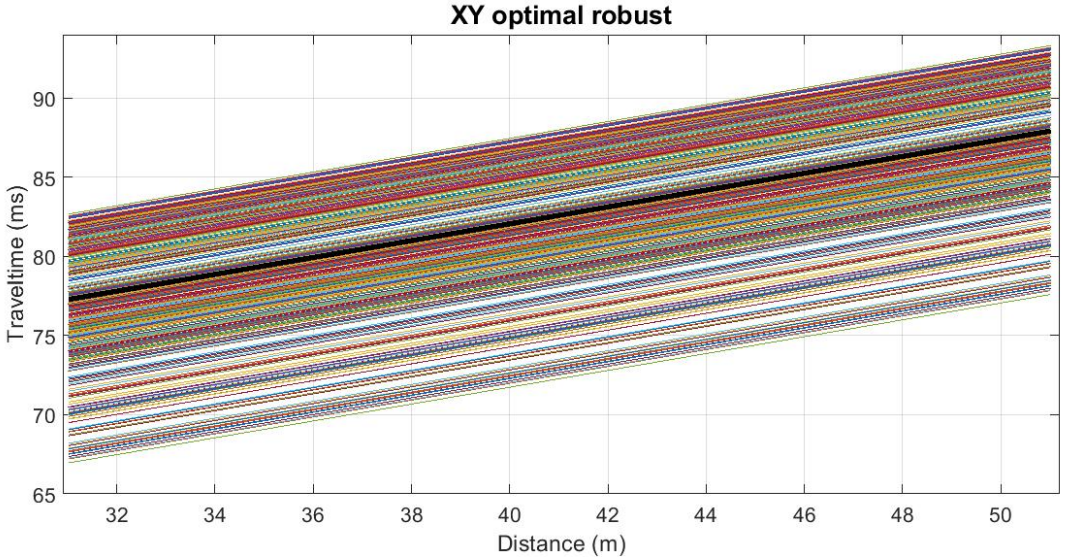

Figure 29: Median of 500 optimal XY curves

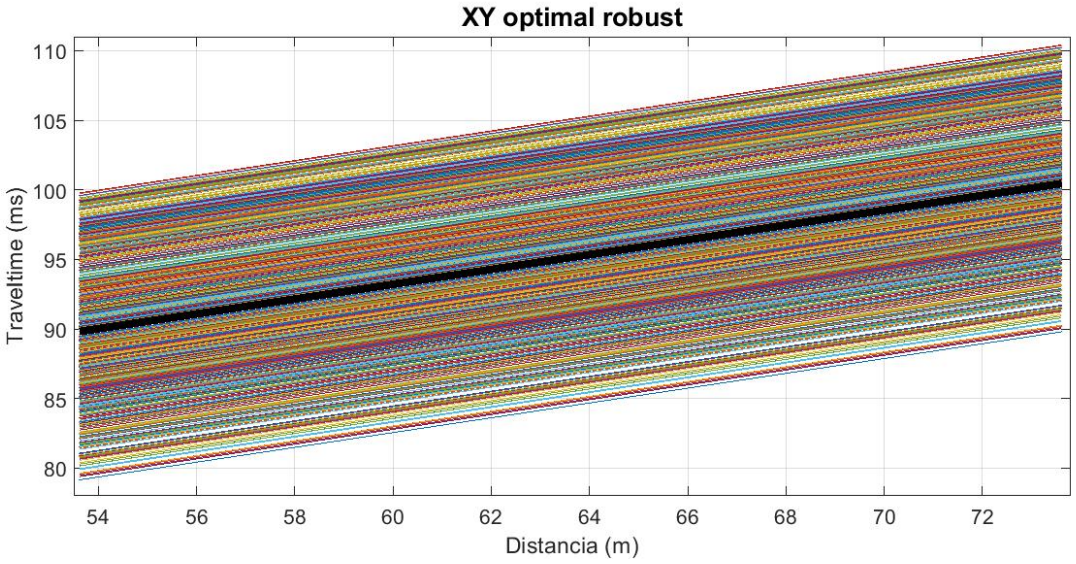

Figure 30: Median of 1000 optimal XY curves

7.3. Palmer's book dataset information

In a third experiment, three databases were taken from Palmer [41], to perform the same procedure as in the previous experiments, that is, the positions of the geophones and the arrival times are incorporated a noise N of times to get N curves away from time and each find the optimal XY and then have the optimal XY sturdy.

Base 1. This base has data on a flat surface and a totally irregular refractor, the geophones are placed every 5 meters to cover 335 meters in total as shown in the figure 31.

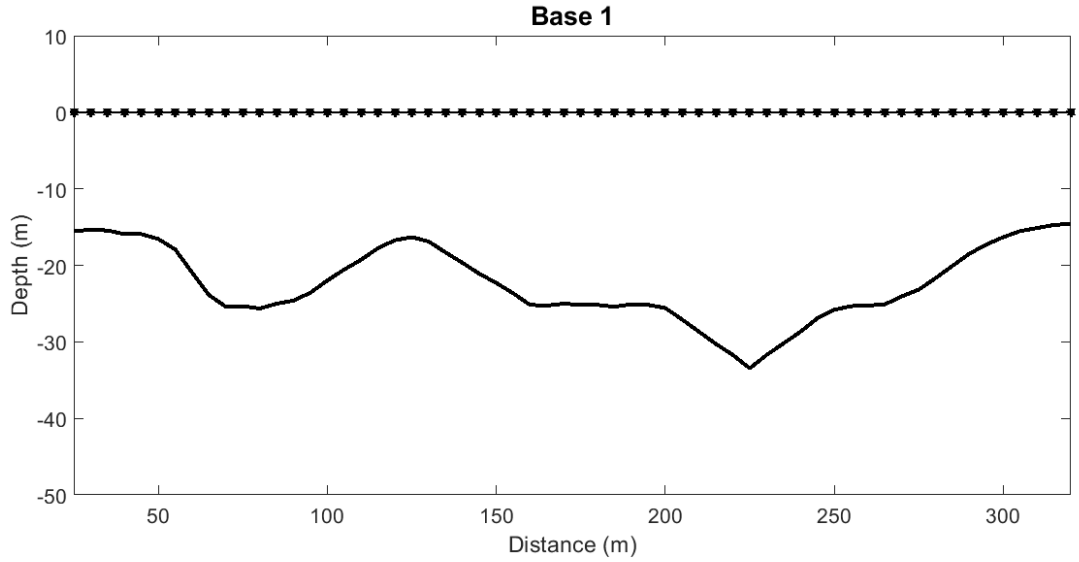

Figure 31: Simulated data with flat surface and irregular refractor.

This base has the arrival times to which a noise is applied as stated above and in this way 100, 500 and 1000 Distance-vs-Time curves are obtained, the figures 32, 33 and 34 correspond to $\zeta_1 \sim U$, the figures 35, 36 and 37 correspond to $\zeta_2 \sim N(0,1)$ and finally the figures 38, 39 and 40 correspond to red noise.

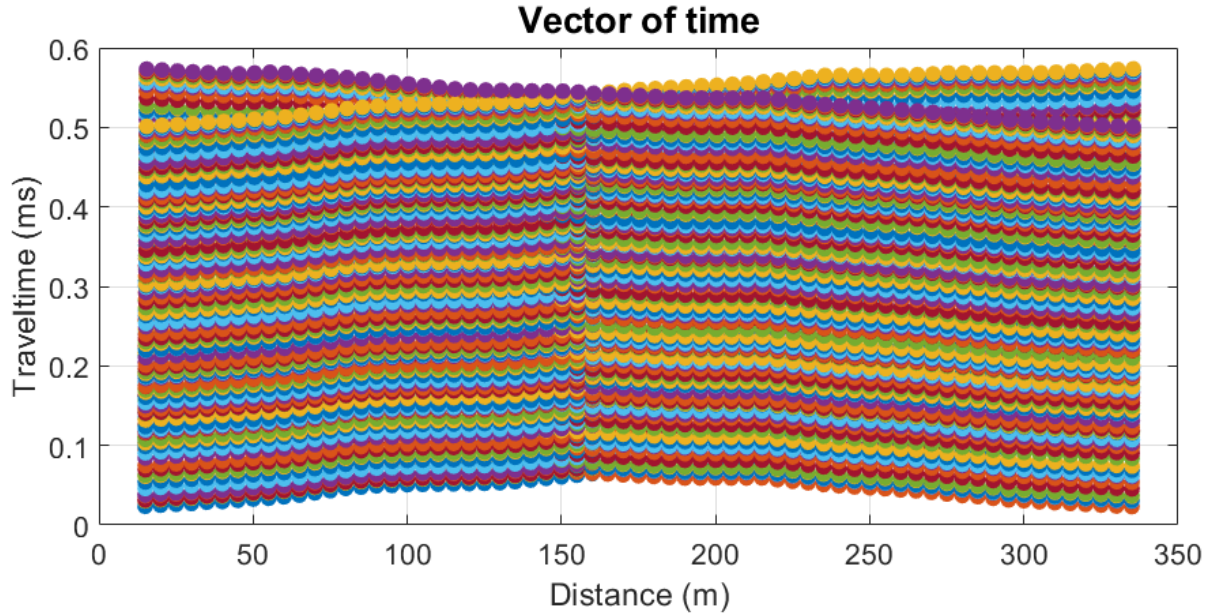

Figure 32: 100 arrival times curves for the simulated data with $\zeta_1 \sim U$

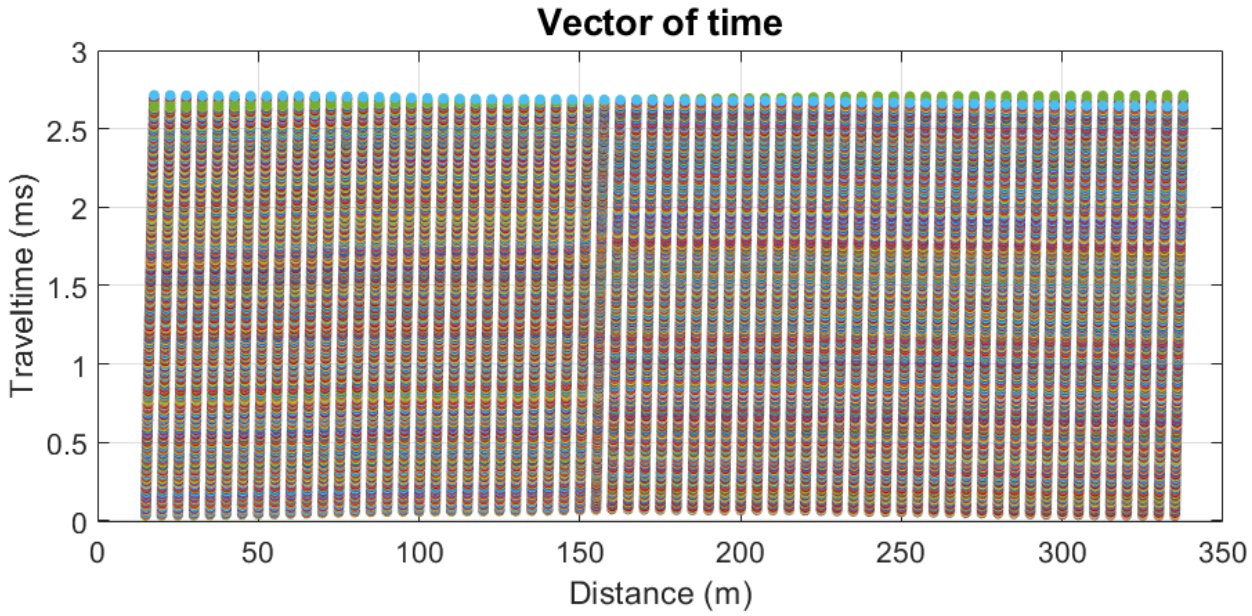

Figure 33: 500 arrival times curves for the simulated data with $\zeta_1 \sim U$

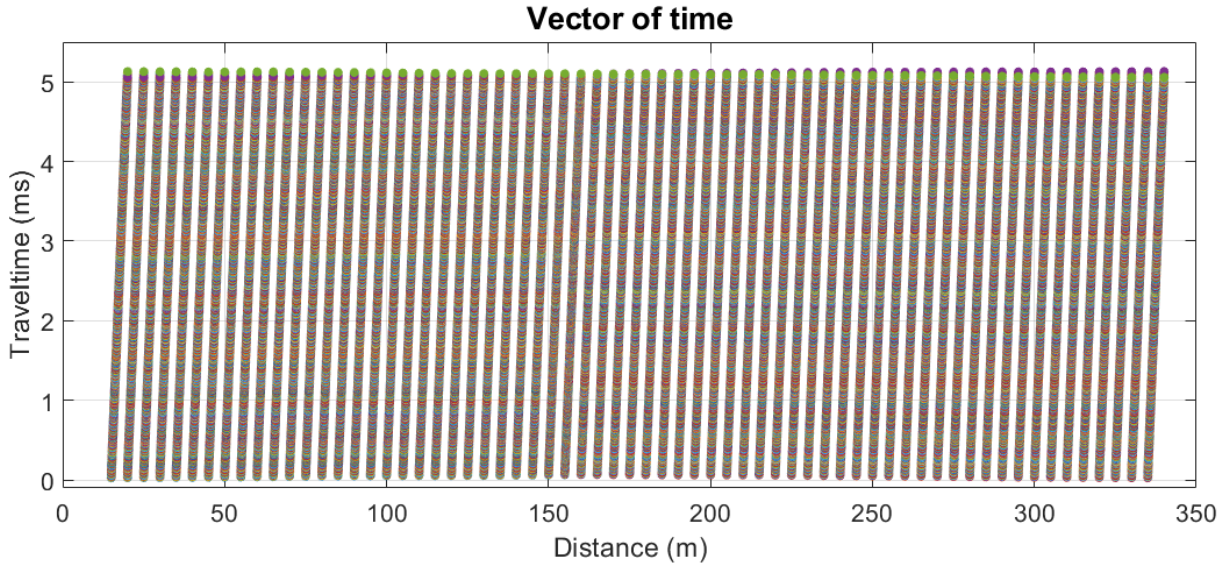

Figure 34: 1000 arrival times curves for the simulated data with $\zeta_1 \sim U$

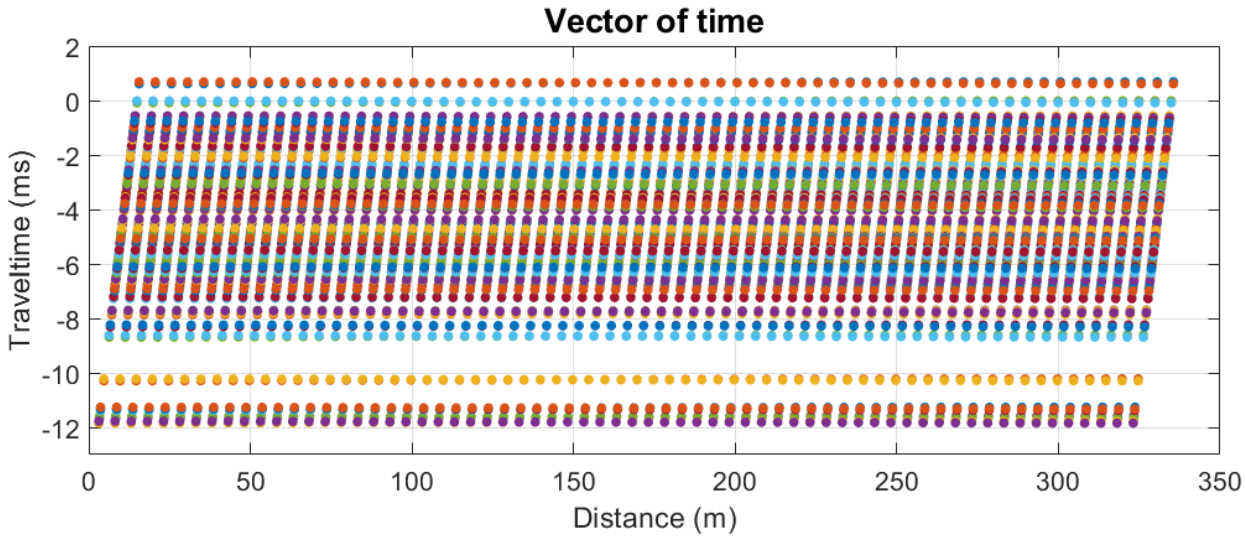

Figure 35: 100 arrival times curves for the simulated data with $\zeta_1 \sim N(0, 1)$

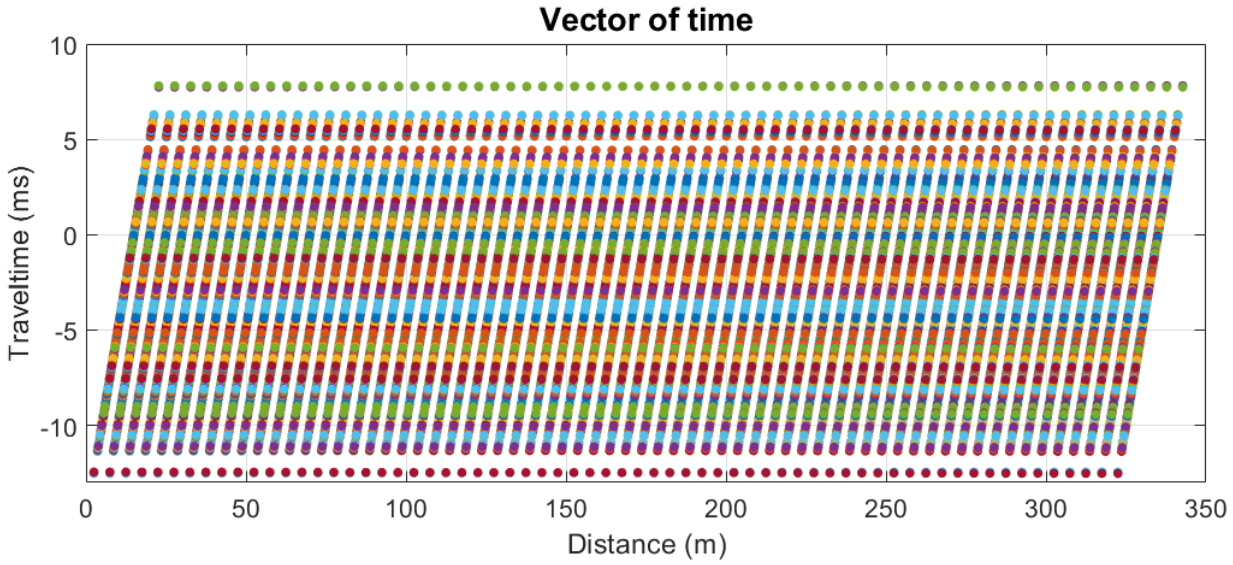

Figure 36: 500 arrival times curves for the simulated data with $\zeta_1 \sim N(0,1)$

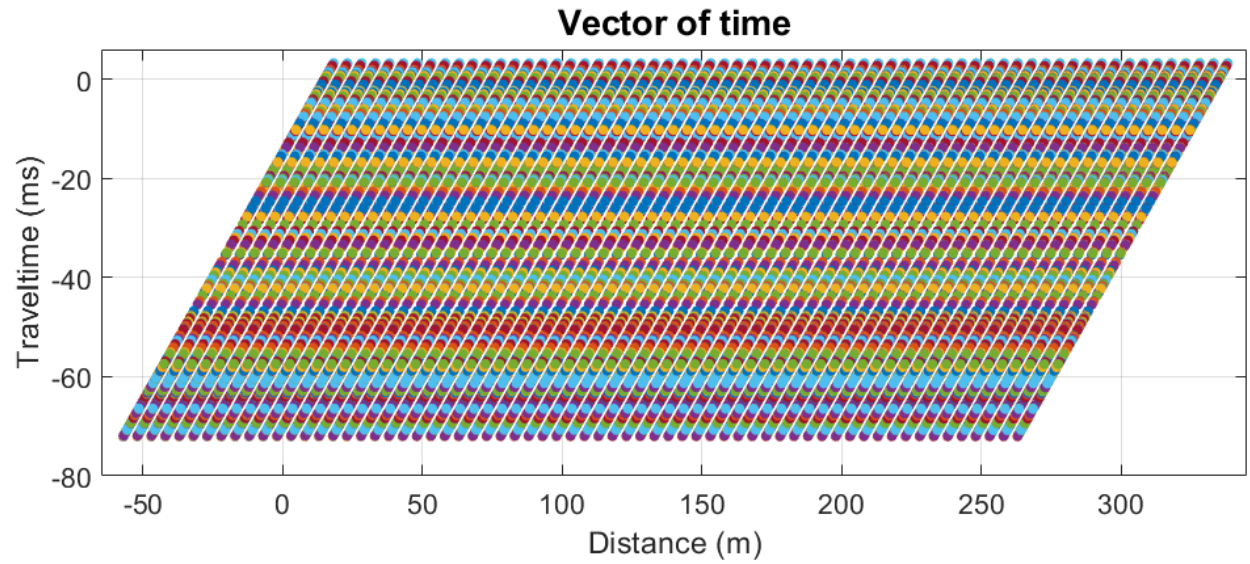

Figure 37: 1000 arrival times curves for the simulated data with $\zeta_1 \sim N(0,1)$

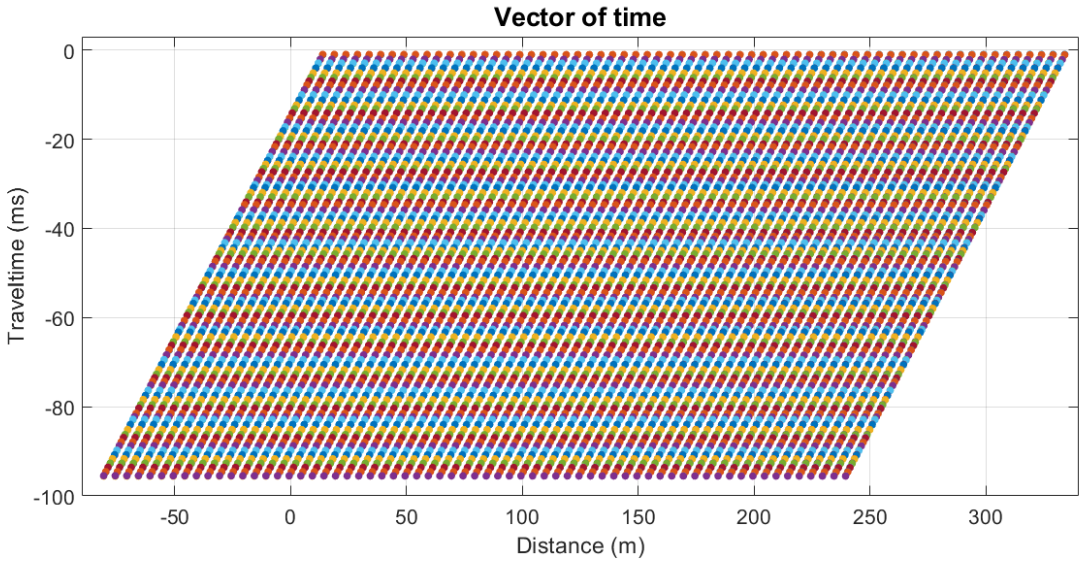

Figure 38: 100 arrival times curves for simulated data with red noise

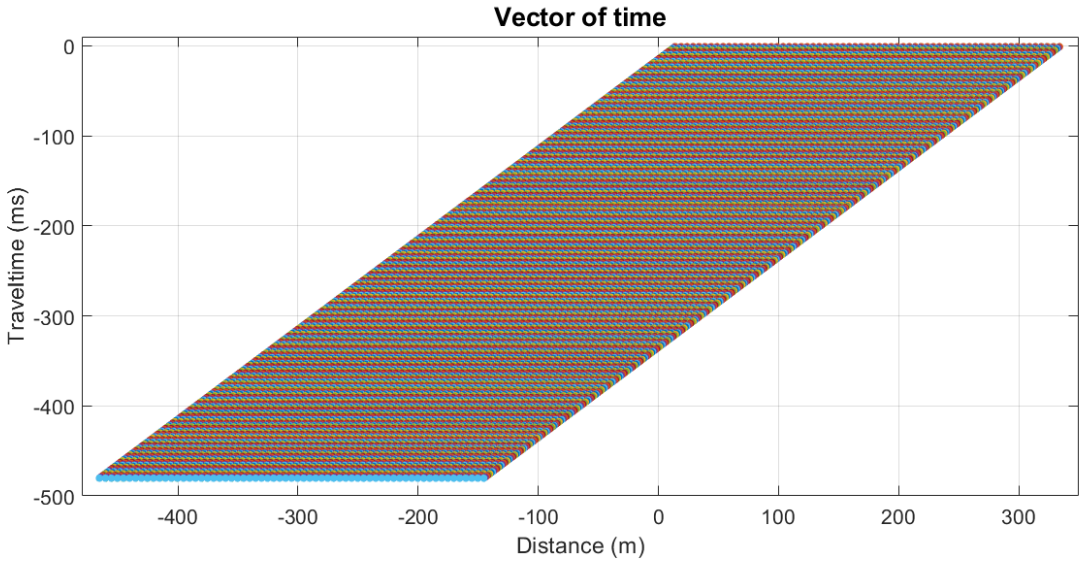

Figure 39: 500 arrival times curves for simulated data with red noise

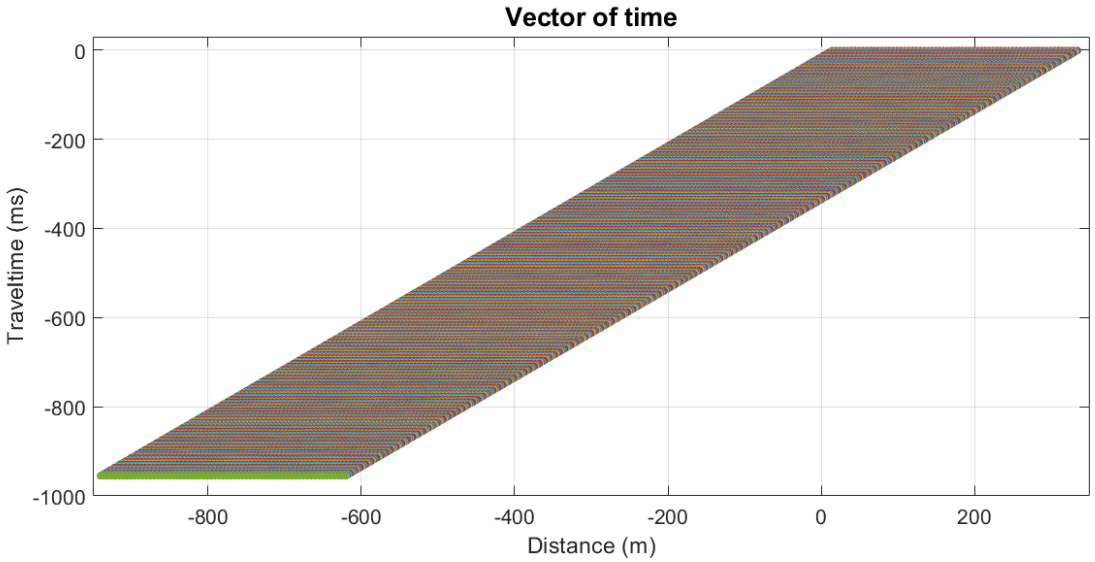

Figure 40: 1000 arrival times curves for simulated data with red noise

The search is made for the XY optimal robust, finding the median of the curves of the optimal XY for Distance-Time curve. The curve was generated after incorporating the noise to the data. Then, the calculus of the velocities of the medium and the depth of the refractor was made with the equations 1 and 9 respectively.

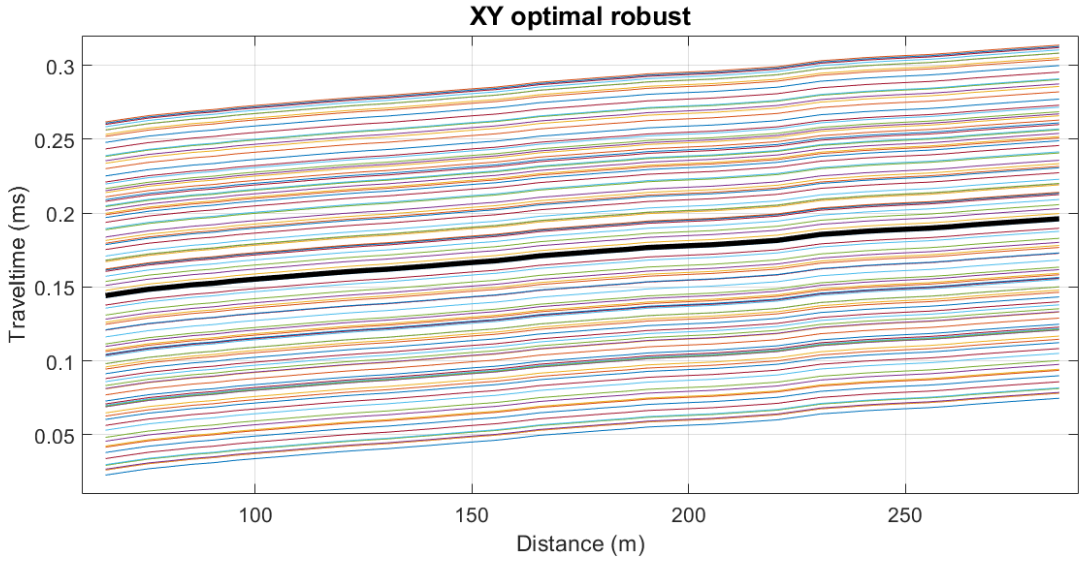

Figure 41: Median of 100 optimal XY curves

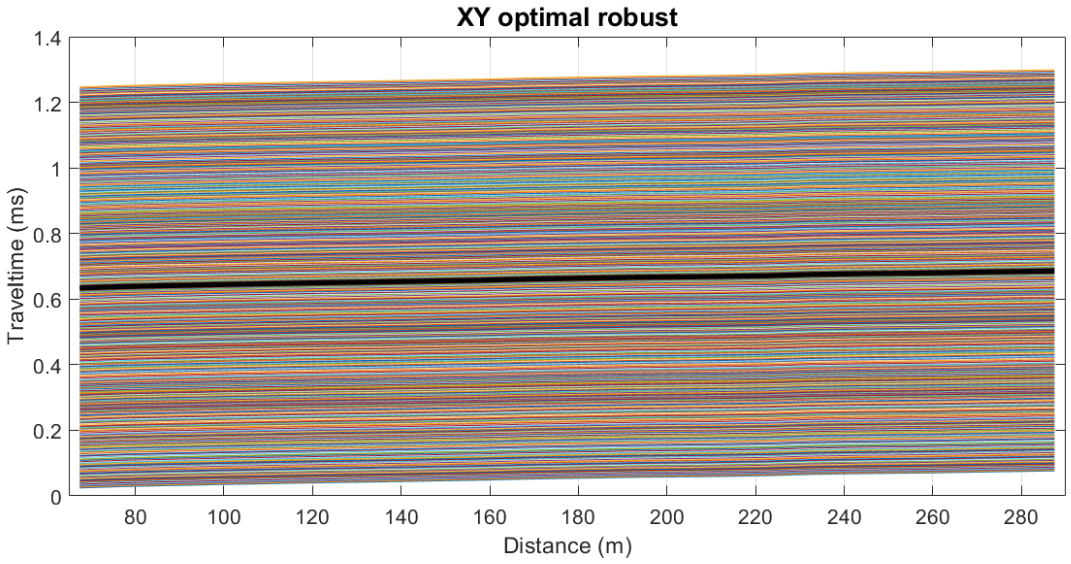

Figure 42: Median of 500 optimal XY curves

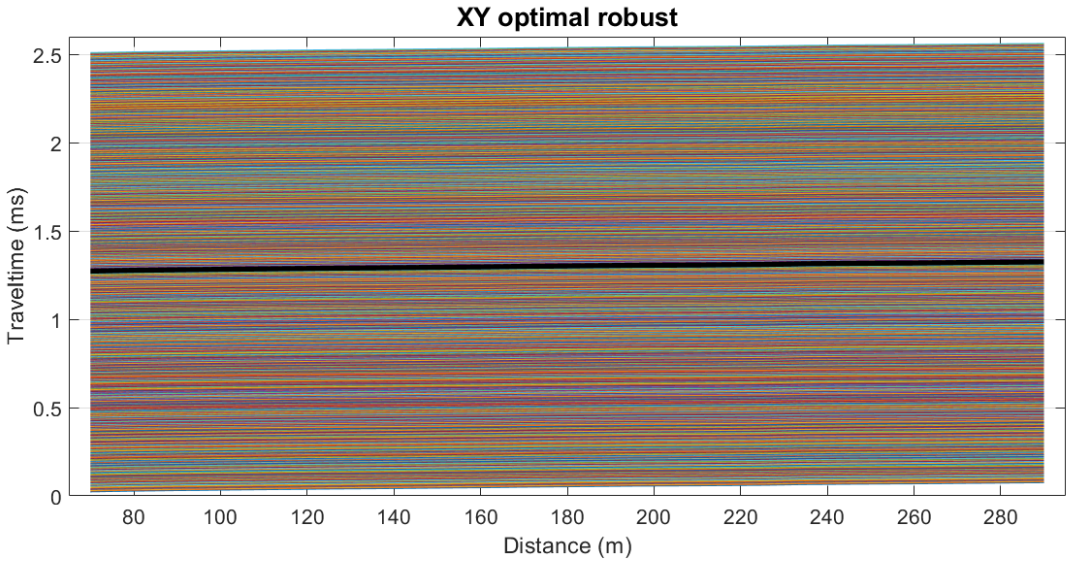

Figure 43: Median of 1000 optimal XY curves

In the figures 41, 42 and 43 are shown the medians found for which in all cases it is determined that the XY optimal robust is 20 meters and the speed of the refractor is of 4421.518055 m/s. In the figure 44 the depth found compared to the given depth of the simulated data is observed.

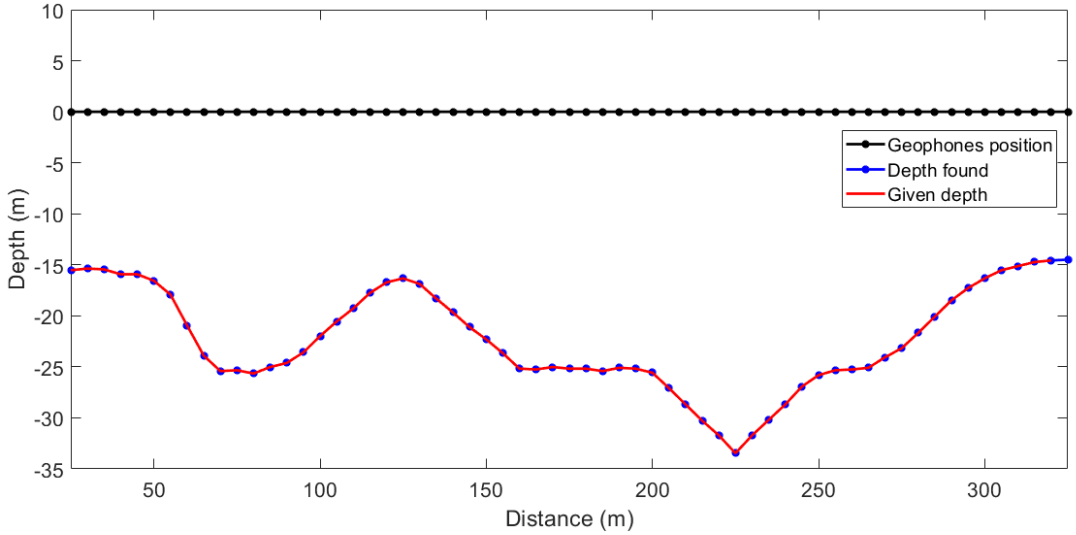

Figure 44: Depth found for the simulated data compared to the given depth.

Base 2. This base has data about an irregular surface and refractor, the geophones are placed every 5 meters to cover a total of 350 meters as shown in the figure 45.

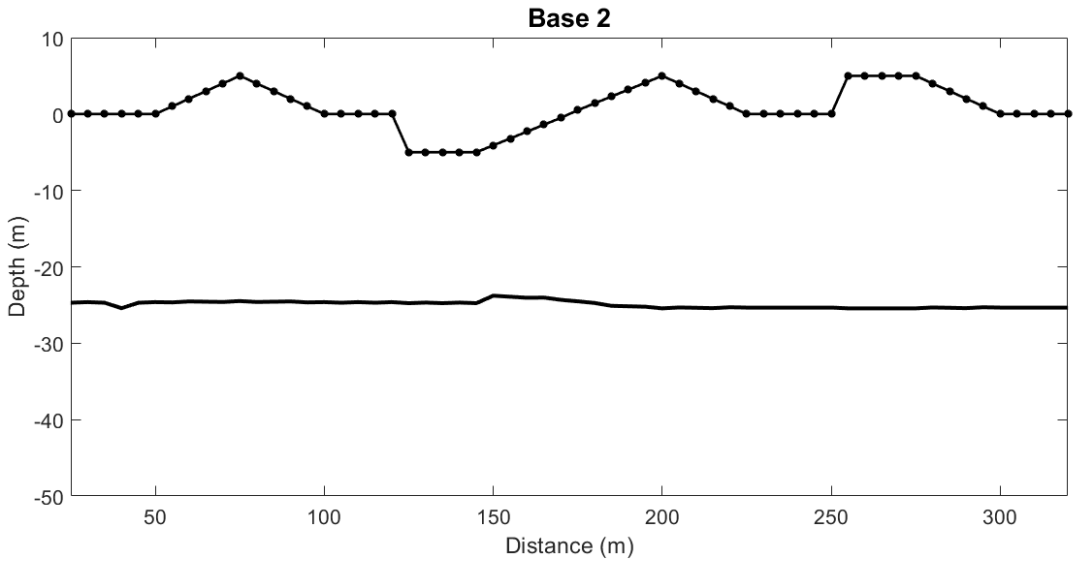

Figure 45: Simulated data with irregular surface and refractor.

In the figures 46, 47 and 48 we have the arrival data with ζ_1; in the figures 49, 50 and 51 are the arrival data with ζ_2 and the figures 52, 53 and 54 with red noise for 100, 500 and 1000 Distance-Time curves.

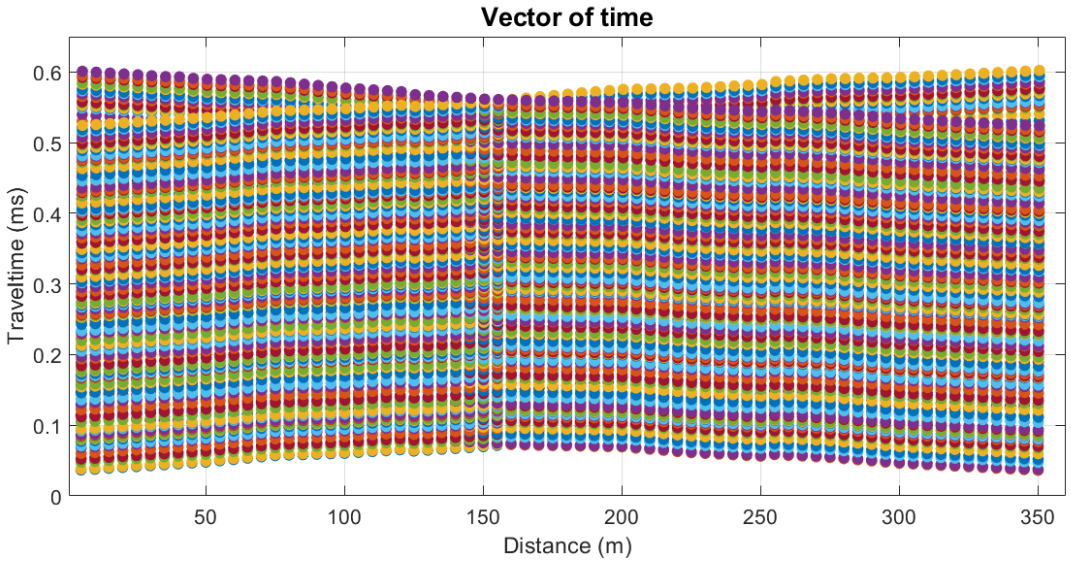

Figure 46: 100 arrival times curves for the simulated data with ζ_1

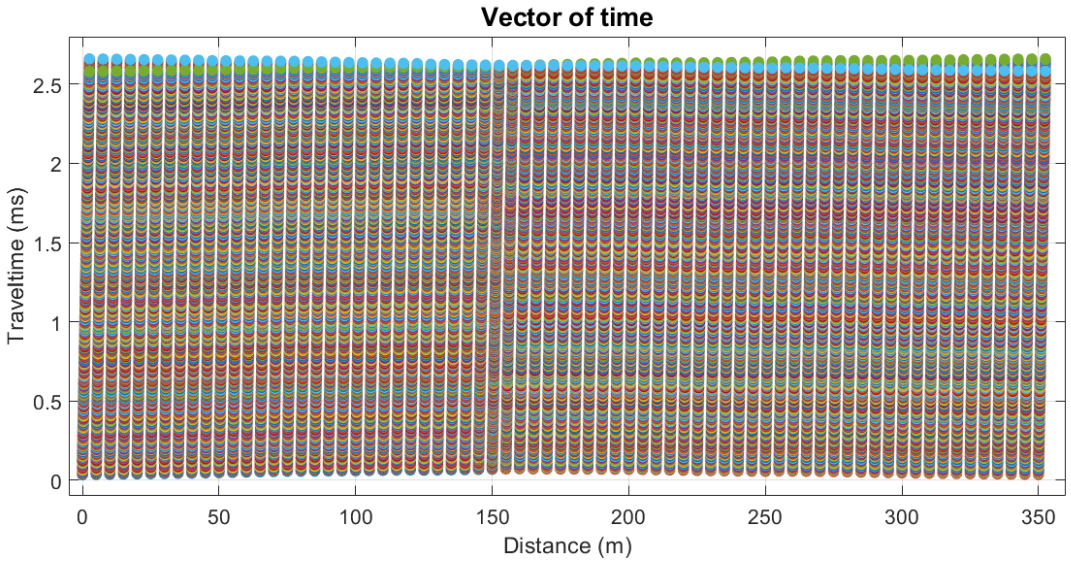

Figure 47: 500 arrival times curves for the simulated data with ζ_1

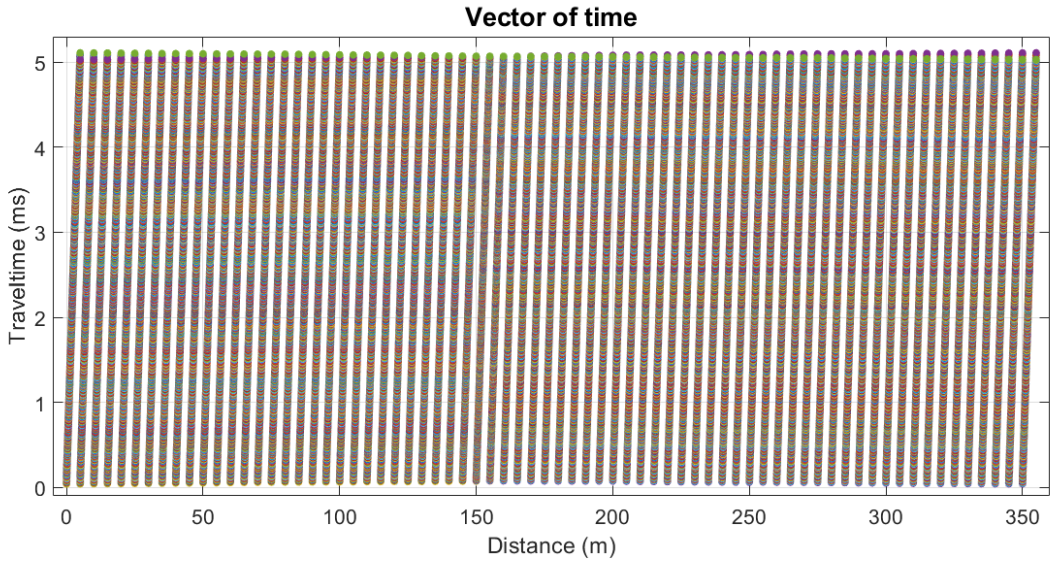

Figure 48: 1000 arrival times curves for the simulated data with ζ_1

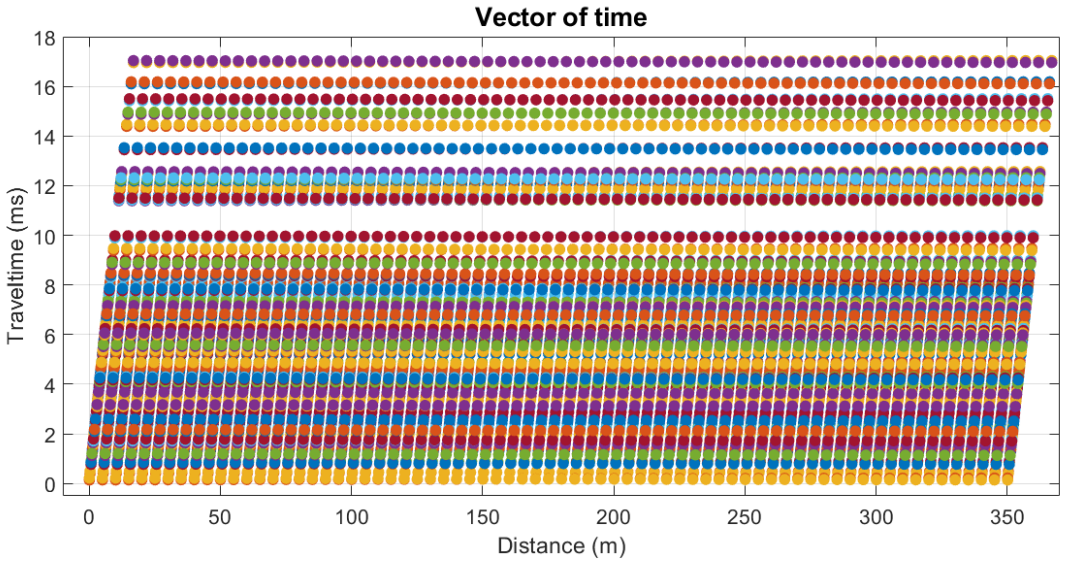

Figure 49: 100 arrival times curves for the simulated data with ζ_2

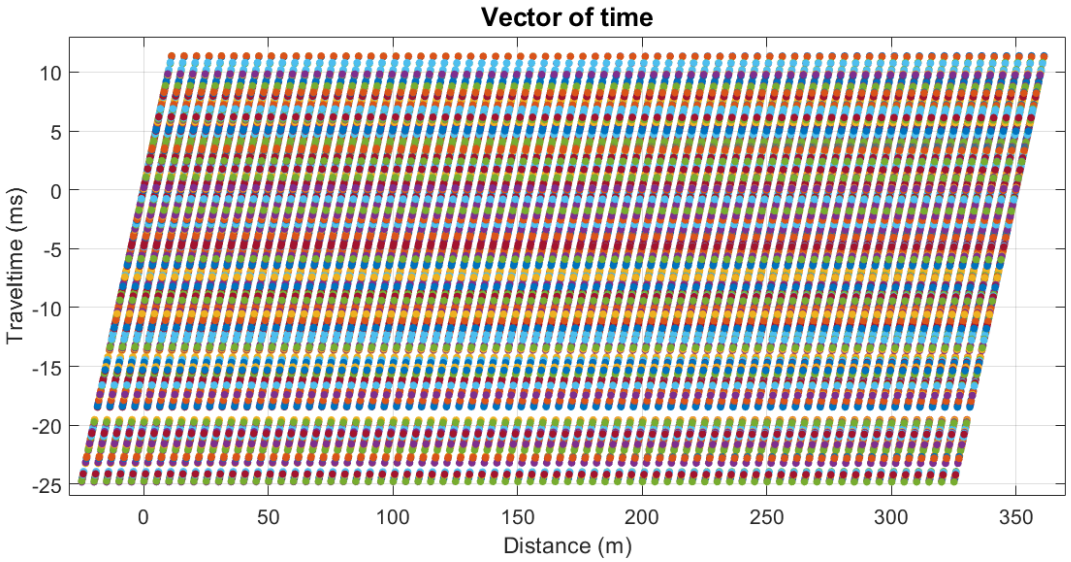

Figure 50: 500 arrival times curves for the simulated data with ζ_2

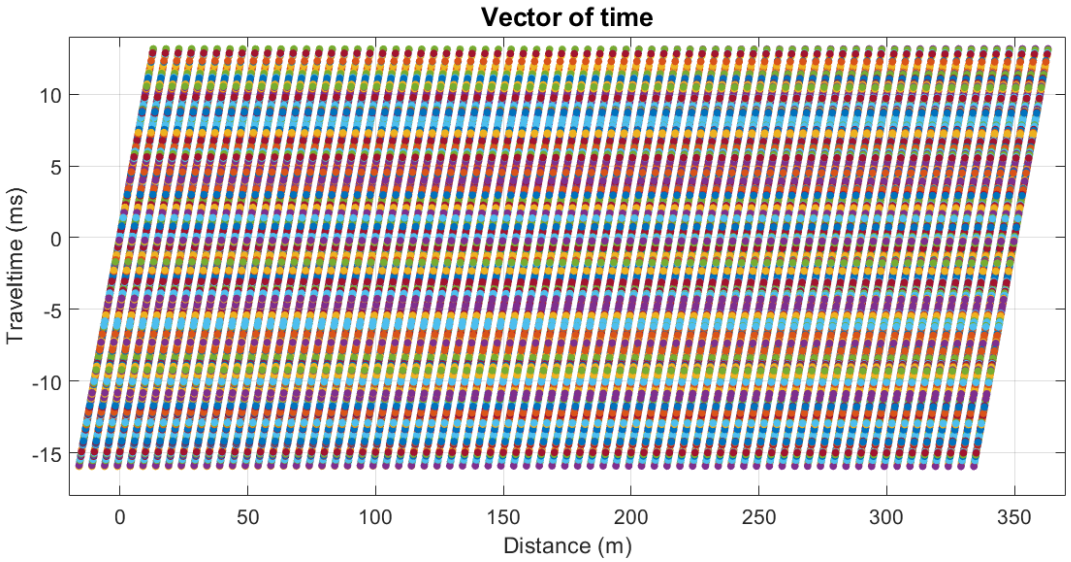

Figure 51: 1000 arrival times curves for the simulated data with ζ_2

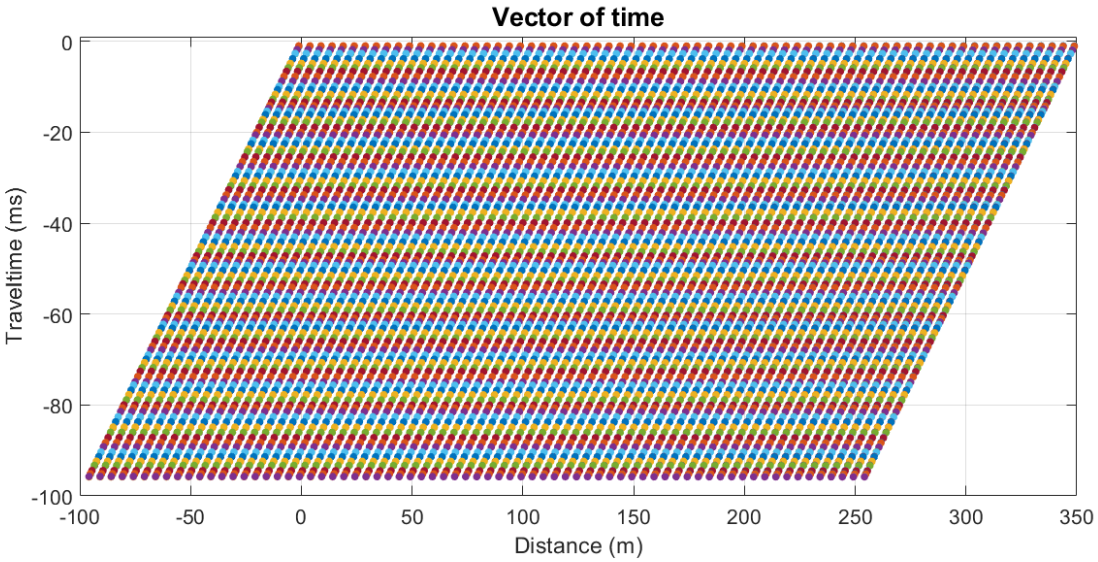

Figure 52: 100 arrival times curves for simulated data with red noise

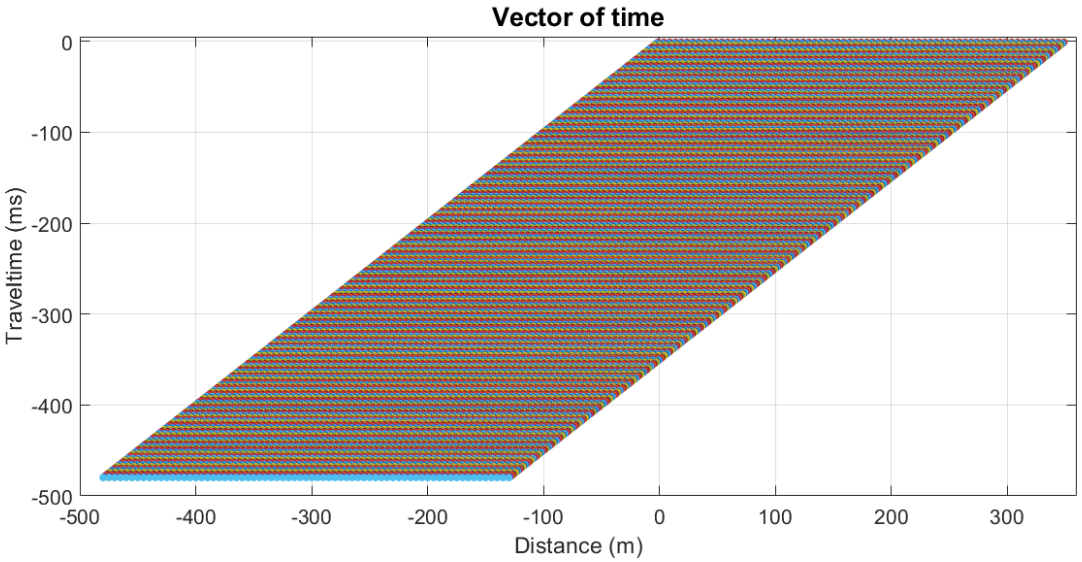

Figure 53: 500 arrival times curves for simulated data with red noise

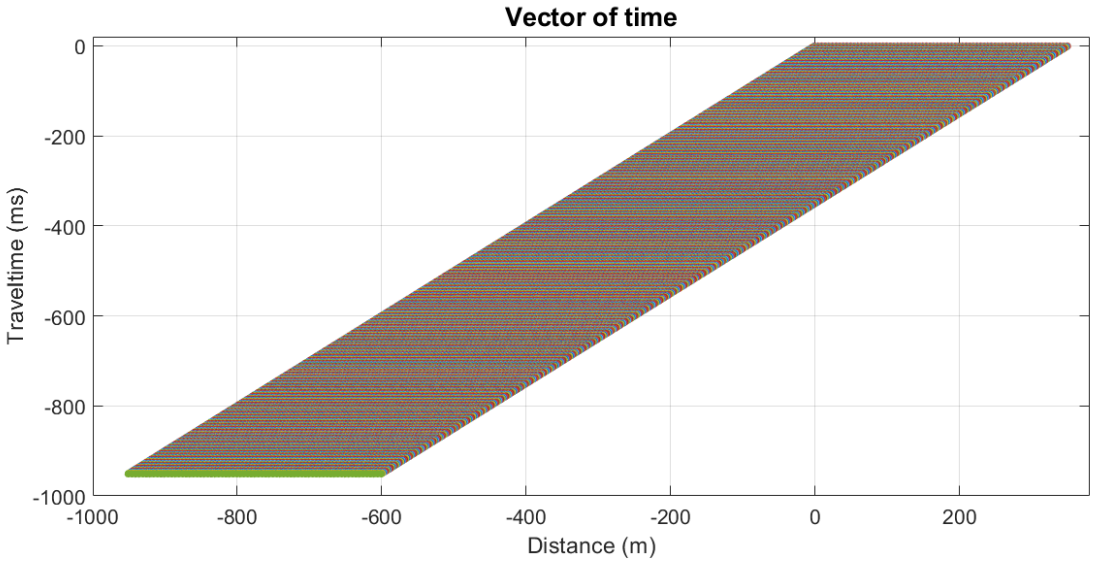

Figure 54: 1000 arrival times curves for simulated data with red noise

Obtaining for each curve generated previously the optimal XY, there are 100, 500 and 1000 optimal curves, to which the median curve is found to find the robust XY optimal (figures 55, 56 and 57).

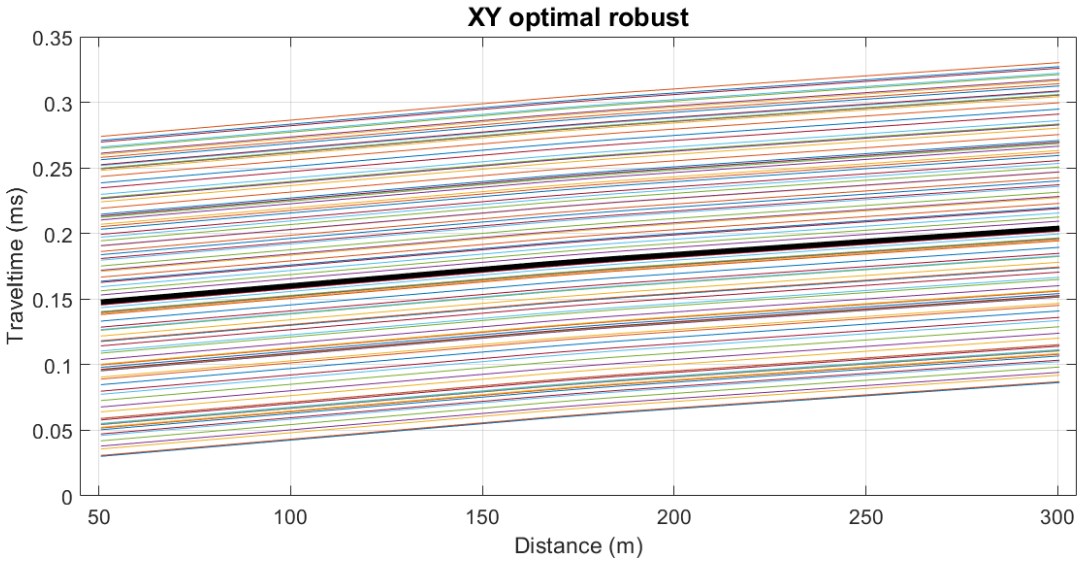

Figure 55: Median of 100 optimal XY curves

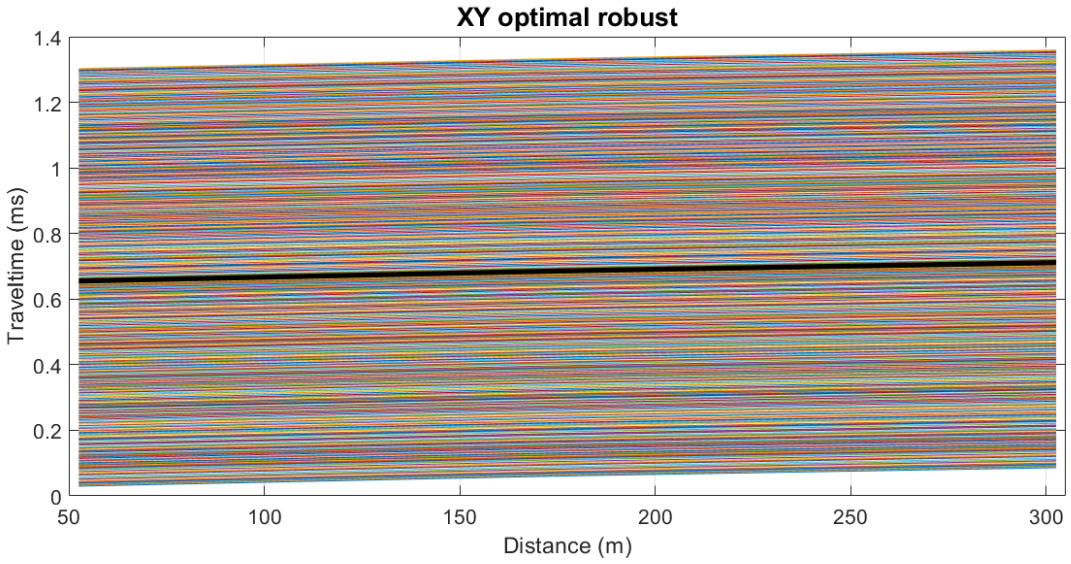

Figure 56: Median of 500 optimal XY curves

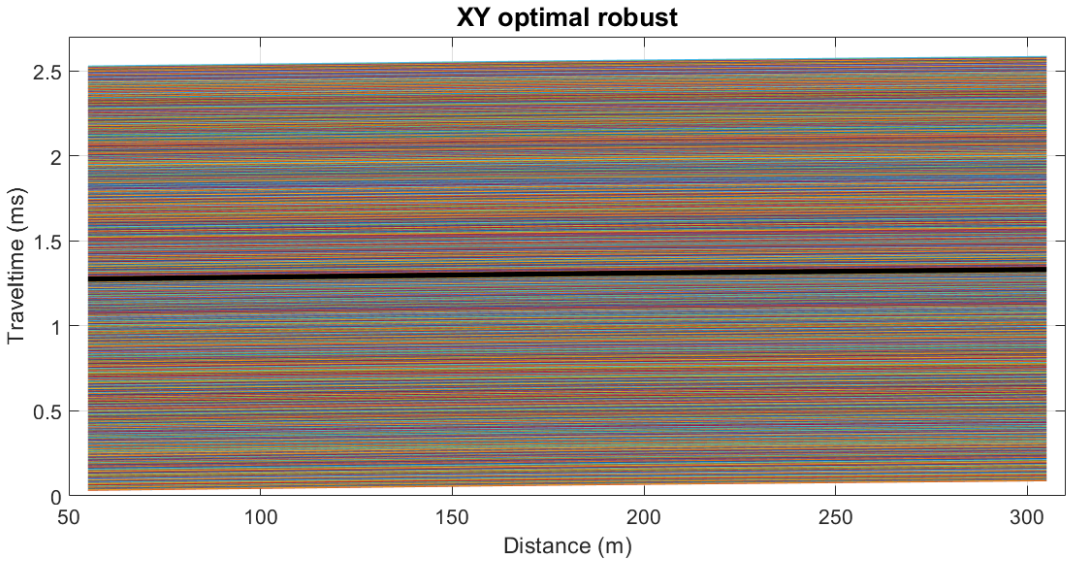

Figure 57: Median of 1000 optimal XY curves

With the above procedure, it is found that 10 meters are the XY optimal robust to generate a mean velocity of 4444.444444 m/s and depth as shown in the figure 58. These data were obtained with the equations 1 and 9 respectively.

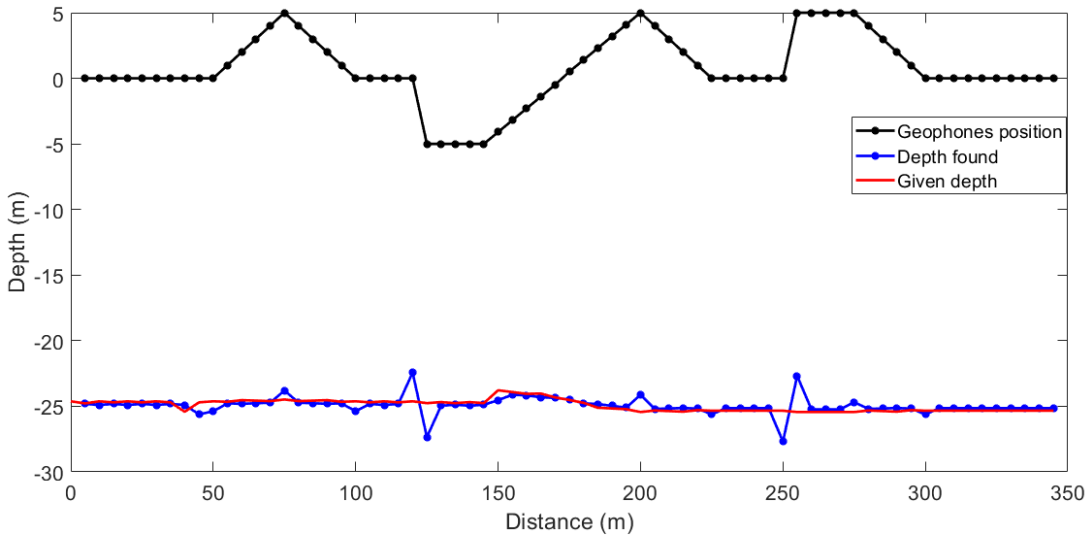

Figure 58: Depth found for the simulated data compared to the given depth.

Base 3. This base has data on an irregular surface and a more irregular refractor than the one presented in base 2, there is a distance of 350 meters in surface and the geophones are placed every 5 meters for a total of 70-time records by Distance-Time curves (Figure 59).

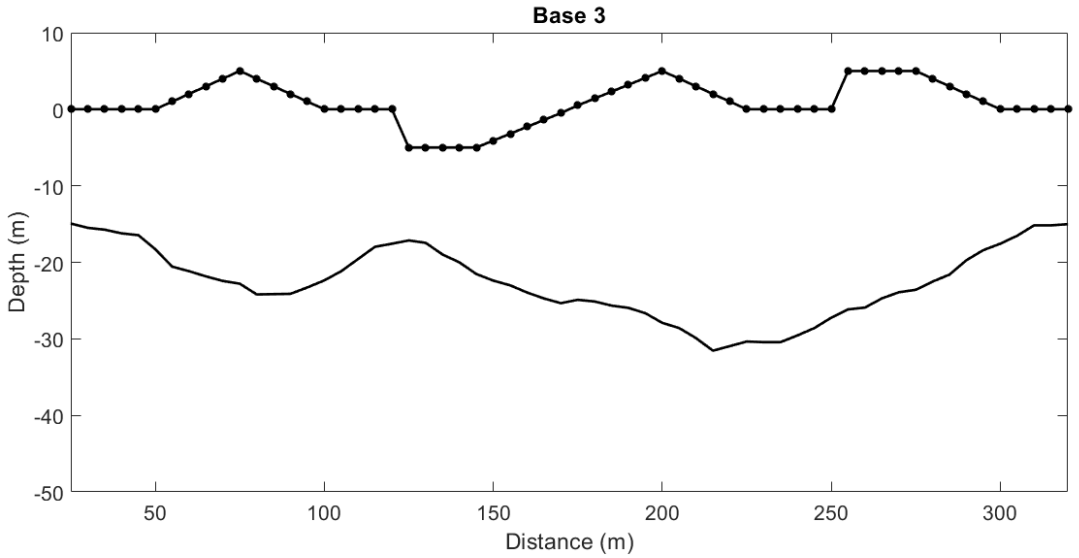

Figure 59: Simulated data with irregular surface and irregular refractor.

As in previous experiments, noise ζ_1, ζ_2 and red noise are applied to arrival times represented in the figures 60, 61, 62, 63, 64, 65, 66, 67 and 68 for 100, 500 and 1000 curves with each type of noise respectively.

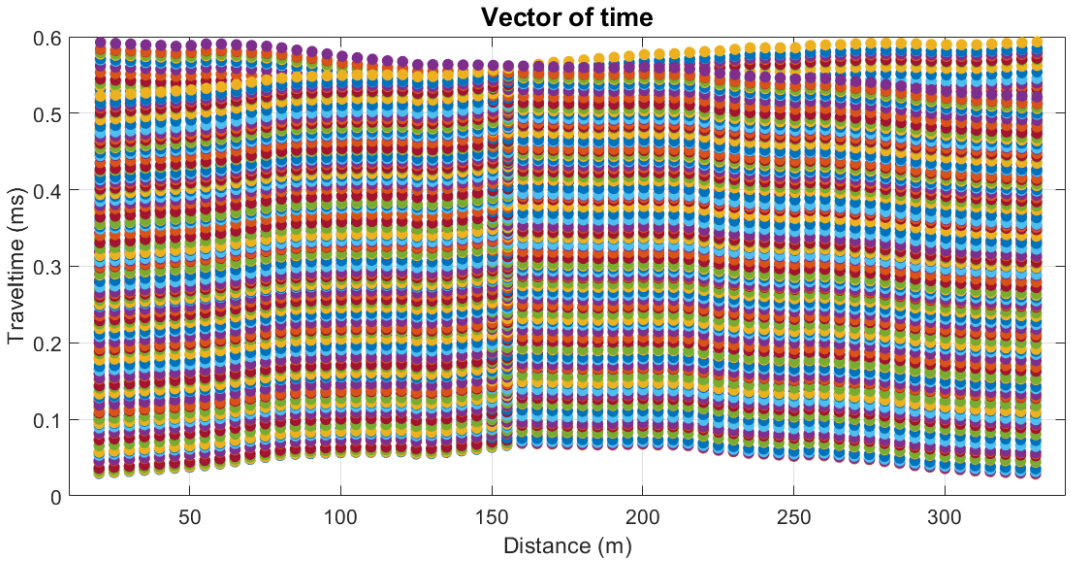

Figure 60: 100 arrival times curves for the simulated data with ζ_1

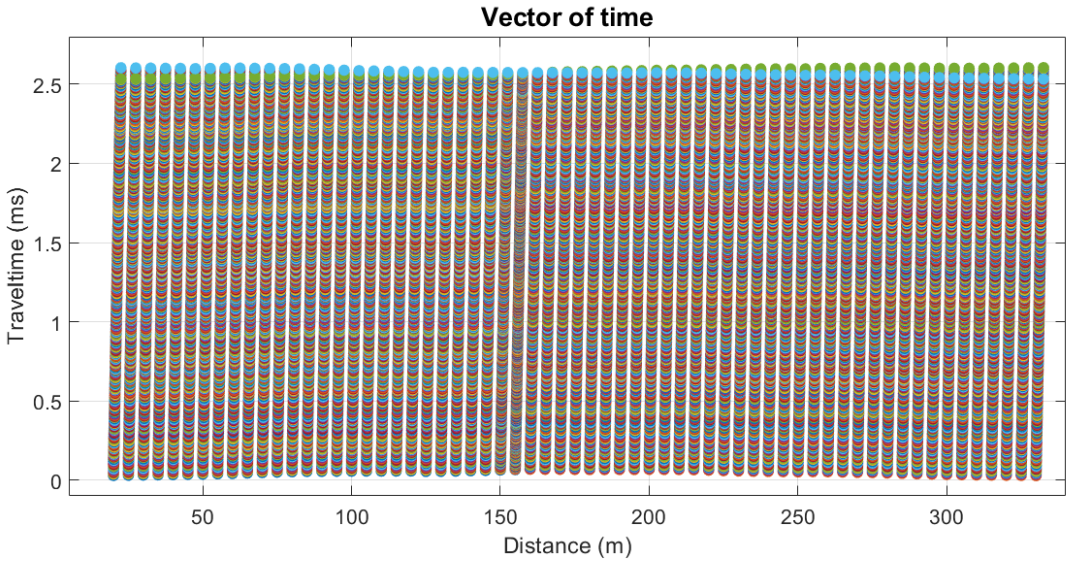

Figure 61: 500 arrival times curves for the simulated data withn ζ_1

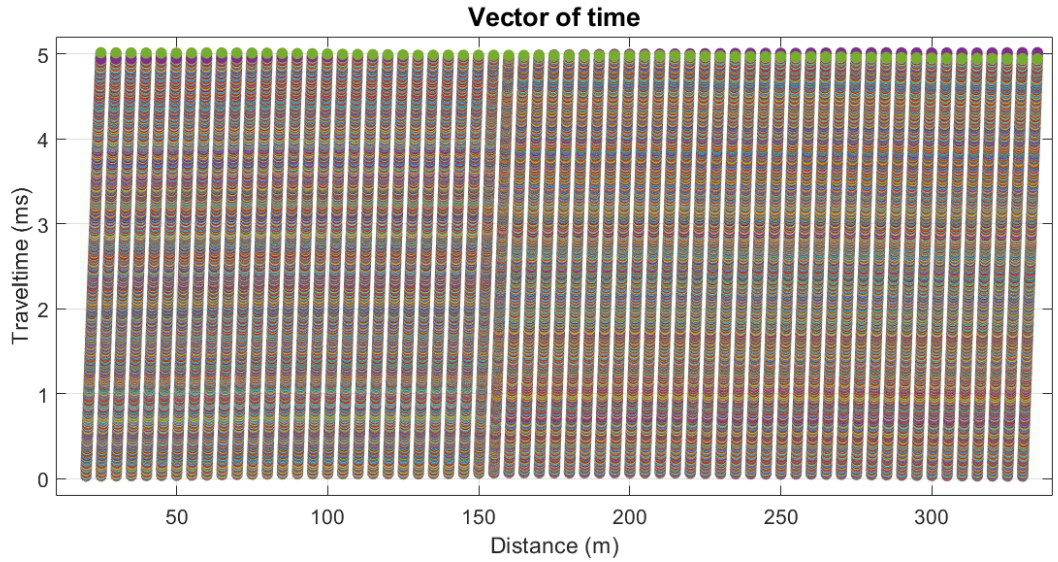

Figure 62: 1000 arrival times curves for the simulated data with ζ_1

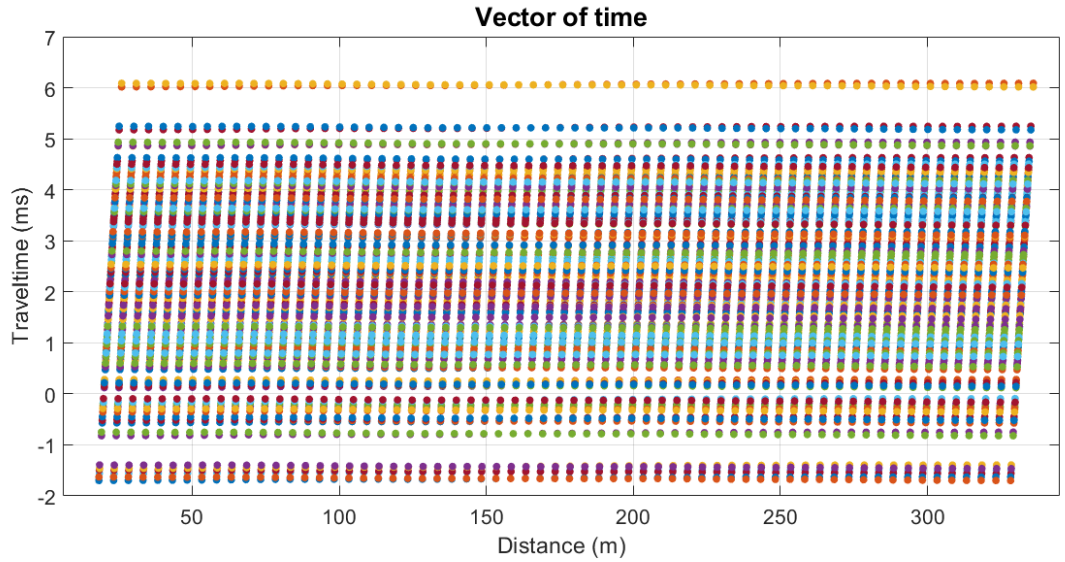

Figure 63: 100 arrival times curves for the simulated data with ζ_2

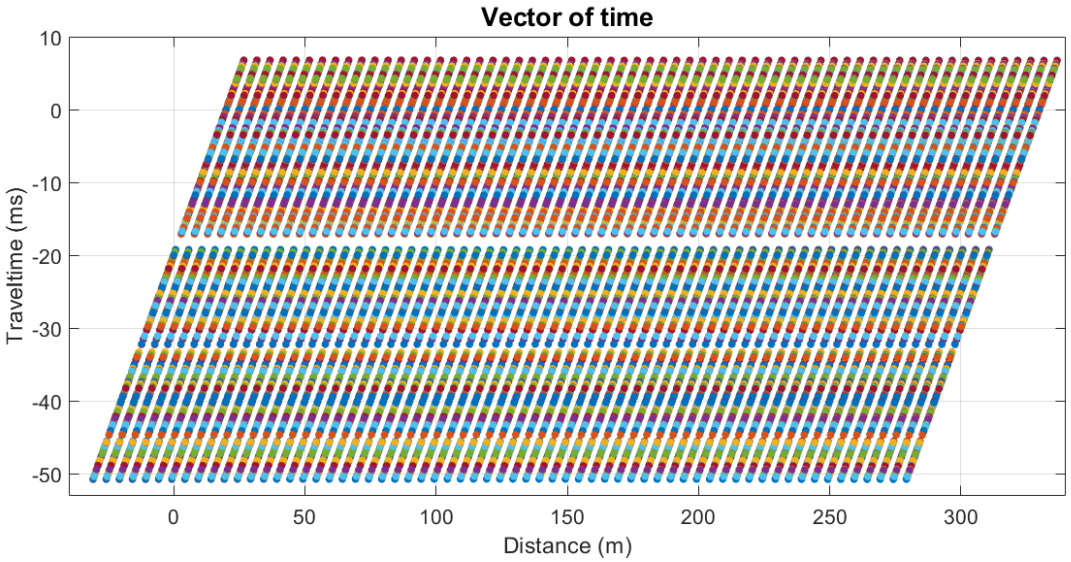

Figure 64: 500 arrival times curves for the simulated data with ζ_2

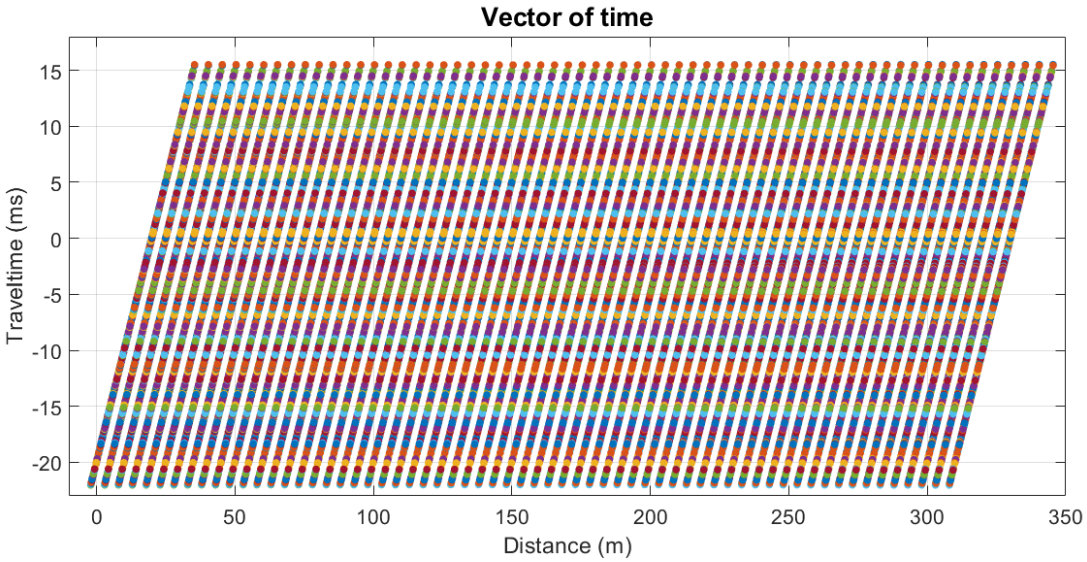

Figure 65: 1000 arrival times curves for the simulated data with ζ_2

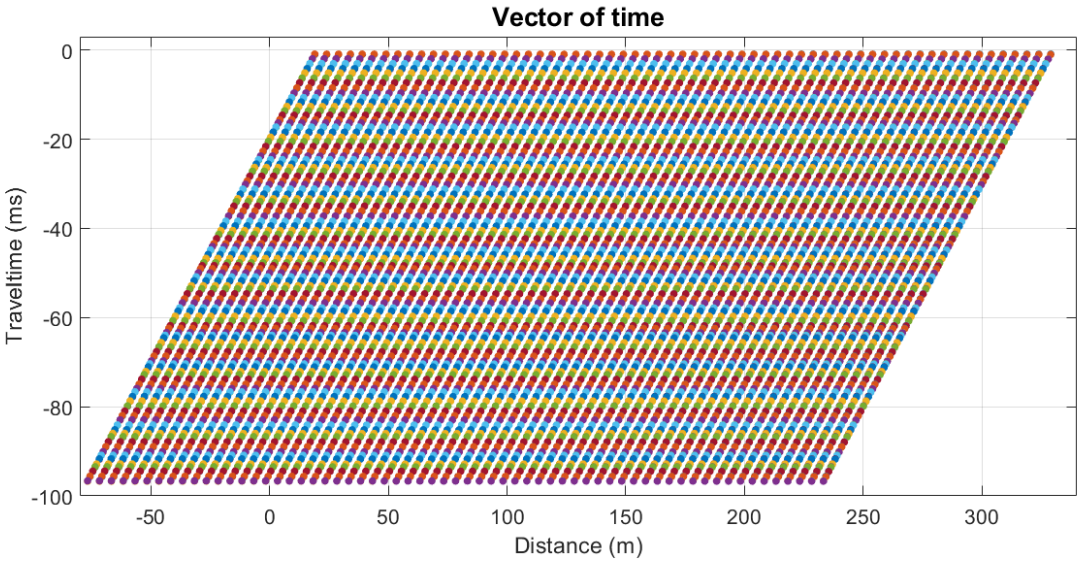

Figure 66: 100 arrival times curves for simulated data with red noise

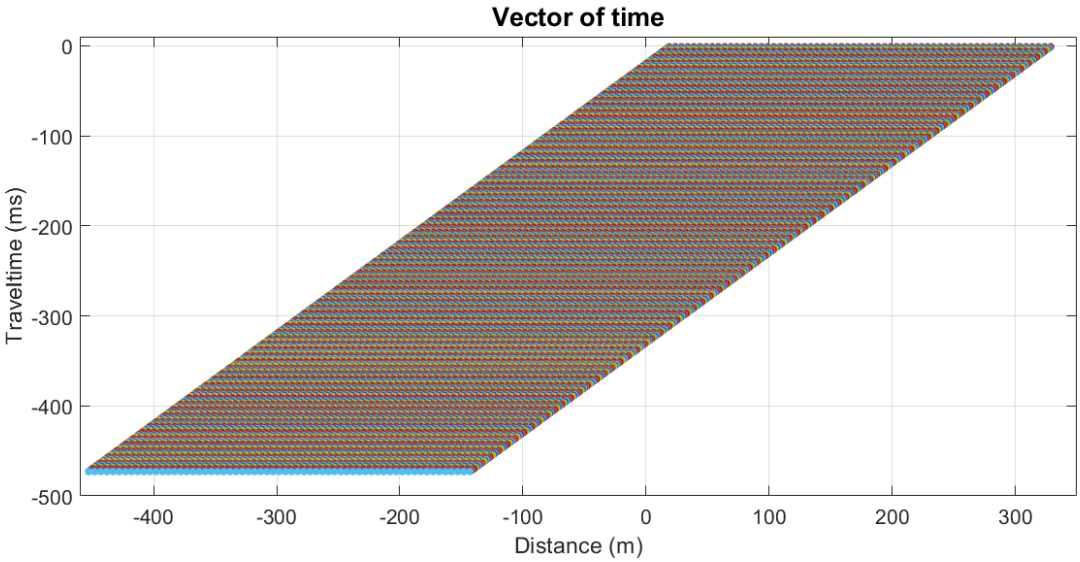

Figure 67: 500 arrival times curves for simulated data with red noise

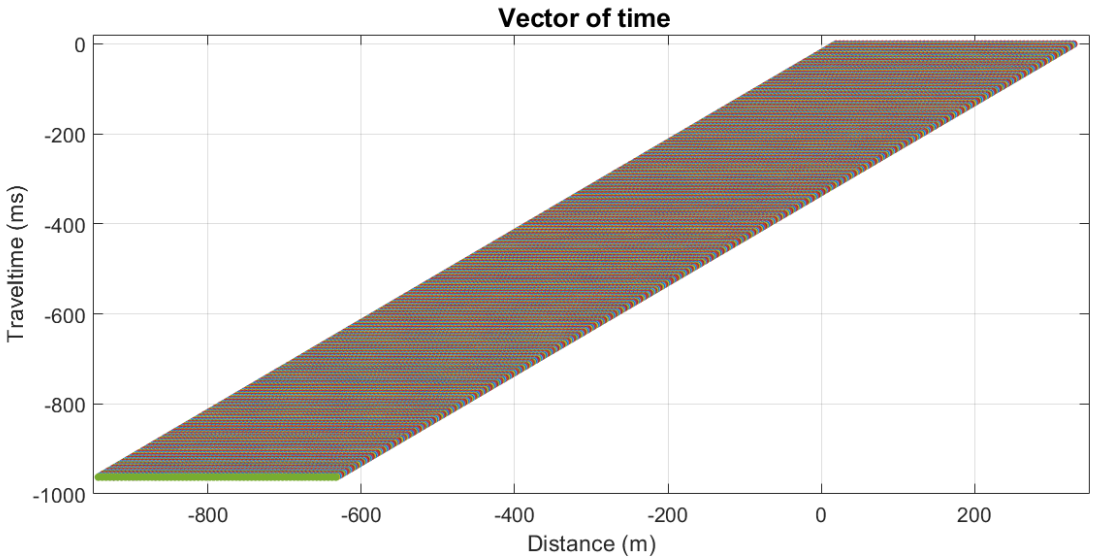

Figure 68: 1000 arrival times curves for simulated data with red noise

From the previous Distance-Time curves the process is done to find the optimal XY obtaining 100, 500 and 1000 optimal XY curves and with them find the median to determine the robust XY optimal (figures 69, 70 and 71).

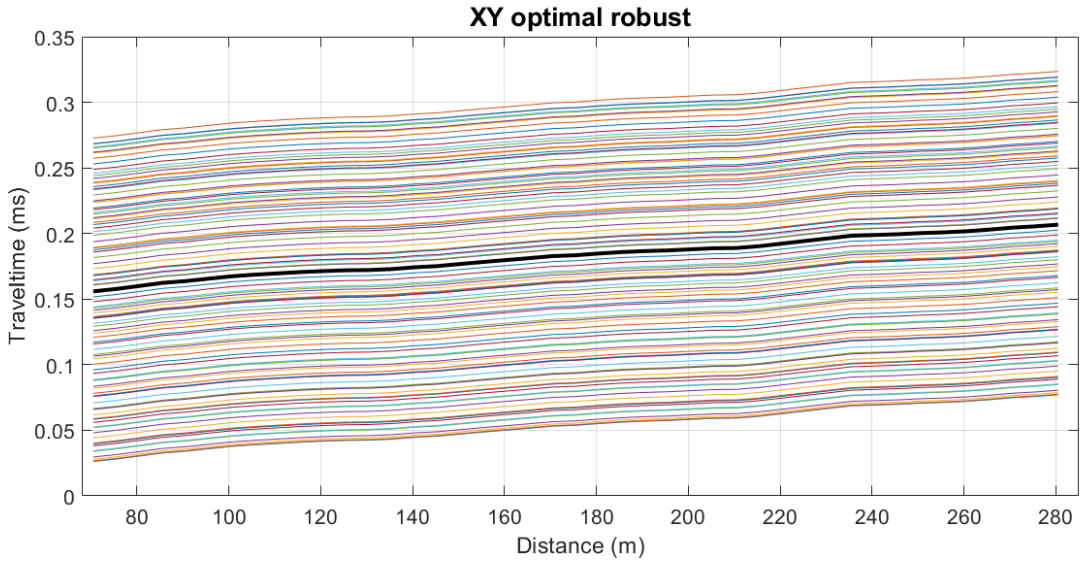

Figure 69: Median de 100 optimal XY curve

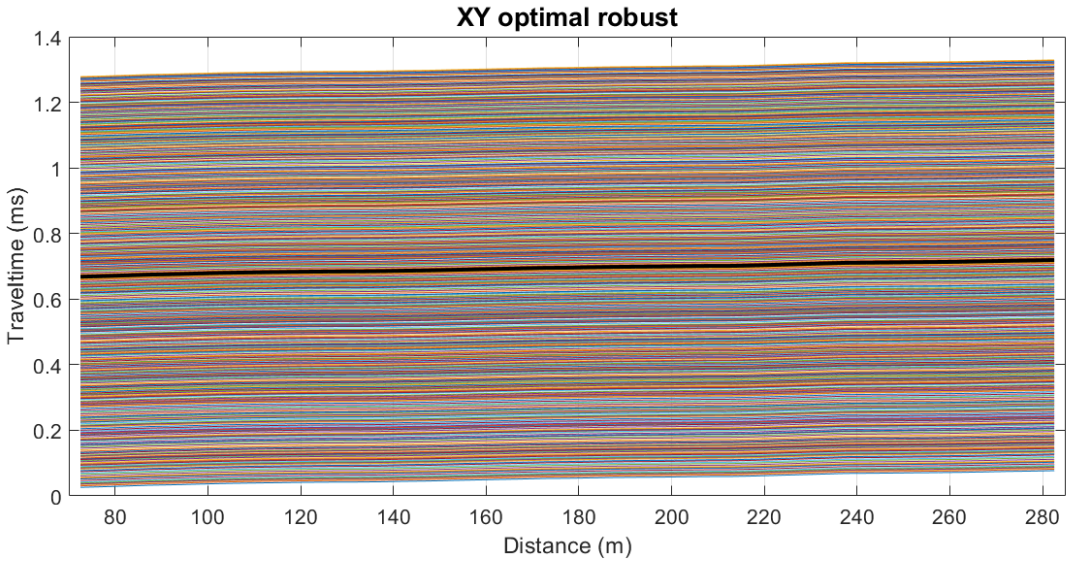

Figure 70: Median de 500 optimal XY curve

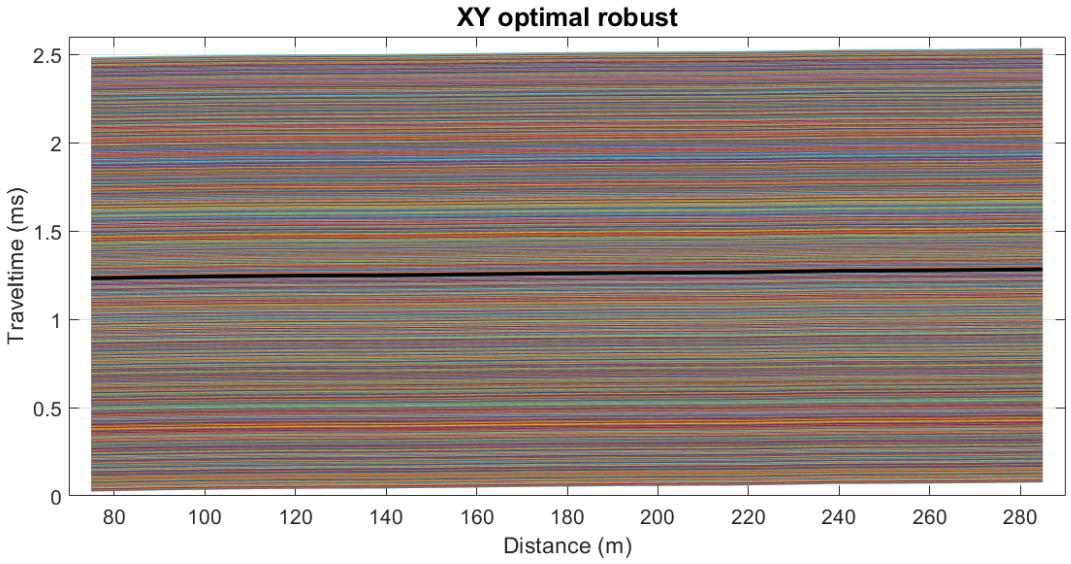

Figure 71: Median de 1000 optimal XY curve

Thus, in all cases we obtain that the sturdy XY is 10 meters with a refractor velocity of 4360.465116 m/s which was calculated with the slope of the equation 1 with the XY robust optimum and then the generalized function of time depth 3 is found to obtain as a result the depth of the refractor through the equation 9. In the figure 72 the depth found compared with the given depth of the simulated data is observed.

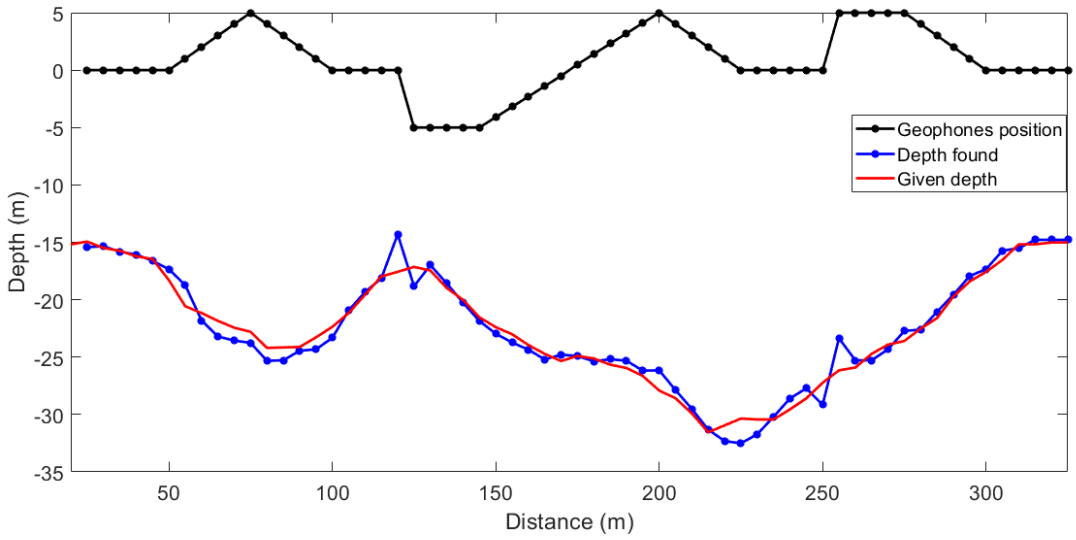

Figure 72: Depth found for the simulated data compared to the given depth.

7.4. Real data

Results are shown with real data provided by the Universidad de Pamplona, Pangea research group. In the work Comparison of refraction, reflection and MASW seismic data, obtained with the SUPER-ONE seismic equipment and the GEODE24 equipment [44], data were taken in a line of 46 meters in the Espiritu Santo urbanization in Pamplona Norte de Santander with the SuperOne equipment (Source: Hammer of 14 Lb, iron plate of 20x20) registering 24 direct and reverse times which were corrected.

In the figure 73 the corrected data record of seismic reflection for two layers is observed, whereby the procedure of the previous examples is done twice, to obtain two speeds and the two depths of the layers.

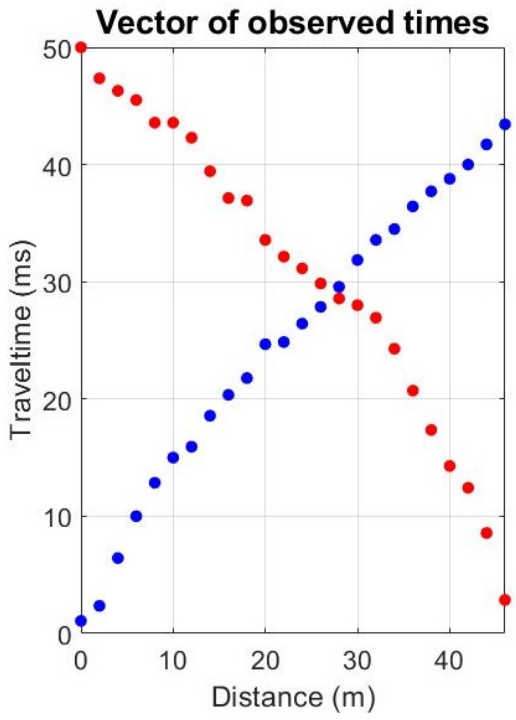

Figure 73: Observed times in Pamplona Norte de Santander

In this case, the arrival times are subject to a normal noise to obtain the graph of the optimal XY for $N = 1000$ in both cases (that is, for layer 1 and layer 2), as shown in the figure 74 for the first layer and in the figure 75 for the second layer.

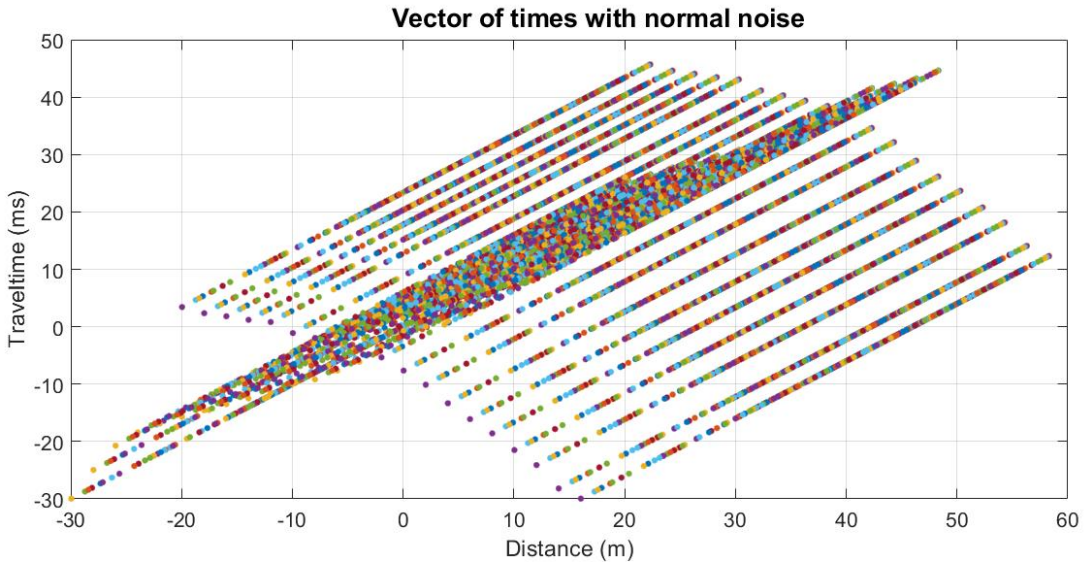

Figure 74: Observed times with normal noise for $N = 1000$ for the first layer

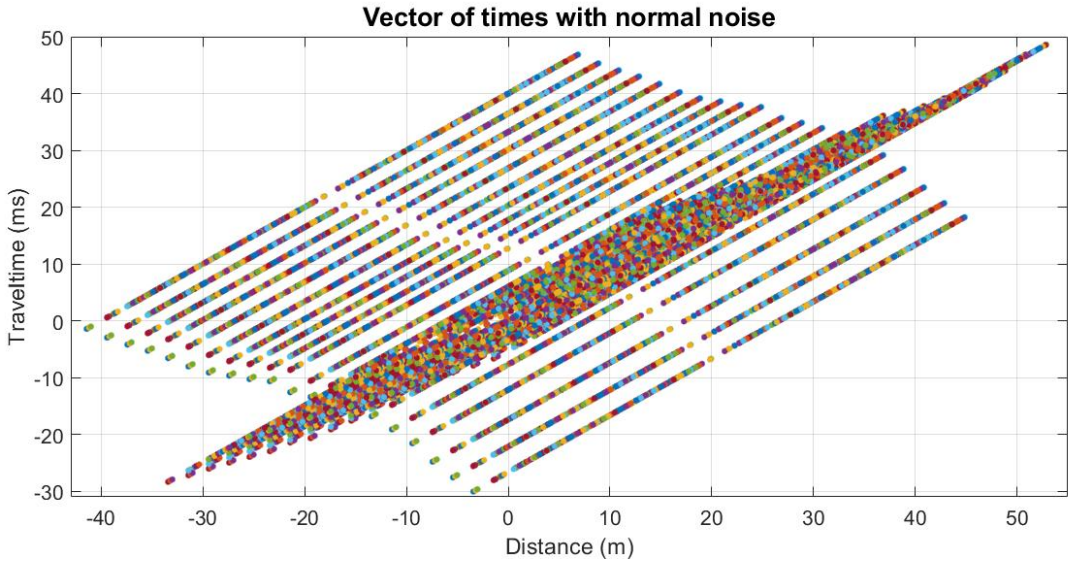

Figure 75: Times observed with normal noise for $N = 1000$ for the second layer

Following the procedure, you will find the velocity functions for each case and its respective linear approximation to choose the optimal XY. As we work with $N = 1000$ we will obtain 1000 XY optimal for which the median curve is found as shown in the figures 76 and 77 using the procedure described in 6.3.1 thus becoming the XY robust optimal for layer 1 and layer 2 respectively.

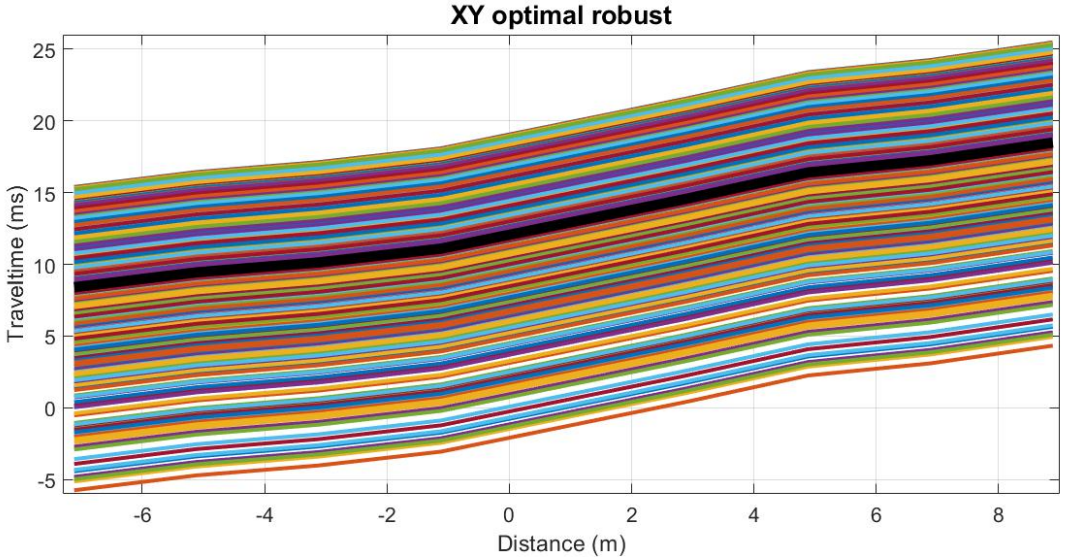

Figure 76: Median curve para 1000 XY optimal in layer 1

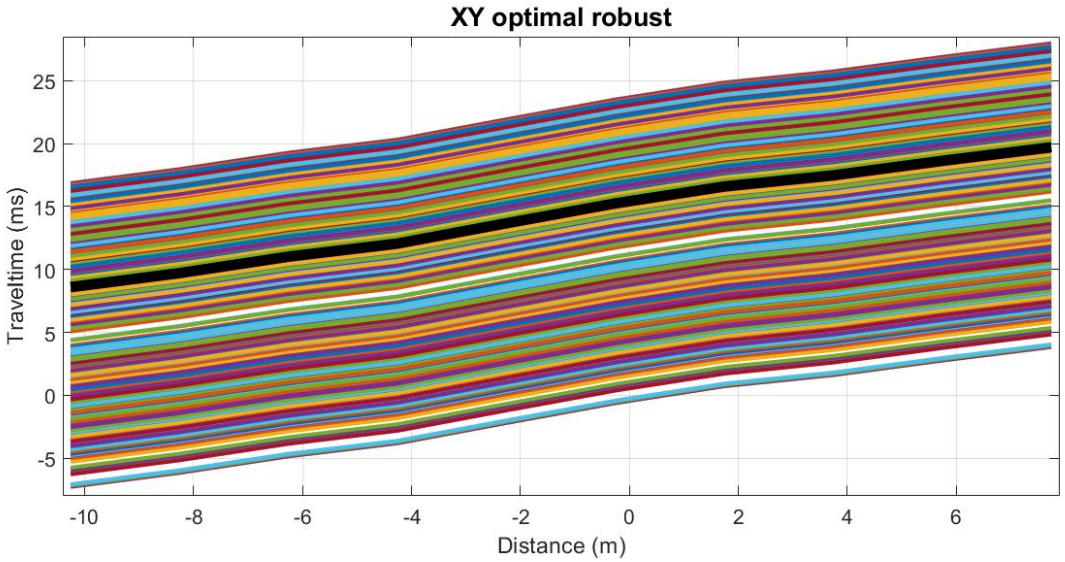

Figure 77: Median curve for 1000 XY optimal in layer 2

Obtaining the XY optimal robust you can find the velocities of the layers. In the first, a robust XY of 20m was obtained and in the case of the second layer an optimum XY 8m.
The velocities calculated were $V_1 = 1198.8m/s$ and $v_2 = 1330.44m/s$ for each layer respectively. Ass the code needs an initial velocity, the value was taken at 0.1m from the surface given in [44], that is, a velocity $V_0 = 508.61m/s$.
With the velocities, the depths of the layers are determined, which can be observed in the figure 78.

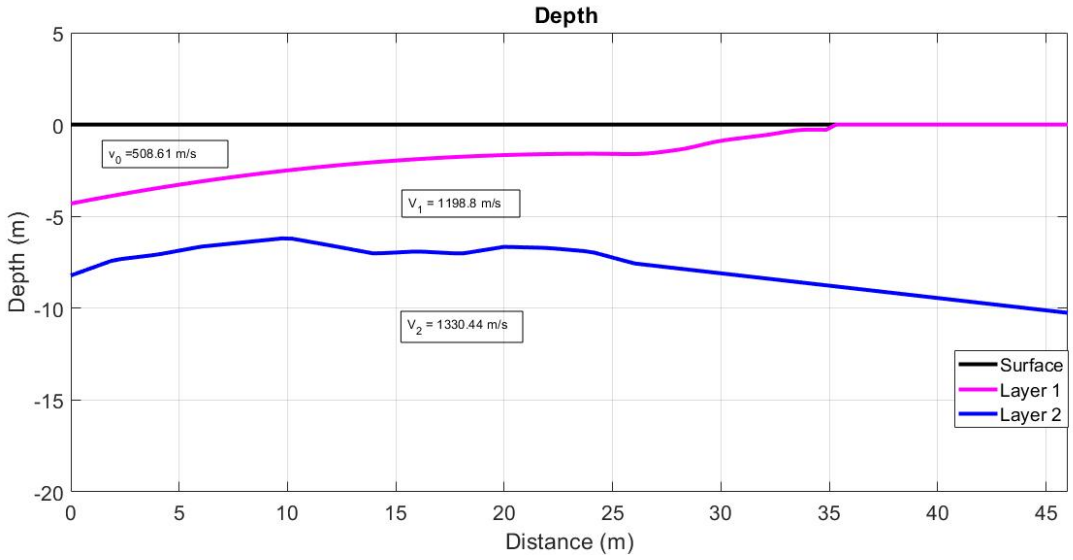

Figure 78: Depth found for layers

This can be compared with the results obtained in the work of Comparison of refraction, reflection and MASW seismic data, obtained with the SUPERONE seismic equipment and the GEODE24 equipment (Table 8. P-wave velocities SuperOne Vs GEODE on page 111) [44].
As shown in the table 2, the first column presents the average of the speeds between 4 meters and 8 meters for the first layer. For the second layer the average of the velocities between 8 meters and 12 meters is considered.
Tn the second column the values obtained with the XY optimal robust are shown and finally the difference between these two velocities are presented.

Velocity SuperOne (m/s)	**Velocity estimated** (m/s)	**Difference** (m/s)	
1215.07	1198.8	16.27	**Layer 1**
1346.238	1330.44	15.798	**Layer 2**

Table 2: Velocities for layers one and two

7.4.1. Pseudocode

This section introduces the pseudocode of the proposed method. It can be seen that the implementation is straigthforward once the concepts of the model and the solution are acquired.
Implementation was made in matlab but the coding in any other language must be easily implemented.

Require: Direct times (tf), inverse times (tr), speed of the first half $(v0)$, position of geophones (x), distance between the geophones (dx), surface (y) and number of curves to obtain N.

for k =1:N **do**

N Distance-Time curves are found with the sum of a random number evenly distributed in the range $(0, 1)$ to the position of the geophones and the times of arrival;

The analysis speed function is found for all possible XY in each Distance-Time curve found.

end for

%————————— XY optimal for each curve————————

Find the coefficients for a polynomial $p(x)$ of degree 1 that is the best fit (in a least squares sense) for the data in (xi, yi) where xi is the values that are taken into account for each XY and yi are the values obtained for speed analysis function (equation 1).

Each xi is evaluated in the polynomial $p(x)$ found.

We find the value of the least square error for each polynomial found with respect to the data yi obtained for each analysis velocity function and then look for the smallest error that would be the optimal XY for each curve.

%————————————Median Functional ————————————————

The functional median is sought for the set of optimal curves obtained where this functional median is introduced by Freiman and Muniz.

Then the data set is the one corresponding to the median which would have the value of the XY optimal robust.

The apparent refractor speed is found as $1/Slope$ of the curve obtained with the XY optimal robust.

%————————————Depth of the refractor ————————————

Having the optimal XY is the time-depth function (equation 3).

And finally you find the depth with the equation9.

Exit:

Distance-Time graph.

XY optimal robust.

Apparent velocity of the refractor.

Depth

8. Conclusions

This thesis had the outcome to reach a mathematics based solution for engineering problems, not solved by technology. The resulting algorithm is easy and understandable once the physics underlying the phenomenon are well understood and the stochastic nature of the problem formulated properly, reaching a simple solution based on stochastic models and functional data analysis. Based on the initial proposal for Colciencias and the curriculum chosen by advisors in the Master in Applied Mathematics programme, the hypothesis was tested and a sucessful application carried out. The robust solution for parameter estimation in the generalized reciprocal method for seismic refraction offers a non expensive solution for direct implementation in norte de Santander. Several distributions were used to model uncertainty on the variations of the subsoil, the changes of speed, the different variations of density and speed of the middle of the layers, the uncertainty of the measurement and the noises in the geophones the spatial location of the geophones. Adding the modeled uncertainties and disturbances, the deterministic model enhanced its accuracy. Results are accurate and the refining of the algorithm must be done in future works considering more formally the non gaussianity of the problem. Resulting velocities of on layer, two layers, complex subsurface are very close to real ones and this method can be inmediately tested in more regions of the country. Intellectual property on the algoritm will be protected.

Acknowledgements

The author acknowledges Scientific Computing Apolo at Universidad EAFIT (http://www.eafit.edu.co/apolo) to conduct the research reported in this scientific product. Special thanks to Universidad de Pamplona, Pangea research group. The scientific spirit for sharing real data obtained with the SUPERONE seismic equipment and the GEODE24 equipment [44]. Advisors acknowledge the faculty of Mathematical Sciences department for their teaching quality, needed for the development of concepts and formal ideas.

References

[1] Colciencias, Convocatoria Norte de Santander (2016).

[2] Agencia Nacional de Míneria, www.anm.gov.co (2017).

[3] Ministerio de Minas y Energía, www.minminas.gov.co/las-cifras-del-sector-minero, 26 de Julio de 2017 (2016).

[4] A. Urea, Realidades de la legalización artesanal en colombia, V CONGRESO CUBANO DE MINERIA (MINERIA 2013) Minería.

[5] E. Guevara, Logistics Analysis of Coal in North of Santander (c).

[6] M. Araneda, Servicios Geofísicos en Minería e Ingeniería SEGMI. Obtenido de Servicios Geofísicos en Minería e Ingeniería SEGMI (2017).

[7] F. Gonzales, Estimación de velocidades de onda corte: Registro de Ondas Superficilaes Love V/S Refracciones de Ondas Internas, Ph.D. thesis, Universidad de Chile (2015).

[8] F. A. H. Guarachi, Aplicación De Métodos Geofísicos Basados En Ondas Superficiales Para La Caracterización Sísmica De Suelos. Aplicación a La Microzonificación Sísmica Del Norte Y Poniente De Santiago, Pontificia Universidad Catolica De Chile.

[9] E. Franco, Método de refracción sísmica (2016) 1–5.

[10] Instituto de Investigaciones Mineras (IIM), http://www.fi.unsj.edu.ar/descargas/ingreso/explora minera.pdf, universidad nacional de san juan (2010).

[11] K. Rezaei, V. Amiri, A. Beitollahi, The contribution of electrical resistivity and seismic refraction techniques to Site characterization and earthquake risk assessment, a case study: IKIA airport, Iran, Elixir 62 (2013) 17669–17676.

[12] A. Hormazabal, Hugo y Pinto, Informe N 1 " Prospección Sísmica " (2011) 1–12.
URL https://apmine.files.wordpress.com/2011/11/informe-prospeccic3b3n-sc3adsmica.pdf

[13] B. Zana, P. Sanchez, F. Bravo, L. Sullca, S. Caballero, Introducción a la ingenieria geologica y de minas (2010).
URL https://www.e-quipu.pe/dinamic/publicacion/adjunto/14753589909Iug1mu3WA.pdf

[14] N. Gella, J. Bruggen, La exploracion geofisica del subsuelo, Sociedad Nacional de Minería 32.

[15] M. A. Gayá Florez, Procesado de Sísmica de Reflexión Superficial en el Complejo Turbidítico de Ainsa (Huesca) (2004).
URL http://upcommons.upc.edu/handle/2099.1/3404

[16] R. Griffiths, D.H. y King, Applied Geophysics for Geologists and Engineers, 2nd Edition, 1981. doi:10.1016/B978-0-08-022072-7.50012-7.
URL http://www.sciencedirect.com/science/article/pii/B9780080220727500127

[17] A. F. y. J. C. H. Burger, H. Rober y Sheehan, Explorring the Shallow Subsurface, 2006.

[18] J. Cantos, Tratado de geofísica aplicada, 1974.

[19] E. Ministerio de medio Ambiente, Técnicas geofísicas (2016).
URL http://www.cedex.es/NR/rdonlyres/C63444EB-3A5F-4346-9CE0-AF209AB125F1/132409/ENSAYOSGEOFISICOS.pdf

[20] N. Vitulli, Geofísica (2017).
URL http://www.unsa.edu.ar/geofisica-salta/Teorias/Unit1.pdf

[21] M. R. Gadallah, R. Fisher, A Comprehensive Guide to Seismic Theory and Application, 2005.

[22] C. Jr, Integração da tomografia sísmica de refração e da análise multicanal de ondas superficiais na investigação rasa na região de Termas de Ibirá, estado de São Paulo, Brasil.

[23] M. L. Rucker, Applying the Seismic Refraction Technique To Exploration for Transportation Facilities.

[24] I. B. Osazuwa, A. D. Chinedu, Seismic refraction tomography imaging of high-permeability zones beneath an earthen dam, in Zaria area, Nigeria, Journal of Applied Geophysics 66 (1-2) (2008) 44–58. doi:10.1016/j.jappgeo.2008.08.006.
URL http://dx.doi.org/10.1016/j.jappgeo.2008.08.006

[25] F. M. Campbell, A. Kaiser, H. Horstmeyer, A. G. Green, F. Ghisetti, A. R. Gorman, M. Finnemore, D. C. Nobes, Processing and preliminary interpretation of noisy high-resolution seismic reflection/refraction data across the active Ostler Fault zone, South Island, New Zealand, Journal of Applied Geophysics 70 (4) (2010) 332–342. doi:10.1016/j.jappgeo.2009.05.001.
URL http://dx.doi.org/10.1016/j.jappgeo.2009.05.001

[26] T. Engelsfeld, F. Šumanovac, V. Krstić, Classification of near-surface anomalies in the seismic refraction method according to the shape of the time-distance graph: A theoretical approach, Journal of Applied Geophysics 74 (1) (2011) 59–68. doi:10.1016/j.jappgeo.2011.03.004.

[27] Jarkko Okkonen and Kari Moisio, Seismic reflection surveys in glaciofluvial deposits in Finland, Near Surface Geophysics. EAGE (2015) 417–432.

[28] O. Preto, Desenvolvimento de interface gráfica para a otimização das rotinas de processamento de dados sísmicos de alta resolução (Sparker, Boomer e Chirp) no programa SU (Seismic UNIX) (2012).

[29] D. S. D. Queiroz, M. V. A. G. D. Lima, Aplicação dos Métodos Sísmicos MASW e Tomografia de Refração para a Determinação das Propriedades Mecânicas do Solo: um estudo de caso no município de Caçapava do Sul/RS (2016) 1–5.

[30] L. Jorge, G. Salamanca, M. C. Leal, J. F. Morales, R. E. N. Montes, Minería en Colombia, Mineria en Colombia Fundamentos para superar el modelo extractivista (2013) 209.
URL http://www.foronacionalambiental.org.co/wp-content/uploads/2011/11/libro-1.pdf{#}page=89

[31] Ministerio de Minas y Energía, Política minera de Colombia. Bases para la minería del futuro, Minminas (2016) 1– 62.
URL https://www.minminas.gov.co/documents/10180/698204/Pol{í}tica+Minera+de+Colombia+final.pdf/c7b3fcad-76da-41ca-8b11-2b82c0671320

[32] N. Cooper, Y. Herrera, MANUAL PARA LA ADQUISICIÓN Y PROCESAMIENTO DE SÍSMICA TERRESTRE Y SU APLICACIÓN EN COLOMBIA, UNIVERISDAD NACIONAL DE COLOMBIA, Bogotá, 2010.

[33] C. Rosales, Sobre El Comportamiento Sísmico De Los Depósitos De Suelos Del Área De Cañaveralejo, Cali, Colombia, Journal of Chemical Information and Modeling 53 (2013) 1689–1699. arXiv:arXiv:1011.1669v3, doi:10.1017/CBO9781107415324.004.

[34] J. Pulido, M. Rodríquez, CARACTERIZACIÓN DEL SUBSUELO UTILIZANDO EL MÉTODO GEOFÍSICO DE REFRACCIÓN POR MICROTREMORES ReMi PARA SEGMENTO DE LA AVENIDA CIRCUNVALAR Y PARQUE CENTRAL SIMÓN BOLIVAR, Ph.D. thesis, UNIVERSIDAD DISTRITAL FRANCISCO JOSÉ DE CALDAS (2015).

[35] H. R. Mancilla Vesga, CARACTERIZACIÓN GEOFÍSICA DE LAS ZONAS CLAUSURADAS Y EN OPERACIÓN, EN LAS INSTALACIONES DEL RELLENO SANITARIO REGIONAL "LA CORTADA", Ph.D. thesis, Universidad de Pamplona (2017).

[36] J. R. Sheehan, W. E. Doll, W. a. Mandell, An Evaluation of Methods and Available Software for Seismic Refraction Tomography Analysis, Jeeg 10 (3) (2005) 21–34. doi:10.2113/JEEG10.1.21.

[37] A. G. Chilusa, S. Naranjo, Exploración de subsuelo (2014) 4–6.

[38] DANE, Informe de coyuntura economica regional (2016).

[39] M. J. G. Cox, E. F. Scherrer, R. Chen, Static Corrections for Seismic Reflection Surveys (1999) 531arXiv:arXiv:1011.1669v3, doi:doi:10.1190/1.9781560801818.
URL https://books.google.co.uk/books/about/Static{_}Corrections{_}for{_}Seismic{_}Re
html?id=2zycziT1G8kC{&}pgis=1

[40] D. Palmer, The generalised reciprocal method of seismic refraction interpretation, 1980.

[41] D. Palmer, An introduction to the generalized reciprocal method of seismic refraction interpretation 46 (11) (2001) 1508–1518.

[42] R. Fraiman, G. Muniz, Trimmed means for functional data, Test 10 (2) (2001) 419–440. doi:10.1007/BF02595706.

[43] J. O. Ramsay, B. W. Silverman, Functional data analysis, 2005. doi:10.1007/978-0-387-98135-2.

[44] A. F. C. Rojas, Comparación de datos sísmicos de refracción, reflexión y MASW, obtenidos con el equipo de sísmica Superone y el equipo Geode24, Ph.D. thesis, Univerdidad de Pamplona (2018).

[45] S. Marshak, Essentials of Geology, fourth edi Edition, W.W. Norton & Company, New York, London, 2012.

[46] F. K. Lutgens, E. J. Tarbuck, D. Tasa, Essentuals of Geology, 11th Edition, Prentice Hall, 2011.

[47] L. A. Estrada, Apuntes de Prospección Sísmica, Tech. rep., Universidad Nacional de Tucuman, Tucuman (2008).
URL http://catedras.facet.unt.edu.ar/geofisica/wp-content/uploads/sites/4/2014/02/Sismica-para-Geologos.pdf

[48] W. Telford, L. Geldart, R. Sheriff, Applied Geophysics, refracción, 1990.

AppendixA. Theoretical framework: Physical principles of exploration seismic

When a pulse is generated, waves are induced that propagate through the ground, both inside and through its surface. Seismic waves, which consist of small packages of elastic deformation energy, move away from any seismic source at speeds determined by the elastic moduli and densities or the media through which they pass [17].
If analytically they express the equilibrium equations of the body is affected by disturbance of a system of equations which is obtained have deduced four solutions that result in the longitudinal, transverse waves, Rayleigh and Love [18].

AppendixA.1. Types of seismic waves - internal waves

They are the ones which traveled to the crossing of the interior of the earth. They follow curved roads due to the different density and composition inside the Earth. The following types can be distinguished:

a. **Longitudinal waves:** Known as P waves, they consist of the transmission of compressions and refractions of the rock, similar to the propagation of sound (Figure A.79). These waves are also named waves of comprehension and dilation and condensation and rarefaction; they are called primary waves or P waves because they are the first to arrive in earthquakes. These are the waves that are used in the seismic exploration by reflection and refraction[18].

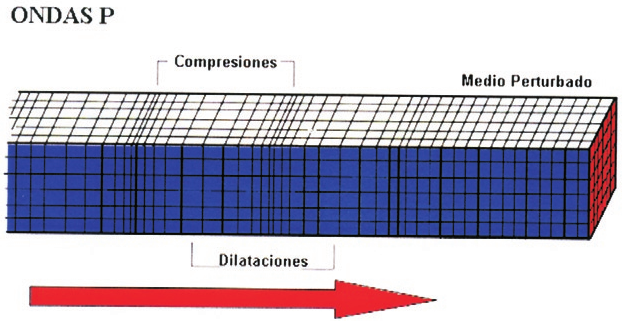

Figure A.79: P wave

b. **Transverse waves:** Known as S waves, they consist of the propagation of shear waves (cut), where the particles move in a direction perpendicular to the direction of propagation of the disturbance (Figure A.80) [45]; lthey are assigned the letter S, since they form the second group of important waves in an earthquake.

   In the case of transverse waves traveling parallel to the surface of the earth, if the particles oscillate from top to bottom, the wave is called SV and, if the particles oscillate in a horizontal plane, they are called SH [18].

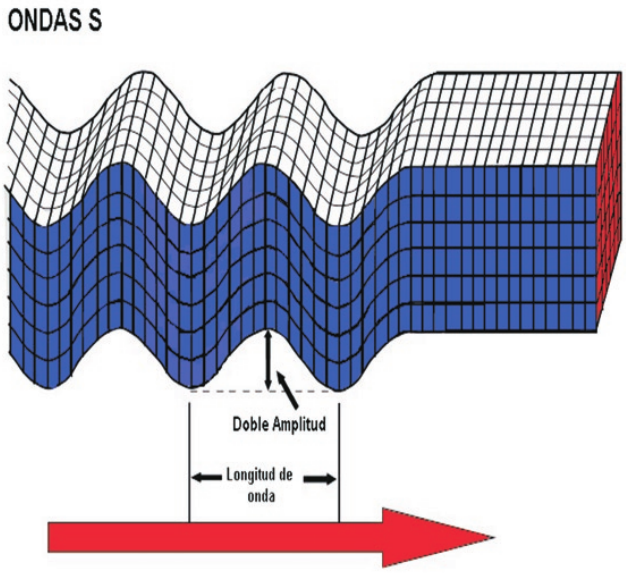

Figure A.80: S wave

AppendixA.2. Classes of seismic waves - surface waves

They receive that name because they only propagate through the most superficial layers of the Earth, decreasing their amplitude with depth. Within this type of waves, two modalities can be differentiated, called Rayleigh waves and Love waves in honor of the scientists who theoretically demonstrated their existence [46].

a. **Rayleigh waves:** they form on the surface of the Earth and cause the particles to move along a retrograde elliptical path (Figure A.81). They are a combination of longitudinal and transverse waves [18].

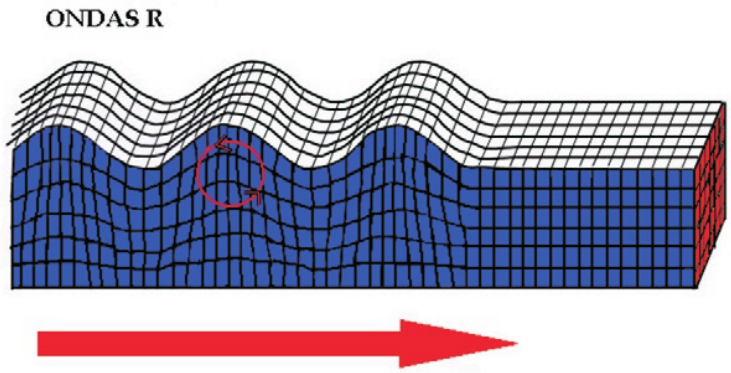

Figure A.81: Rayleigh wave

b. **Love waves:** Originate in the interface of two media with different mechanical properties; in this case, the movement of the particles is perpendicular to the direction of propagation of the disturbance, similar to S waves, but only occurs in the plane of the earth's surface (figure A.82) [46]. They are another combination of longitudinal and transverse waves in which the displacement of the particles is only horizontal and perpendicular to the direction of propagation. These waves propagate in a medium that is limited in its upper part by an ideal reflective surface, such as the discontinuity floor-air and in its lower part by a medium in which the speed of the transverse waves is higher than in the first [18].

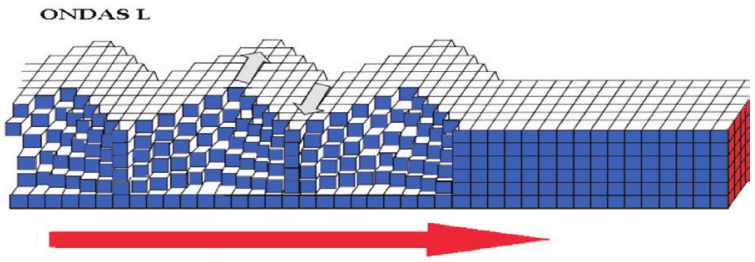

Figure A.82: Onda Love

Within this variety of waves, the P are those that propagate with greater speed (hence the name, primary), also presenting the characteristic of being able to spread by any type of material, whether solid or liquid. The S waves travel at a somewhat lower speed (secondary) and do not spread by liquid masses. Finally, surface waves travel at a lower velocity [45].
The different types of seismic waves travel at different speeds. P waves travel faster and arrive first. S waves travel more slowly, at 60% of the speed of P waves, so they arrive later. The surface waves are the slowest of all.
The friction absorbs the energy as the waves pass through a material, and the waves bounce off the layers and obstacles on the Earth, so the amount of energy carried by the seismic waves decreases the farther they travel [45].
The materials of the real earth are imperfectly elastic, which leads to the loss of energy and the attenuation of seismic waves, that is, to a reduction in amplitude faster than would be expected only from the geometric dispersion. This attenuation is more pronounced for the less consolidated rocks and is also higher for the higher frequencies, the selective loss of the high-frequency components of a pulse that leads to its progressive widening over time as the impulse propagates [16].
These aspects are the basis of the solution proposed in this thesis.

AppendixA.3. A principle of the seismic method

It will take into account how waves propagate on a similar surface. A hemispherical wave front reaches equally spaced geophones that record the movement of the ground due to the arrival of waves (Figure A.83). he time travel of these waves are the primary interest, and therefore it is generally more convenient to represent a path through rays. A ray is a line drawn so that it is always perpendicular to successive portions of the front of the waves (this is strictly true only for isotropic materials), and therefore it is a path along which the impulse energy propagates [16]. The time travel of these waves between the energy source, trigger point or disturbance and each of the geophones can be determined in the field seismograms. With this data, we can build a graph that will be called **Dromochrones or Time Travel Curves** [47].

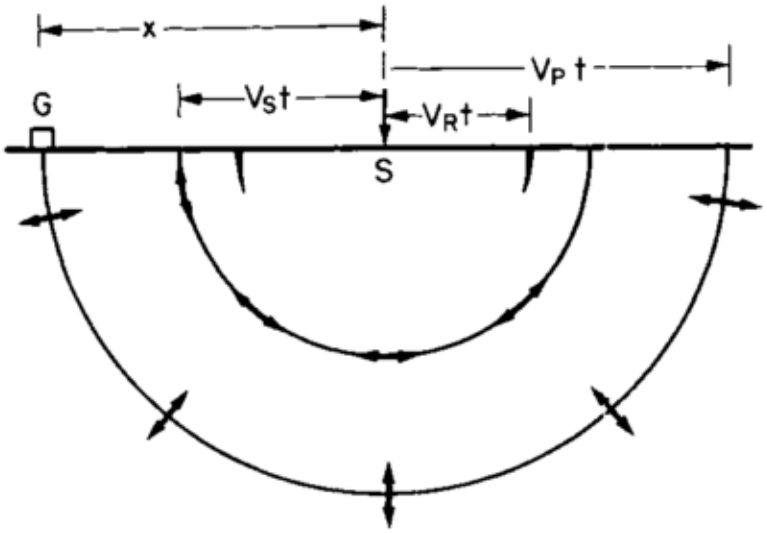

Figure A.83: Pulse pulses of the waves P, S and R in one time t in ms after generating a pulse in the point S [48]

Since the geophones are equally spaced, the curve will be a straight line that passes through the origin whose time travel equation will have the form:

$$tiempo = \frac{d}{v} \qquad \text{es decir} \qquad t = \frac{x}{v_1} \tag{A.1}$$

Deriving A.1 the slope is obtained:

$$\frac{dt}{dx} = m = \frac{1}{v_1} \qquad \text{o} \qquad v_1 = \frac{1}{m} \tag{A.2}$$

It means that with a graph of this type, we can determine the speed of the direct wave that propagates between the source and the sensor, and thus obtain some information about the material through which it was propagated [47].

As you know, the soil is not homogeneous. A stratified medium usually approximates the ground, each layer has a constant speed or one that changes regularly and straightforwardly with depth. The interfaces between the layers can be inclined at any angle concerning the horizontal and each other, but the model can be treated more easily when the stratification is horizontal.

For the reader's reference in the proposed solution, we will consider the case of a horizontal interface at a *depth* h_1 between the media with wave velocities P v_1 and v_2, where v_1 is the velocity in the first layer and v_2 the velocity in the second layer, where this is the highest velocity [16]. It is to be expected that refractions, reflections, and conversions of the waves will be found in each interface or layer.

Figure (A.84) shows a diagram of rays that show the possible paths for body waves generated by a perturbation E and registered by a tt geophone, the trajectory marked with (1) is the same trajectory of a wave surface, and the trajectory marked with (2) is the path of the P wave, where this direct wave travels with a velocity V_P that is greater than the velocity of the surface waves.

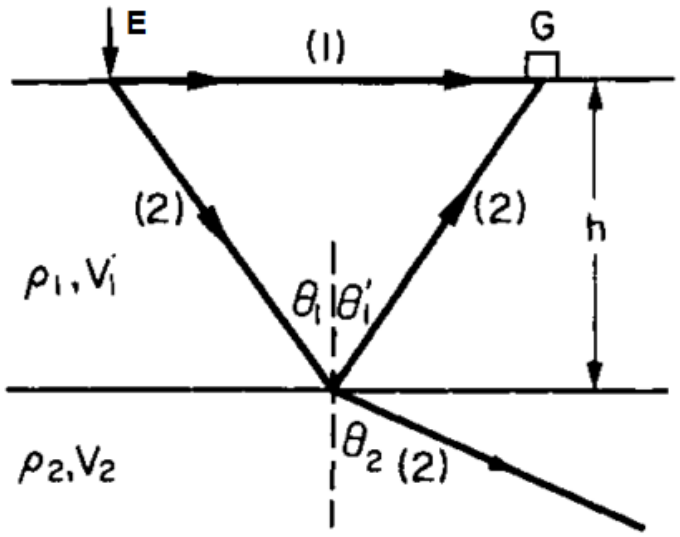

Figure A.84: (1) Trayectoria de un rayo directo. (2) Trayectoria de un rayo del mismo pulso reflejado y refractado [48]

Any wave that encounters an interface between different velocity media is partly reflected and partly transmitted. The laws of reflection and refraction are the same as those known in optics, so that for the ray (2) in figure A.84, θ_1 is the angle of incidence of the ray and θ_1' is the refracted angle, and we have that $\theta_1 = \theta_1'$ nd also:

$$\frac{\sin\theta_1}{V_1} = \frac{\sin\theta_2}{V_2} \qquad \text{(Ley de Snell)} \tag{A.3}$$

The *refractive index* of the interface is $\sin\theta_1/\sin\theta_2 = V_1/V_2$ para $V_2 > V_1$.
The amplitudes A_r and A_t of the reflected and transmitted waves vary in complicated ways with angle of incidence, but the reflection coefficient $r = A_r/A_i$ for a normally incident wave of amplitude A_i depends only on the properties of the means and is given by :

$$r = \frac{\rho_2 V_2 - \rho_1 V_1}{\rho_2 V_2 + \rho_1 V_1} = \frac{Z_2 - Z}{Z_2 + Z} \tag{A.4}$$

such that $-1 \leq r \leq 1$.
It depends on the *acoustic impedances* Z_1 and Z_2 of the medium instead of just on their velocities, but the changes in density ρ are in practice no more than about $\pm 20\%$, whereas the seismic velocity can change by $\pm 50\%$.An interface with good speed contrast (strictly speaking, impedance contrast) will result in a strong reflection, and also if Z_2 is smaller Z_1, it means if the reflection is on the surface of a slower medium, the quotient is negative.
The ray (2) of the figure A.84 then gives rise to two rays: a reflected ray that returns to the surface and registers in the geophone G, and a refracted ray, which continues in the second interface.
In figure A.85 nother ray (3) of the same impulse front is drawn: this has a greater incidence angle θ_C which is so large that the path of the refracted beam is parallel to the limit of the interfaces, that is, $\sin\theta_1 = 1$ and so on:

$$\sin\theta_C = \frac{V_1}{V_2} \tag{A.5}$$

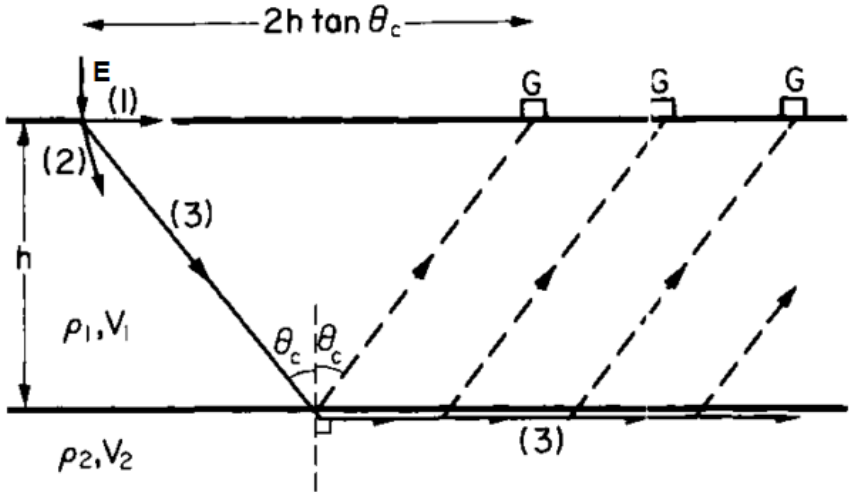

Figure A.85: Path of refracted rays (full line) and a set of refracted rays (dotted lines) [48].

It is the critical incidence condition, and θ_C is known as the critical angle: The rays that have the highest incidence angles are adequately reflected. If v_2 is less than v_1 the path of the rays is not refracted towards the normal, therefore the critical refraction should not occur.

The ray parallel to the limit is in the lower half, and the treatment with rays would only lead us to suppose that no energy can be returned to the surface by this path. However, the theory of wave propagation with these boundary conditions shows that the pulse as it travels with velocity v_2 along the lower side of the interface, will generate in the upper half a pulse of reasonably small size of known amplitude as the head wave in which the ray trajectories are inclined at the same angle θ_C o the normal as are the falling rays that are critically refracted. A geophone on the surface at any distance more significant than the **critical range** $2h \tan \theta_C$ will be placed on one of these rays and will record the arrival of the wave at the appropriate time.

The nature of the head wave can be qualitatively understandable if it is remembered that the seismic pulse is a region of tension in the rock and that a pulse in the lower half is necessarily accompanied by some tensions in the upper middle part of the limit. This region of elastic tension of the upper means moves along the interface with a velocity v_2, figure A.86.

Since the elastic waves can travel in the upper medium with a lower velocity v1, this results in the generation of the shock wave and the head wave can be considered as its analog. Since the wave head wave is derived from the refracted wave, it is clear that its amplitude at any point must decrease with the increase in the velocity contrast, since this increases the proportion of the incident energy returned by reflection.

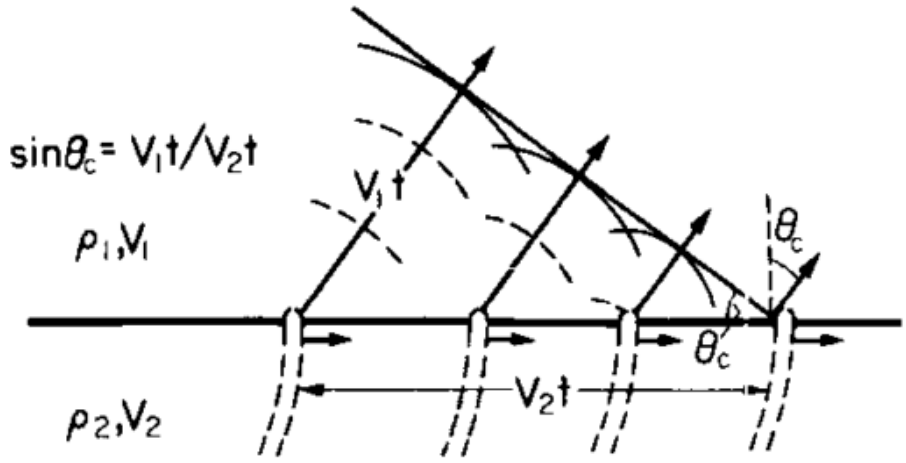

Figure A.86: Generation of a head wave by the passage of a refracted pulse along a limit [48].

Although in the calculation of the pulse time travel for these three paths, it is convenient to refer to the diagrams of the figures A.84 and A.85, the process of its propagation can be better understood by visualizing the successive positions of the pulse fronts, to which the rays are ordinary. Figure A.87 shows the diagrams of the direct wavefront, reflected and refracted, as well as the head wave. In a geophone beyond the critical range, but not too far from the disturbance, the direct wave arrives before the head wave, but at distances more significant than the critical distance x_c the head wave arrives first.

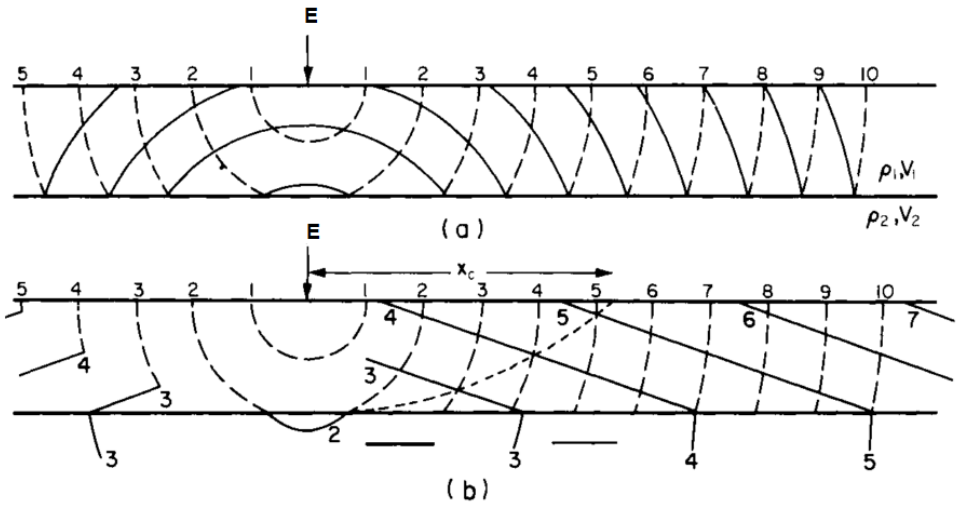

Figure A.87: Positions of the wavefront of a pulse at equal time intervals for (a) direct and reflected pulse; (b) direct and refracted pulses and head wave pulses. The dotted line joins points at which the travel times of the direct and head wave impulses are equal. It reaches the surface at the critical distance x_c of S. The left part of the diagram has been simplified further by omitting those parts of the pulse fronts that do not produce first surface arrivals. [48].

AppendixB. Seismic refraction model 2D

Seismic refraction has a long and distinguished history. Although seismographs developed in the latter part of the 19th century, it was not until the early 20th century that important discoveries of refraction techniques emerged. In 1909 A. Mohorovicic determined that there is a discontinuity of velocity at the base of the crust based on his interpretation of the wave arrivals of a nearby

earthquake. Then, in 1913, B. Gutenberg determined the depth of the Earth's core. Therefore, the seismic refraction was responsible for our knowledge early of the basic structure of the Earth. In the 1920s, refraction techniques were applied vigorously and successfully to oil exploration.
As the seismic techniques and the equipment improved, the reflection eventually replaced the refraction as the dominant method applied in the exploration. However, refraction continues to be the most frequently applied seismic technique for superficial investigations [47].

AppendixB.1. Horizontal layers

A first step is to analyze the refracted wave, to then derive an equation of time travel that can be analyzed, find the critical distance and depth of each layer.

AppendixB.1.1. An interface

The figure (B.88) shows the complete graph for the simple horizontal interface of the figures (A.84) and (A.85), ignoring S and R waves that are slower waves.

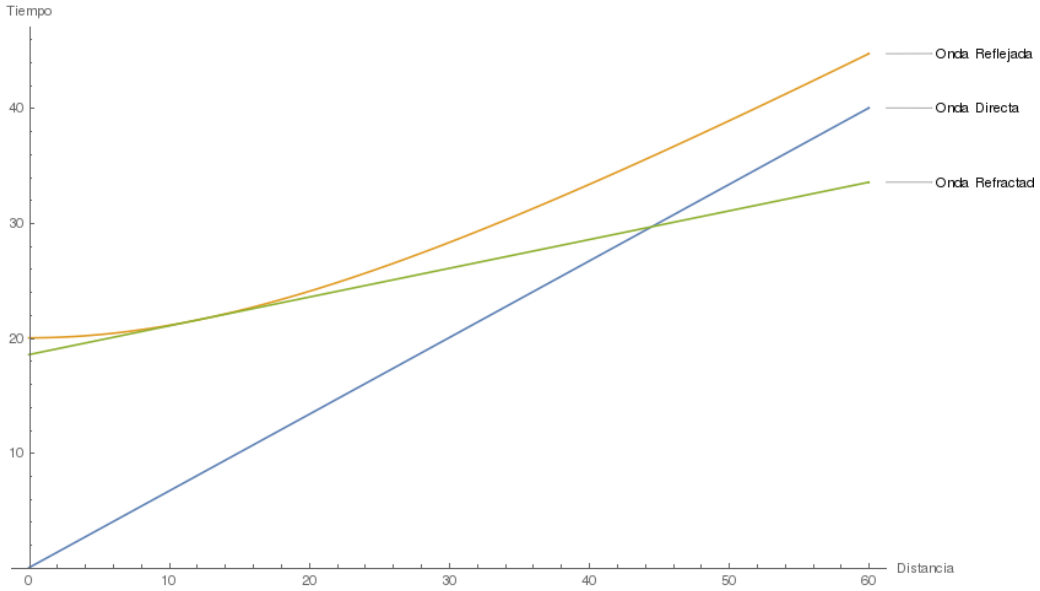

Figure B.88: Traveltime graphs for direct, reflected and refracted waves. In a single horizontal interface at depth $h = 15m$ it divides a higher speed means $V_1 = 1500m/s$ from a lower speed $V_2 = 4000m/s$.

It is easy to see from the ray diagram that a geophone near the trigger point will record the arrival of the reflected pulse after a time $2h/v_1$, and also that in horizontal ranges much higher than the depth h of the reflected path it becomes practically the same to direct, so that the graphs for these two paths must join asymptotically for large values of x. The actual length of the reflected trajectory is:

$$2\sqrt{h^2 + (x/2)^2} \tag{B.1}$$

As you can see in the figure A.84 it goes through the speed V1, you see the time-distance relationship for the reflected pulse must be:

$$
\begin{aligned}
t &= \frac{2\sqrt{h^2+(x/2)^2}}{V_1} \\
t &= \frac{\sqrt{4h^2+x^2}}{V_1} \\
t^2 &= \frac{4h^2+x^2}{V_1^2} \\
t^2 &= \frac{(2h)^2}{V_1^2}+\frac{x^2}{V_1^2} \qquad \text{(B.2)}
\end{aligned}
$$

Taking $t_0 = 2h/V_1$ there is

$$t^2 = t_0^2 + \frac{x^2}{V_1^2} \qquad \text{(B.3)}$$

then $t = t_0$ for $x = 0$ and $t \to x/v_1$ when x is large enough.
The shape of the graph for the head wave can also be qualitatively predicted if it is remembered that this wave is generated by a disturbance that travels horizontally at the highest velocity v_2 and therefore will have this apparent velocity across the surface, this point refers to the start of the next phase.
The graph will not pass through the origin, as the direct wave, since the wave is not subject to a delay in the displacement towards the high-speed refractor and another delay in the return to the surface. These two delays result in an intersection in the time if the graph occurs from $x = 0$.
The graph does not have physical reality for angles of incidence lower than the critical angle, that is, for values of x less than the *critical range* $2h\tan\theta_c$, since the head wave does not exist at all for such short intervals. Even at slightly longer intervals, the head wave will be so delayed by the inclined parts of its trajectory that it will arrive after the direct wave, and only beyond the critical range x_c will the head wave be the first recorded event on the seismogram. Since the amplitude of the head wave is usually much smaller than that of the direct wave, the part of its graph of time travel before the crossover range can rarely be observed in practice.
The equation of the time-distance graph for the refracted wave can be found by adding the times in each of the three sections of its path (Fig B.89).
The path traveled by the disturbance from the energy source **E** to the geophone **G** is that ray that is refracted with a critical angle and travels at the speed v_2 through the interface, as shown in figure B.89. As each point reached by this ray emits new waves by the Huyggens Principle, we will only consider the one that comes out with the same incident angle θ_c.

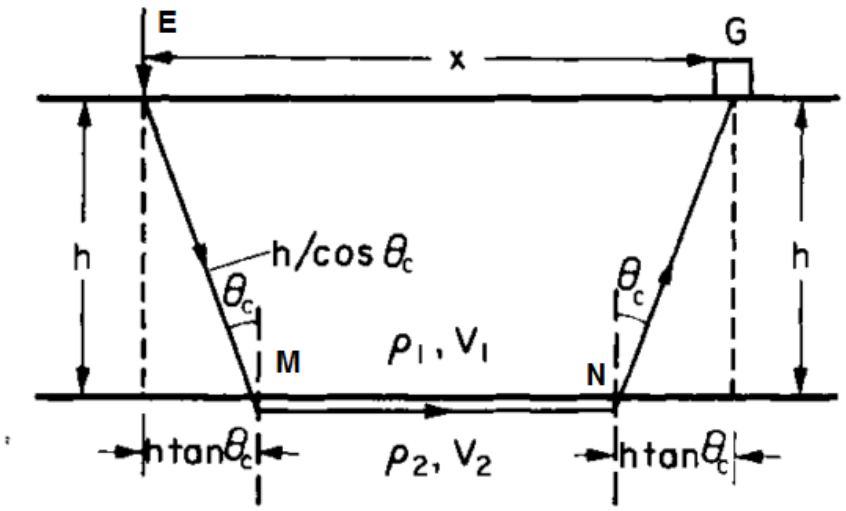

Figure B.89: Geometría de la trayectoria de la onda principal [48].

The equation of time travel will then be:

$$t = \frac{\overline{EM}}{v_1} + \frac{\overline{MN}}{v_2} + \frac{\overline{NG}}{v_1} \tag{B.4}$$

Replacing in equation B.4 we have:

$$\begin{aligned} t &= \frac{1}{V_1}\frac{h}{\cos\theta_c} + \frac{x - 2h\tan\theta_c}{V_2} + \frac{1}{V_1}\frac{h}{\cos\theta_c} \\ &= \frac{x}{V_2} + 2h\left(\frac{1}{V_1\cos\theta_c} - \frac{\tan\theta_c}{V_2}\right) \end{aligned} \tag{B.5}$$

$$\begin{aligned} t &= \frac{x}{V_2} + 2h\left(\frac{1}{V_1\cos\theta_c} - \frac{\sin\theta_c}{V_2\cos\theta_c}\right) \\ &= \frac{x}{V_2} + 2h\left(\frac{V_2 - V_1\sin\theta_c}{V_1V_2\cos\theta_c}\right) \\ &= \frac{x}{V_2} + 2hV_1\left(\frac{V_2/V_1 - \sin\theta_c}{V_1V_2\cos\theta_c}\right) \end{aligned} \tag{B.6}$$

By equation B.5 we can rewrite the equation B.6 in the following way:

$$
\begin{aligned}
t &= \frac{x}{V_2} + 2hV_1\left(\frac{1-\sin^2\theta_c}{V_1V_2\sin\theta_c\cos\theta_c}\right) \\
&= \frac{x}{V_2} + 2hV_1\left(\frac{\cos^2\theta_c}{V_1V_2\sin\theta_c\cos\theta_c}\right) \\
&= \frac{x}{V_2} + 2hV_1\left(\frac{\cos\theta_c}{V_1V_2\sin\theta_c}\right) \\
&= \frac{x}{V_2} + 2hV_1\left(\frac{\cos\theta_c}{V_1^2}\right) \\
&= \frac{x}{V_2} + 2h\left(\frac{\cos\theta_c}{V_1}\right) \\
&= \frac{2h\cos\theta_c}{V_1} + \frac{x}{V_2} \\
&= \frac{2h\left(1-(V_1^2/V_2^2)\right)^{1/2}}{V_1} + \frac{x}{V_2} \\
&= \frac{2h\left(V_2^2-V_1^2\right)^{1/2}}{V_1V_2} + \frac{x}{V_2}
\end{aligned} \tag{B.7}
$$

It means,

$$
t = t_i + \frac{x}{V_2} \tag{B.8}
$$

where $1/v_2$ represents the velocity of the line and the *intersection time* $t_i = \dfrac{2h\left(V_2^2-V_1^2\right)^{1/2}}{V_1V_2}$, is the intersection of the line on the time axis.

AppendixB.1.2. Critical distance

The data x_c is the value x that satisfies both the equation B.8 and that of the direct wave line $t = x/V_1$, therefore

$$
\frac{x_c}{V_1} = \frac{x_c}{V_2} + t_i \tag{B.9}
$$

So,

$$
\begin{aligned}
x_c &= \frac{t_1}{\dfrac{1}{V_1}+\dfrac{1}{V_2}} \\
x_c &= 2h\sqrt{\frac{V_2+V_1}{V_2-V_1}}
\end{aligned} \tag{B.10}
$$

Time travel equations B.8 and B.3 form the basis of the reflection and refraction seismic methods to determine the depth of an interface. The method of refraction is mainly based on the measurement of the time travel of the first arrivals to the geophones and that this is technically a more straightforward question than the observation of reflected waves that occur later in a complex record since these are of small amplitude compared to the direct wave.

It does not mean that subsequent arrivals (particularly arrivals of the direct wave beyond the critical distance) have no value in the refraction method: in fact, it is always desirable to identify them if possible, and they can often be essential for an unequivocal interpretation.

AppendixB.1.3. Determination of depth

From equation B.10 the depth h of the interface can be determined, if the velocities of the layers, V_1 and V_2 respectively, are known, using the following expression:

$$h = \frac{x_c}{2}\sqrt{\frac{V_2 - V_1}{V_2 + V_1}} \tag{B.11}$$

this same depth h can be found through the *intersection time* t_i

$$h = \frac{t_i V_1}{2\cos\theta_c} \tag{B.12}$$

The critical distance x_c for a range of depths is presented as an example in the following table. The velocities used were $V_1 = 500m/s$ and $V_2 = 1400m/s$ with a depth increase of 2m:

Depth (m)	x_c **(m)**
2	1.52944
4	3.05888
6	4.58831
8	6.11775
10	7.64719
12	9.17663
14	10.7061
16	12.2355
18	13.7649
20	15.2944

Another example that can be shown are the arrival times of the direct wave and the refracted wave (Table and Figure B.90), taking into account a depth of $h = 10m$, $V_1 = 1400m/s$ and $V_2 = 4500$with a position of the geophones every 3 meters.

Geophone	**Direct wave**	**Refracted wave**
0.	0.	13.5768
3.	2.14286	14.2434
6.	4.28571	14.9101
9.	6.42857	15.5768
12.	8.57143	16.2434
15.	10.7143	16.9101
18.	12.8571	17.5768
21.	15.	18.2434
24.	17.1429	18.9101
27.	19.2857	19.5768
30.	21.4286	20.2434
33.	23.5714	20.9101
36.	25.7143	21.5768
39.	27.8571	22.2434
42.	30.	22.9101
45.	32.1429	23.5768
48.	34.2857	24.2434
51.	36.4286	24.9101
54.	38.5714	25.5768
57.	40.7143	26.2434
60.	42.8571	26.9101

The following figure B.90 shows an example of the arrival times of the refracted ode (in orange) and the direct wave (in red).

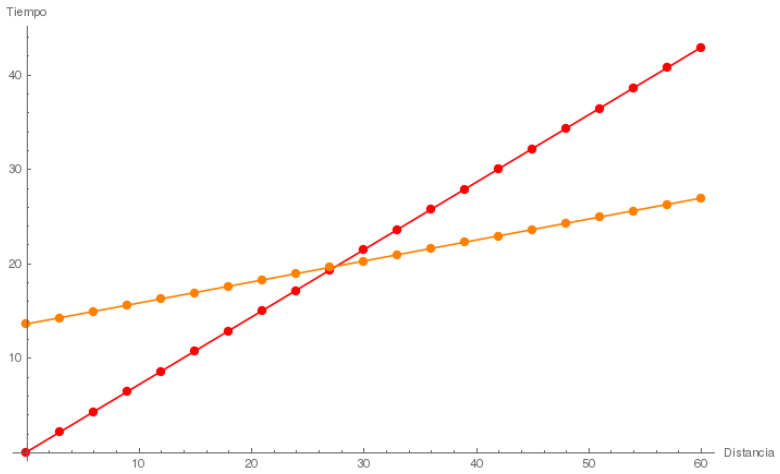

Figure B.90: Times of arrival of the refracted wave and the direct wave.

AppendixB.1.4. Two horizontal layers

When the subsoil has two interfaces, which is known as the case of three layers, always horizontal, obtaining the time travel equation has a shape similar to that of two layers.

The path traveled by the disturbance from the energy source **E** to the geophone **G**, will be the one corresponding to the ray that is refracted with a critical angle and travels at the speed V_3 through the second interface. This implies that in the layer with speed V_2 there is a noncritical refraction based on the velocities V_1 and V_2,

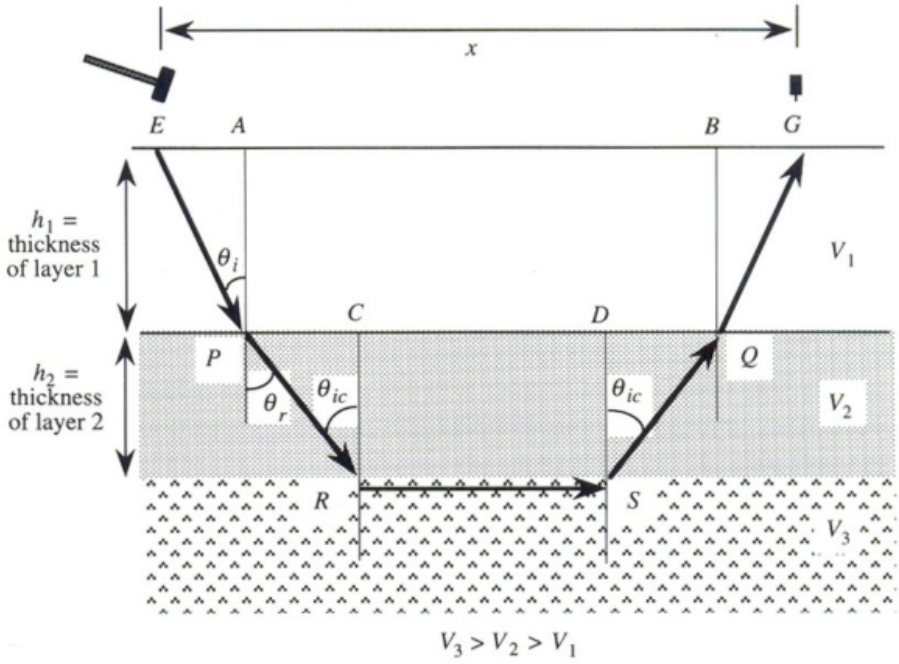

Figure B.91: Geometry of the trajectory of the main wave in three layers[47].

Taking into account the geometry of the main wave represented in the figure B.91 the time travel equation will then be:

$$t = \frac{\overline{EP}}{V_1} + \frac{\overline{PR}}{V_2} + \frac{\overline{RS}}{V_3} + \frac{\overline{SQ}}{V_2} + \frac{\overline{QG}}{V_1} \tag{B.13}$$

With what resulted, the time is:

$$t = \frac{2h_1 \cos\theta_i}{V_1} + \frac{2h_2 \cos\theta_{ic}}{V_2} + \frac{x}{V_3} \tag{B.14}$$

and finally it is

$$t = \frac{2h_1(V_3^2 - V_1^2)^{1/2}}{V_3 V_1} + \frac{2h_2(V_3^2 - V_2^2)^{1/2}}{V_2} + \frac{x}{V_3} \tag{B.15}$$

It means,

$$t = t_{i1} + t_{i2} + \frac{x}{V_3} \tag{B.16}$$

Where $1/V_3$ is the slope of the line that appears to have three layers,
$t_{i1} = \frac{2h_1(V_3^2 - V_1^2)^{1/2}}{V_3 V_1}$ and $t_{i2} = \frac{2h_2(V_3^2 - V_2^2)^{1/2}}{V_2}$ re the times of intersection of the first and second line, as indicated by the figure B.92

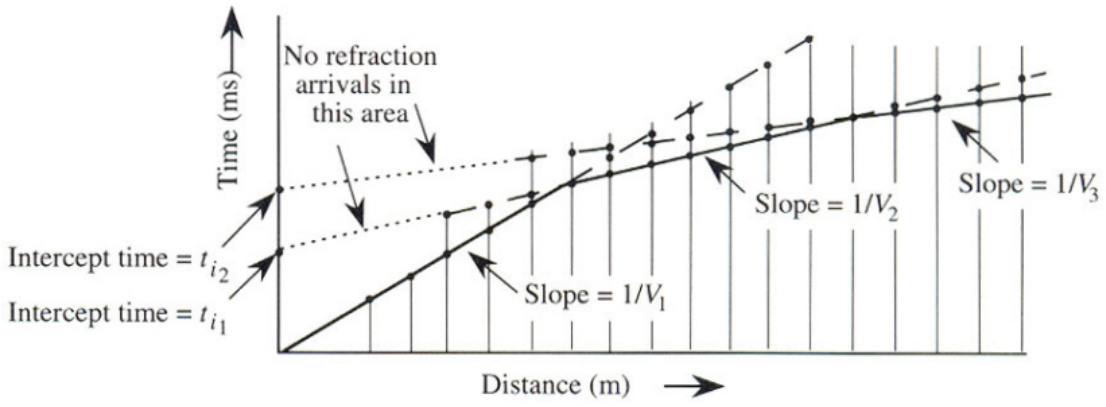

Figure B.92: Wave travel time in two interfaces [47].

AppendixB.1.5. Determination of depth

The determination of the depth h_2 of the interface can be determined through the times of intersection, that is:

$$h_2 = \frac{V_2 h_1 \cos\theta_i}{V_1 \cos\theta_{ic}} - \frac{V_2 t_{i1}}{2\cos\theta_{ic}} - \frac{V_2 t_{i2}}{2\cos\theta_{ic}} \tag{B.17}$$

Equation B.17 can be rewritten as follows:

$$h_2 = \left[t_{i2} - \frac{2h1\cos\theta_i}{V_1}\right] \frac{V_2}{2\cos\theta_{ic}} \tag{B.18}$$

and, finally

$$h_2 = \left[t_{i2} - \frac{2h_1(V_3^2 - V_1^2)^{1/2}}{V_3 V_1}\right] \frac{V_3 V_2}{2(v_3^2 - V_2^2)^{1/2}} \tag{B.19}$$

AppendixB.1.6. Critical distance

The critical distance xcrit for the head wave produced by the critical refraction along the second interface is EG in figure B.93. The ray path for this geometry is $EPRQG$. Thus x_{crit} is equal to

$EA + PC + CB + BG$. As $EA = BG = h_1 \tan\theta_i$ and $PC = CQ = h_2 \tan\theta_{ic}$, y $\sin\theta_i = V_1/V_3$ and $\sin\theta_{ic} = V_2/V_3$,

$$x_{crit} = 2\left[h_1 \frac{\sin\theta_i}{(1-\sin\theta_i^2)^{1/2}} + h_2 \frac{\sin\theta_{ic}}{(1-\sin\theta_{ic}^2)^{1/2}}\right] \tag{B.20}$$

$$x_{crit} = 2\left[h_1 \frac{V_1/V_3}{\left[1-[V_1/V_3]^2\right]^{1/2}} + h_2 \frac{V_2/V_3}{\left[1-[V_2/V_3]^2\right]^{1/2}}\right] \tag{B.21}$$

$$x_{crit} = 2\left[h_1 \frac{V_1}{(V_3^2-V_1^2)^{1/2}} + h_2 \frac{V_2}{(V_3^2-V_2^2)^{1/2}}\right] \tag{B.22}$$

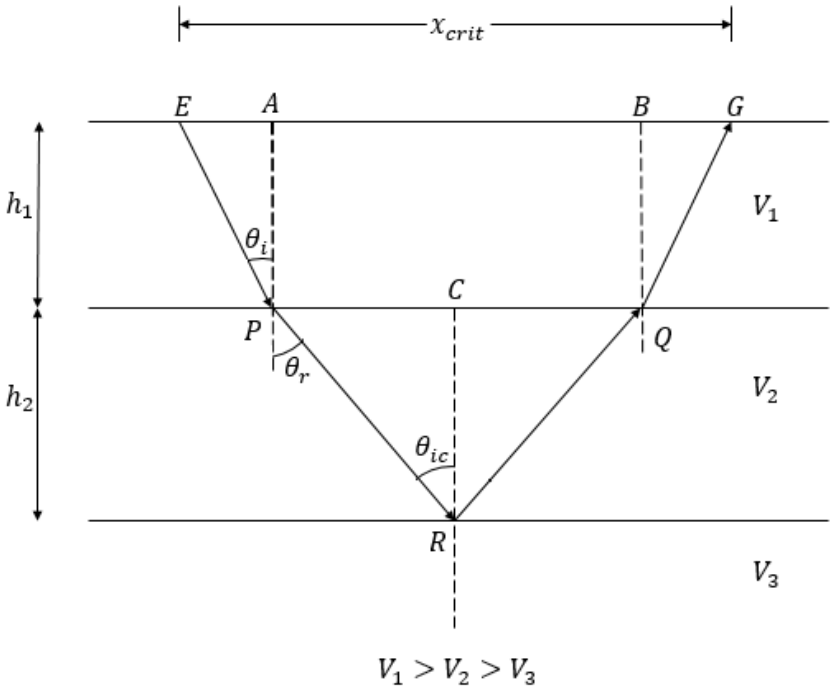

Figure B.93: Symbols used for determining the critical distance

AppendixB.1.7. Multiple horizontal layers

When the subsoil has multiple layers, always horizontal, obtaining the time travel equation has a similar shape to that of one or two layers.

$$t_n = \frac{x}{V_n}\frac{2}{V_n}\sum_{i=1}^{n-1} h_i \frac{(V_n^2 - V_i^2)^{1/2}}{V_i} \tag{B.23}$$

From equation B.23 it can be used to find an equation that incorporates the intercept time $t_{i_{n-1}}$ and solve the depth h_{n-1}. The speeds are determined with the inverse of the slopes, and the depths are calculated using the intercept times and starting with layer one until arriving at layer $n-1$.

AppendixB.2. Inclined Layers

The simple situations presented in the previous section are often not valid. One of the most serious defects is the neglect of the inclination of the layers since it drastically modifies the distance-time curve for the refraction.

AppendixB.2.1. An inclined layer

The derivation of the time travel equation for an inclined layer is necessarily the same as for a horizontal layer.

The symbols involved for the derivation of the time-distance equation are identified in Figure B.94.

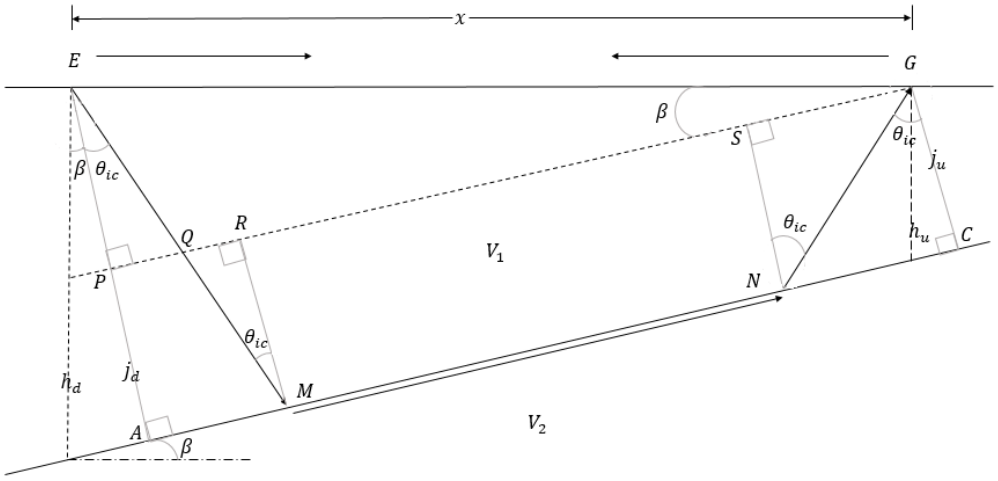

Figure B.94: Symbols used to derive the time-distance equation for an inclined layer

First the case will be addressed when the energy source is in the position E:

$$t_d = \frac{EM}{V_1} + \frac{MN}{V_2} + \frac{NG}{V_1} \tag{B.24}$$

$$\text{where } EM = \frac{j_d}{\cos\theta_{ic}}, NG = \frac{j_u}{\cos\theta_{ic}}, \tag{B.25}$$

and also

$$j_u = j_d - EP = j_d - x\sin\beta \tag{B.26}$$

$$NG = \frac{j_d - x\sin\beta}{\cos\theta_{ic}}. \tag{B.27}$$

because $MN = PG - AM - NC$, and therefore

$$PG = x\cos\beta, \quad AM = j_d\tan\theta_{ic}, \tag{B.28}$$

and

$$NC = j_u\tan\theta_{ic} = (j_d - x\sin\beta)\tan\theta_{ic}. \tag{B.29}$$

with what the distance-time equation gives:

$$t_d = \frac{j_d}{V_1\cos\theta_{ic}} + \frac{x\cos\beta - j_d\tan\theta_{ic} - (j_d - x\sin\beta)\tan\theta_{ic}}{V_2} + \frac{j_d - x\sin\beta}{V_1\cos\theta_{ic}}. \tag{B.30}$$

using the trigonometric identities:

$$\sin(\theta_{ic} - \beta) = \sin\theta_{ic}\cos\beta - \cos\theta_{ic}\sin\beta$$
$$\sin(\theta_{ic} + \beta) = \sin\theta_{ic}\cos\beta + \cos\theta_{ic}\sin\beta,$$

1032 you can reduce equation B.30, where it remains

$$t_d = \frac{2j_d\cos\theta_{ic}}{V_1} + \frac{x}{V_1}\sin(\theta_{ic} - \beta). \tag{B.31}$$

1033 Doing the same procedure but this time the strong energy is in the G position. After simplifying,
1034 you get:

$$t_u = \frac{2j_u\cos\theta_{ic}}{V_1} + \frac{x}{V_1}\sin(\theta_{ic} - \beta). \tag{B.32}$$

1035 These two equations are very similar to the equations of a horizontal layer, the slopes need to be
1036 determined. Deriving the equations B.31 and B.32 we obtain:

$$\frac{dt_d}{dx} = \frac{\sin(\theta_{ic} - \beta)}{V_1} \quad \text{y} \quad \frac{dt_u}{dx} = \frac{\sin(\theta_{ic} + \beta)}{V_1}. \tag{B.33}$$

1037 Rewriting Equation B.33, we have:

$$m_d\frac{\sin(\theta_{ic} - \beta)}{V_1} \quad \text{y} \quad m_u = \frac{\sin(\theta_{ic} + \beta)}{V_1}. \tag{B.34}$$

1038 Remembering, you have no $\sin\theta_{ic} = V_1/V_2$, if you know θ_{ic} you can determine V_2. You also want
1039 to know the inclination of the layer, β. From Equation B.34, β and θ_{ic}. can be deduced. Then the
1040 equations take the form:

$$\theta_{ic} - \beta = \sin^{-1}(V_1 m_d) \quad \text{y} \quad \theta_{ic} + \beta = \sin^{-1}(V_1 m_u). \tag{B.35}$$

1041 Since m_u, m_d, and V_1 are determined directly from the travel-time curves, it can be solved for θ_{ic}:

$$\theta_{ic} = \sin^{-1}(V_1 m_d) + \beta \quad \text{y} \quad \theta_{ic} = \sin^{-1}(V_1 m_u) - \beta.$$

$$2\theta_{ic} = \sin^{-1}(V_1 m_d) + \sin^{-1}(V_1 m_u).$$

1042 and finally,

$$\theta_{ic} = \frac{\sin^{-1}(V_1 m_d) + \sin^{-1}(V_1 m_u)}{2}. \tag{B.36}$$

1043 Similarly, β can be found

$$\beta = \theta_{ic} - \sin^{-1}(V_1 m_d) \quad \text{y} \quad \beta = -\theta_{ic} + \sin^{-1}(V_1 m_u).$$

1044 Thus,

$$\beta = \frac{\sin^{-1}(V_1 m_u) - \sin^{-1}(V_1 m_d)}{2} \tag{B.37}$$

1045 *AppendixB.2.2. Determination of depth*
1046 At this point we know the critical angle and velocity of the first layer, with this information you can
1047 express equations B.31 and B.32 regarding intercept times:

$$t_{i_d} = \frac{2j_d\cos\theta_{ic}}{V_1} \tag{B.38}$$

$$t_{i_u} = \frac{2 j_u \cos\theta}{V_1}. \tag{B.39}$$

Since you have that $\cos\beta = j_d/h_d$ and $\cos\beta = j_u/h_u$, then the depth in the first layer is:

$$j_d = \frac{t_{i_d} V_1}{2\cos\theta_{ic}}, \tag{B.40}$$

$$j_u = \frac{t_{i_u} V_1}{2\cos\theta_{ic}}, \tag{B.41}$$

$$h_d = \frac{j_d}{\cos\beta}, \tag{B.42}$$

$$h_u = \frac{j_u}{\cos\beta}. \tag{B.43}$$

AppendixB.2.3. Multiple inclined layers

Determining time travel equation for multiple inclined layers, the same development must be followed as in the determination of the travel equation for multiple horizontal layers. In this section, the solution is presented.

AppendixB.2.4. Time travel equation

Based on Figure B.95, it should be noted that the anglesθ_i and ϕ_i are measured from the perpendicular of the layers and therefore represent the angles of incidence and refraction. The angles d_i and u_i are measured from the vertical.

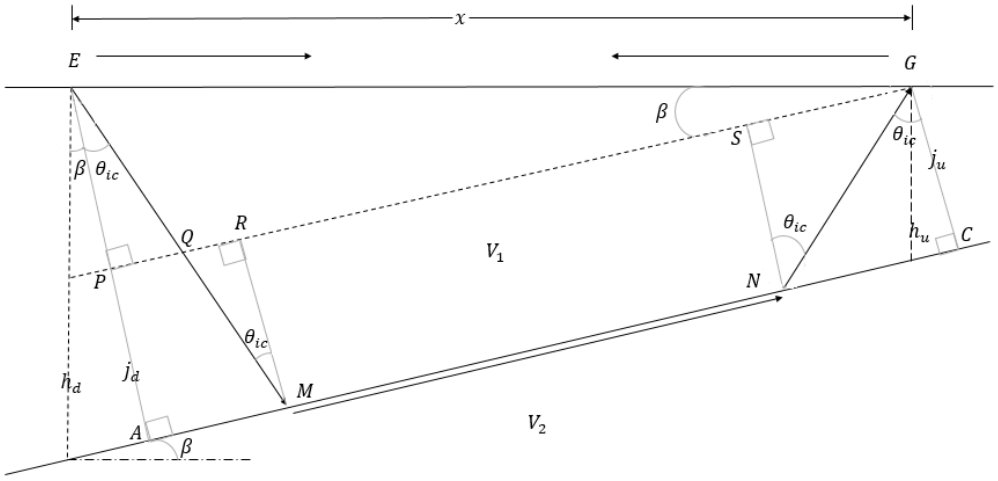

Figure B.95: Symbols used to derive the time-distance equation for inclined layers.

The time travel equation is given by:

$$t_d = \frac{x \sin u_1}{V_1} + \sum_{i=1}^{n-1} \frac{h_{di}}{V_i}(\cos d_i + \cos u_i) \tag{B.44}$$

and

$$t_u = \frac{x \sin d_1}{V_1} + \sum_{i=1}^{n-1} \frac{h_{ui}}{V_i}(\cos d_i + \cos u_i) \tag{B.45}$$

In which n is the number of layers.

AppendixB.3. Laterally variable velocity

The refraction method also allows detecting lateral changes of material on the surface (fig B.96), even when this change is covered or covered by another material (fig B.97). If these variations are not extreme, the speeds of the surface do not vary significantly, and the depths calculated for the interfaces will have only small errors.

The time travel curve in Figure B.96 illustrates that a field study in the higher speed direction gives a curve analogous to that produced by a single horizontal interface. However, an inverse travel produces a very unusual curve because the first segment has a lower slope than the second segment [17].

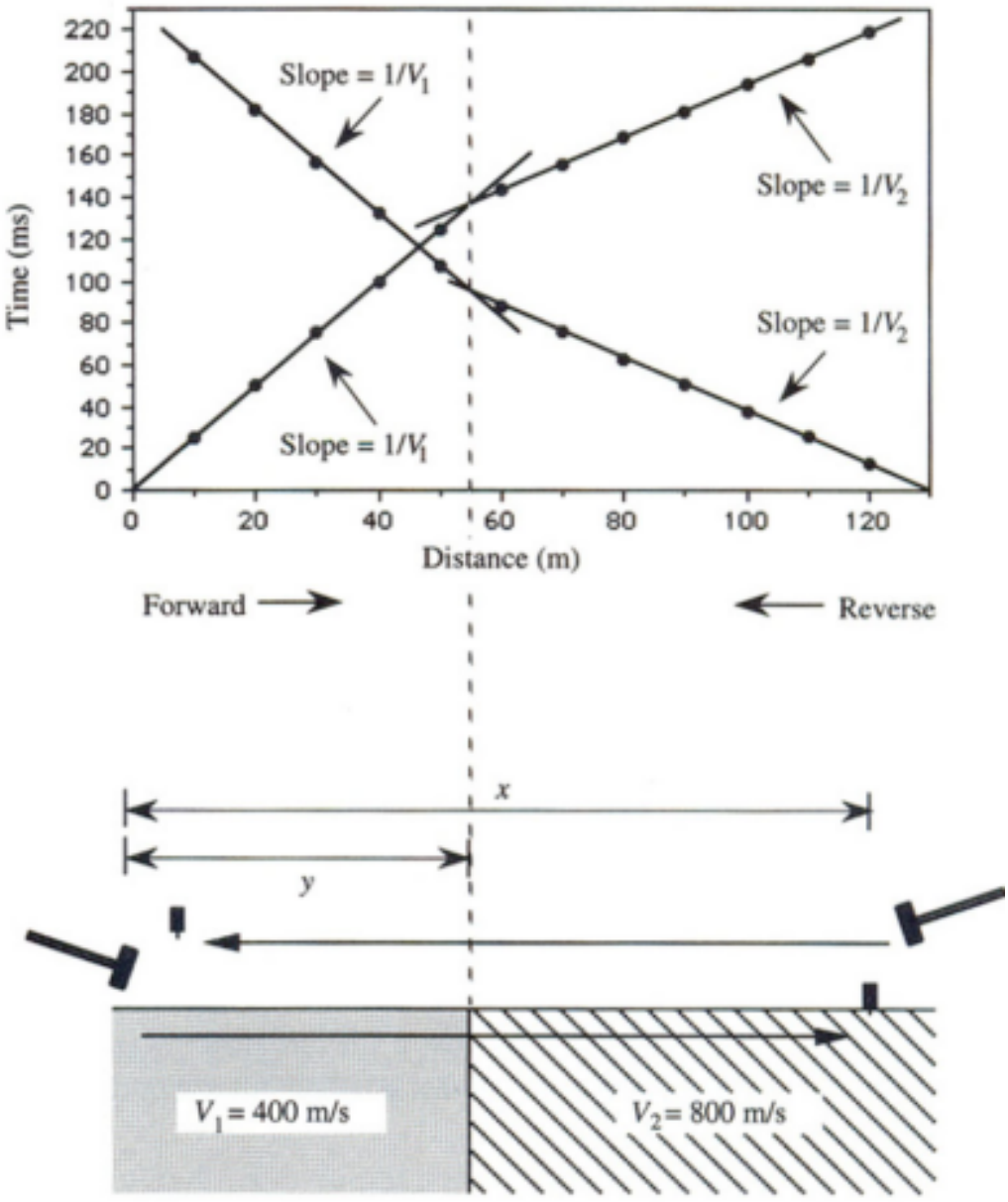

Figure B.96: Effect of a vertical velocity discontinuity in the forward and backward travel time curves. [17].

In this case the time travel equation of the curve is (based on Figure B.96):

$$t = \frac{y}{V_1} + \frac{x-y}{V_2} \quad \text{para } x \geq y \tag{B.46}$$

with slope

$$\frac{dt}{dx} = \frac{1}{V_2}. \tag{B.47}$$

Therefore, the presence of a vertical surface discontinuity can be recognized by the special pattern of time travel curves; the velocities of the materials can be determined; and locate the position of the discontinuity by the crossing distances of the segments of the forward and backward curves [17]. The breaks or the intersection of the ascending and descending lines coincide with the location of the change of material, when this occurs on the surface. When the material is hidden, the breaks do not coincide and the change of material will be between them (Fig B.97). In this case, a curve of three segments arises because the layer on the discontinuity is vertical. Once again, the slopes of the segments of the time travel curve produce all the speeds illustrated in the model. The general position of the discontinuity is indicated by the change in slope of the second and third segments of each transverse direction.

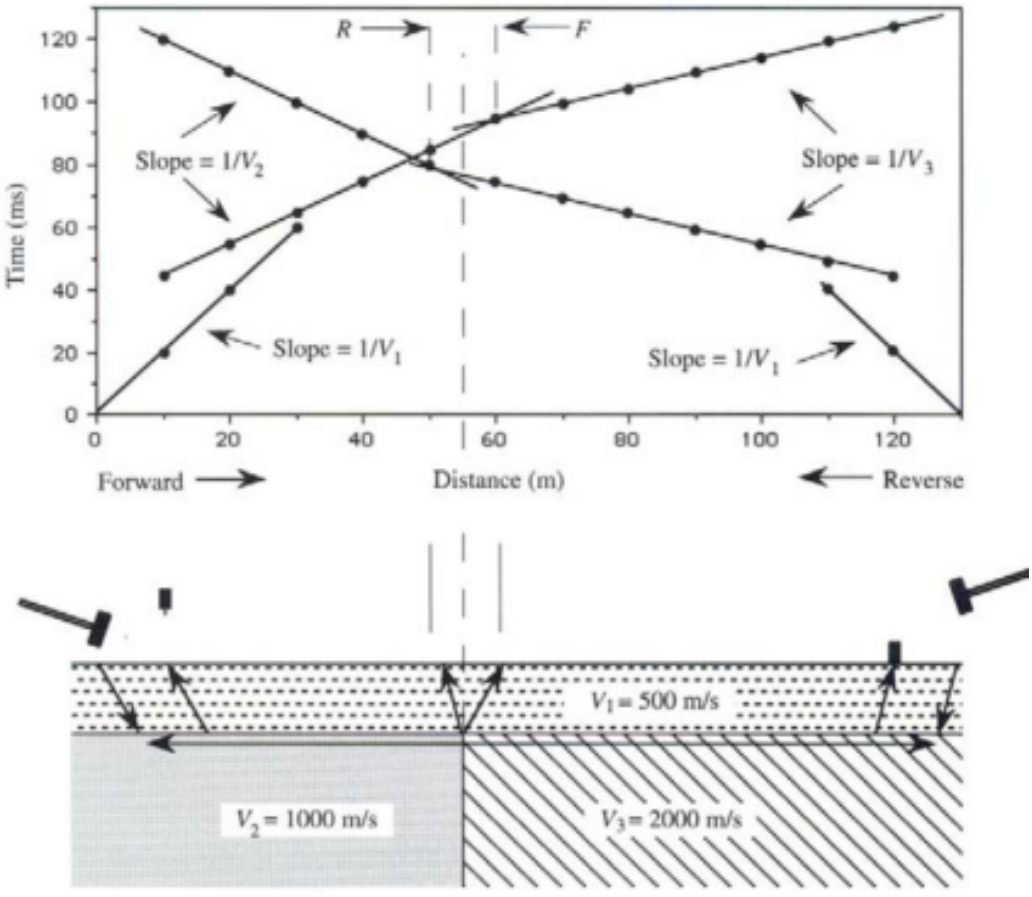

Figure B.97: Side changes of covered material [17].

AppendixB.4. Discontinuous Interface

Another particular case occurs when there is a jump or step by failure. The trajectories of the rays for the forward and backward travel curves resulting from traversing a vertical step are shown in Figure B.98. The area of interest is the region that surrounds the vertical step because it is essentially

treated with a two-layer situation at significant distances from the step in any direction. First, the journey ahead will be analyzed. Early arrivals consist of direct and refracted waves in the classical pattern, producing two segments of travel times of the curve (figure B.98).

Based on the figure B.98, it is observed that QA and RB have a difference in the intercept times, $t_{i2} - t_{i1}$, which is due to the extra distance, RD, traveling for RB at a speed V_1. RD is related to the critical angle and height of the jump or step z

$$RD = z \cos \theta_{i_c}, \tag{B.48}$$

so that the difference of time of the intercept and the jump z can be calculated as follows:

$$t_{i2} - t_{i1} = \frac{z \cos \theta_{i_c}}{V_1} \tag{B.49}$$

and

$$z = \frac{(t_{i2} - t_{i1})V_1}{\cos \theta_{i_c}} \tag{B.50}$$

o

$$z = \frac{(t_{i2} - t_{i1})V_2 V_1}{\sqrt{V_2^2 - V_1^2}} \tag{B.51}$$

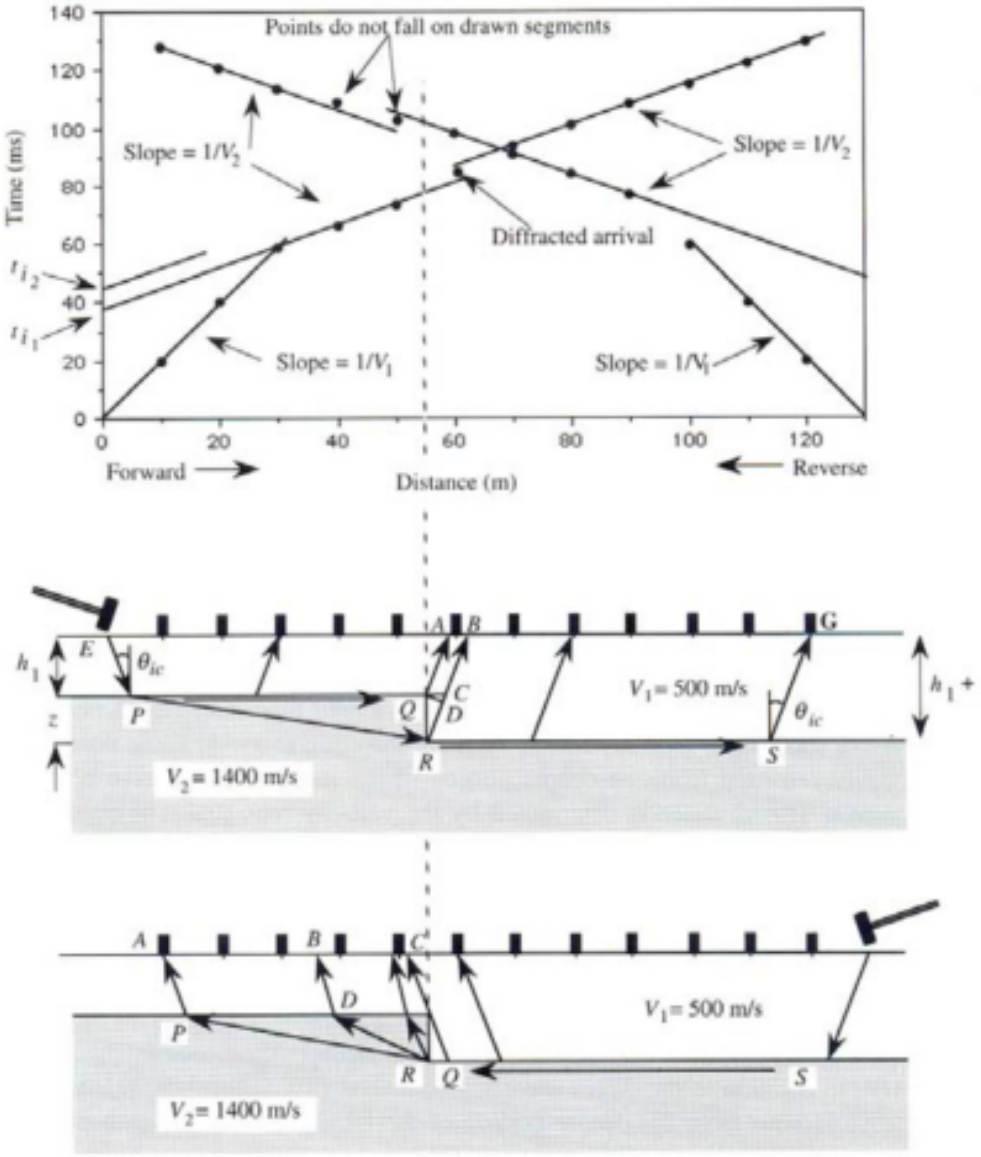

Figure B.98: Trayectorias de rayos y curvas de tiempo de viaje resultantes al atravesar un escalón vertical [17].